

School of Physics and Astronomy



Telescope Group Project Star Clusters Group 2

Olivia JACKSON, Joe KENNARD, Megan LEISHMAN,
Lewis LESLIE, Sebastian STRASZAK, Syaza IZZATI SUHAIRULAZRIN

March 2021

Abstract

Using the PIRATE telescope Johnson UBV passband observations of two star clusters, M52 and NGC 7789, have been taken and, using standard stars for calibration, data reduction and analysis have been performed to produce estimates of the population, reddening A_V , age, metallicity, and mass of each cluster. M52 was determined to have 209 cluster members and 529 members were found for NGC 7789. The radii of the clusters were determined to be 0.21(4) degrees for M52 and 0.20(5) degrees for NGC 7789. The core radii for the clusters was determined to be 0.06(2) degrees for M52 and 0.08(3) degrees for NGC 7789. The interstellar reddening, A_V , was calculated to be 1.896(5) for M52 and 1.18(2) for NGC 7789 leading to distance measurements of 1810(80) pc and 2370(40) pc respectively. Isochrone fitting estimated ages between 69-143 Myr for M52 and 1.38-1.48 Gyr for NGC 7789 to 3-sigma confidence. Metallicities were also determined, with $[Fe/H]$ values of 0.05 for M52 and -0.3 for NGC 7789. Finally, an initial mass function was used to determine the integrated cluster masses giving 1920 M_\odot and 5670 M_\odot for M52 and NGC 7789 respectively. A third smaller, more distant and fainter cluster [FSR 2007] 0433 was observed in the M52 frames, which has also been analysed, but was not a primary target.

Advisor: Ross McLure

Contents

1	Aims	1
2	Background	1
2.1	Open Star Clusters	1
2.2	Literature Studies of M52 (NGC 7654) and NGC 7789	2
2.2.1	Reddening	2
2.2.2	Distance	2
2.2.3	Age	3
2.2.4	Cluster Membership and Radius	3
2.3	Implications of the Results	3
3	Methods	4
3.1	Observation	4
3.1.1	Choosing Standard Stars and Star Clusters	4
3.1.2	Star Cluster and Standard Star Observations	5
3.1.3	Calibration Frames	5
3.1.4	Data Organisation	5
3.2	Basic Data Reduction	5
3.2.1	Master Bias Frame	6
3.2.2	Flatfields	6
3.2.3	Dark Current	6
3.3	Standard Star Calibration	7
3.4	Point Spread Function	8
3.4.1	Astrometry	8
3.4.2	Standard Star Photometry	9
3.4.3	Determining τ_λ & z_λ	10
3.5	Deep-stacking Cluster Images	11
3.5.1	Local Translational Alignment	12
3.5.2	Offset Alignment	13
3.5.3	Full Alignment and Stacking	13

3.6	Cluster Photometry & CMD Diagrams	13
3.6.1	Source Selection	14
3.6.2	Field Photometry	15
3.6.3	Catalogue Production	16
3.7	Cluster Membership	16
3.7.1	Determination of Cluster Members Using Proper Motion	16
3.7.2	Cluster Determination in aid of Extinction Coefficient - Visual Magnitude Cuts	16
3.8	Interstellar Extinction	17
3.9	Distance Determination	19
3.10	Cluster Centre Estimation	20
3.10.1	Cluster Centre Estimation by Mean	20
3.10.2	Cluster Centre and Average Proper Motion Estimate by Kernel Density Estimation	20
3.11	Radius Estimation via Surface Density Plots	20
3.12	Isochrone Fitting	21
3.12.1	Final Catalogue	21
3.12.2	Geometric Isochrone Fitting	22
3.12.3	Isochrone Error Estimation	23
3.13	Initial Mass Function Fitting	23
3.13.1	Obtaining and fitting an IMF	24
3.13.2	Integrated mass estimation	24
4	Results and Discussion	26
4.1	Observation	26
4.2	Standard Star Calibration	27
4.3	Deep Stacking	28
4.4	Photometry	29
4.4.1	Source Selection	29
4.4.2	Photometry	29
4.4.3	Preliminary CMD's	30
4.5	Cluster Membership Determination	31

4.5.1	Determination of Cluster Members Using Proper Motion	31
4.5.2	Cluster Determination in aid of Extinction Coefficient - Visual Magnitude Cuts	32
4.6	Reddening	33
4.6.1	Data from Cluster Membership Proper Motion: 1 x error tolerance	34
4.6.2	Data from Cluster Membership Proper Motion Matched with the Older Catalogue	36
4.6.3	Final Reddening Value	36
4.7	Distance Determination	36
4.7.1	Data from Cluster Membership Proper Motion: 1 x error tolerance	37
4.7.2	Data from Cluster Membership Proper Motion Matched with the Older Catalogue	39
4.7.3	Final Distance and Reddening Value	39
4.8	Cluster Centre Estimation	40
4.8.1	Cluster Centre Estimation by Mean	40
4.8.2	Cluster Centre and Average Proper Motion Estimate by Kernel Density Estimation	41
4.9	Radius Estimation via Surface Density Plots	42
4.10	Isochrone Fitting	44
4.10.1	Preliminary Fits using MIST: UBVR(I) & Temperature-Luminosity	44
4.10.2	Final Fits using PARSEC/COLIBRI CMD Isochrones	45
4.11	IMF Fitting	47
4.12	[FSR 2007] 0433: Serendipitous cluster discovery in M52 Image Field	48
4.12.1	Reddening & Distance	48
4.12.2	Centroid, Proper Motion & Membership	49
4.12.3	Isochrone fitting	50
5	Conclusion and Further Work	51
6	Acknowledgements	52
A	Observing Log	58
A.1	Observation Data	59
B	Reddening and Distance Plot: Cluster Membership Proper Motion Matched with the Older Catalogue	62
B.1	Reddening plot for M52 and NGC7789	62

B.2	Distance determination plot for M52 and NGC7789	63
C	Reddening and Distance: [FSR 2007] 0433 (Cluster near M52)	65
C.1	Reddening Plot	65
C.2	Distance Plot	66
D	Error Propagation	67
D.1	Simple Aperture Photometry	67
D.2	Optical Depth τ_λ	67
D.3	$I_\lambda(0)$, the above-atmosphere flux	67
D.4	Error in m_λ	68
D.5	Error in M_V	68
D.6	Error in dereddened (B-V) & M_V	69
E	Final Deep Image Stacks	70
F	Images: source extraction for clusters	71
G	Preliminary CMD's for clusters	73
H	Preliminary colour-colour diagrams for clusters	74
I	GAIA CMD's in 20' vicinity of clusters	75
J	Final CMD's for clusters	76
K	PARSEC/COLIBRI Isochrone fits for clusters	78
L	Preliminary MIST isochrone fits	80
M	[FSR 2007] 0433: Objects	81

1 Aims

The aims of this project were to take measurements of two star clusters using a remote telescope and, using these observations, infer physical properties of the clusters. Initially, the aims included calculating the clusters' reddening values, ages, distances, memberships, and radii. The group first aimed to produce calibrated and corrected images of the clusters by data reduction, use of standard stars, and de-reddening so that distances to the clusters could be determined via colour-magnitude diagrams. After this, focus was directed to techniques such as proper motion cluster membership estimation, isochrone fitting for age determination and producing surface density plots for values of the radius and core radius.

As the project proceeded, the initial aims expanded to include estimating the clusters' mass, initial mass function, and metallicity. In the corner of the M52 images a small cluster of stars was also identified that was of higher number density than the surrounding background. Though dwarfed by M52 and even more so by NGC 7789, this smaller cluster presented an opportunity to gather more data for analysis and was studied briefly after the main two clusters.

2 Background

2.1 Open Star Clusters

A star cluster is generally defined as a collection of stars localised in some area of space.^[1] Open clusters are formed when clouds of dense molecular gas collapse to form stars which are mutually gravitationally attracted to each other. Less than half of the original gas is used to form stars with the remainder being expelled and forming nebulae. These gas expulsion events from molecular clouds cause some of the newly formed stars to be ejected, shocking loose stars out of the cluster. Clusters formed from this process can be essentially unbound, resulting in a stellar association where stars share the same origin but are not gravitationally bound. Alternatively, the process can result in an open cluster with only a fraction of the original stars gravitationally bound together and the rest ejected.^[2] Simulations studying the well-known Orion Nebula Cluster have shown that the cluster only contains approximately 1/3 of its original members with the rest being blown out.^[3] Open cluster populations generally range from a few hundred to a few thousand stars.

After the surrounding gas nebula disperses, a distinct cluster of bound stars is left. Smaller mass open clusters will not have sufficient gravitational binding to hold onto its members due to the escape velocity of the cluster generally being much smaller than the average star velocity. This can occur from the gas ejection, lowering the cluster mass enough to result in this weak gravitational binding. After a few million years, the cluster itself will disperse.^[4] Clusters with masses large enough to keep their members after nebula evaporation will, on scales of tens of millions of years, lose mass via two-body relaxation where momentum is exchanged between larger and smaller stars resulting in the less massive star gaining enough velocity to exceed the cluster's escape velocity. On scales of a hundred million years, the cluster tends to pass by a giant molecular cloud upon which the resulting gravitational tidal forces will cause further disruption and cluster member evaporation. However, even after clusters have dispersed, cluster members still share characteristic properties and can be correlated together for multiple galactic orbits.^[2]

Since open clusters were formed from the same molecular cloud, cluster members share many characteristics making it easier to determine star properties for a large collection of stars. Cluster members are expected to have similar ages and metallicities, the approximate distance to each member will be the same, and when observing these clusters, atmospheric and interstellar extinction will vary minimally since the area of sky being observed will be small. For all these reasons, open clusters are ideal laboratories for studying stellar evolution; observing and evaluating clusters immediately gives a large number of fixed stellar variables without the need to observe properties of many individual stars with varying extinction, composition and distance. Luminosities and thus masses can also be determined easily since the distance is fixed and so apparent brightness will only scale with

mass (after atmospheric and interstellar extinction corrections).

Open clusters are typically found in the spiral arms of spiral galaxies where the star formation rate is highest. Their dispersion from the galactic plane is very low with a scale height of around 55pc. Old rich clusters are found to be more dispersed with a scale height of over 7.5kpc indicating a correlation between cluster age and dispersion in the galactic plane. Although open clusters tend to be younger than a few hundred million years, the rarer, older open clusters can be used in this way to study the evolution of the galactic disk.^[5]

Although the results presented in this report have been obtained via observation of open clusters, it is worth mentioning the second main type of cluster, globular clusters. Found in the halo of the Milky Way, they contain hundreds of thousands of stars, tightly gravitationally bound to form a spherical shape. Globular clusters are some of the oldest objects in the universe, with typical age values of tens of Gyrs. In this way, globular clusters are used to place a limit on the age of the universe with clusters such as Messier 4 (M4) having an age of 12.7 Gyrs.^[6] Formation of globular clusters is a topic of debate however stars in globular clusters are observed to have similar ages and metallicities.^[7] This suggests that globular clusters could have been formed the same way as open clusters, through a gravitationally bound gas cloud, and that there may not be much difference between rich open clusters and sparse globular clusters. Conditions in the earlier universe allowing many stars to form into a rich globular cluster may no longer be present in our galaxy explaining the absence of rich young globular clusters.^{[8][9]}

2.2 Literature Studies of M52 (NGC 7654) and NGC 7789

M52 and NGC 7789 are both open clusters with properties that have been studied prior to the observations reported here. By presenting literature data for these clusters, comparisons and determinations for the validity of the results obtained can be made. In particular, values for reddening, distance, and age have been obtained from a variety of sources as described below.

2.2.1 Reddening

M52 is generally deemed to have substantial interstellar extinction along its line of sight. A paper by Kaltcheva *et al* (1990)^[10] reports data on M52 using the Strömgren photometric system (or the uvby system). The paper determines the E(B-V) extinction to be 0.57 which corresponds to an A_V value of 1.767 when taking the ratio of total-to-selective extinction to be the standard for the diffuse interstellar medium, $R = 3.1$.^[11] Another paper by Kharchenko *et al* (2005)^[12] describes the use of the ASCC-2.5 (All Sky Compiled Catalogue of 2.5 Million Stars) as recorded by the ESA Hipparcos mission to study many open clusters including M52. The resulting E(B-V) value for M52 from this study was 0.65 corresponding to an A_V value of 2.015. A wider range of A_V values for M52 was reported in a paper by Pandey *et al* (2001)^[13] from observations taken at the Kiso Observatory in Japan. The reddening was found to be variable across the cluster with a minimum E(B-V) of 0.46 and a maximum of 0.80 producing a range of A_V values of 1.426 and 2.48 for the minimum and maximum reddening respectively. This study also illustrates the significant variability in reddening over the cluster and a potential area of future work.

For NGC 7789, Kaltcheva *et al* (1990)^[10] gives an E(B-V) value of 0.28(2) and thus an A_V of 0.868. NGC 7789 is a significantly less studied cluster than M52 and thus did not have a variety of reddening values that could be confidently referred to for literature values.

2.2.2 Distance

The distance to M52 is still a topic of debate but many estimates have been made from use of varying methods. Larger values of reddening contribute to this uncertainty in distance. Kaltcheva *et al* (1990)^[10] derives a distance modulus for M52 of $V_0 - M_V = 11.3(1)$. This corresponds to a distance of 1819.7pc. The study using the ASCC-2.5 by Kharchenko *et al* (2005)^[12] found distances to over 200 clusters for which M52 was determined to be 1421pc. The second GAIA data release, containing precise astrometry and photometry of stars observed via the

GAIA telescope, was also used to analyse over 1229 clusters in a paper by Cantat-Gaudin *et al* (2018)^[14]. For M52, GAIA DR2 parallax data was used to determine the most likely distance as 1600.01pc. Kiso Observatory’s observation described by Pandey *et al* (2001)^[13] deems M52 to be a distance 1380(70)pc. For this report, the GAIA parallax data will be used accessed from the SIMBAD Astronomical Database^[15] which measures the distances to astronomical objects through highly accurate parallax measurement. From this, M52 was determined to have a distance of 1677.85pc.

The distance to a few select clusters including NGC 7789 was specifically determined in a paper by Gao, Xin-hua (2018)^[16] also using the GAIA DR2 data but selecting cluster members using the Gaussian mixture model (GMM). The distance as determined from this paper was 2067(4)pc. From Kharchenko *et al* (2005)^[12], the distance was determined to be 2337pc. From the SIMBAD Astronomical Database, NGC 7789 was measured to have a distance of 2207.51pc.^[15]

2.2.3 Age

NGC 7789 is an old open cluster with age estimates in orders of Gyrs. A larger abundance of red giant stars as seen from observations illustrate this. From observations taken using the Beijing-Arizona-Taiwan-Connecticut (BATC) Multi-Color Survey photometric system as described in the paper by Wu *et al* (2007)^[17], the age estimate for NGC 7789 was given as 1.4(1) Gyr. Kharchenko *et al* (2005)^[12] estimated the age of NGC 7789 to be 1.7Gyr.

2.2.4 Cluster Membership and Radius

The number of stars in each cluster is an important factor to consider before performing further analysis. This can be dependent upon a number of things, including the chosen radius of the cluster in the sky. The literature radius of M52 was taken to be 13’ (arcminutes) as agreed upon by multiple sources.^{[18][19]} The Kiso Observatory observations by Pandey *et al* (2001)^[13] gave a cluster boundary of 11.7’. The Messier Catalogue gave a value of 193 members in M52 when measuring at a 9’ radius.^[18] Freestarcharts estimated the number of members to be around 200 also with a radius of 13’.^[20]

For NGC 7789, Observing at Skyhound gave a value of 15’ for the radius.^[21] A study by Nine *et al* (2020)^[22] of observations from the WIYN telescope gave an apparent cluster radius of 18’ suggesting 624 cluster members. The Messier catalogue gave a value of 16’ for the radius of NGC 7789.^[23]

2.3 Implications of the Results

Star clusters, namely old clusters, are shining examples of stellar evolution in action: the tip of the Red Giant Branch of a cluster is commonly used to determine the age of a star cluster. This works under the assumption that our models of stellar evolution are accurate, an assumption we justify by testing the models against real observations of evolving stars.

There has been much disagreement about one of our main results: the distance of the cluster M52 has been quoted to have a distance between 25 and 150Mpc^{[1][13]}. The reason for this disparity has been put down to non-uniform reddening across the cluster^[1]. The results presented here aim to provide evidence for a better understanding of this cluster. Reddening calculation is not only important for the calculation of accurate distance to the cluster, but can also be used to find accurate distances to other clusters using their relative brightness. This is an important technique when making sense of our galaxy, and how clusters might interact with each other^[24]. The initial mass function (IMF) of a cluster can be used to estimate cluster mass, which may aid in estimating the Galactic mass function.^[25] Star formation rate of the cluster can also be found along with the luminosity of the cluster from the IMF. These additional results were beyond the scope of this project. All of these results can allow one to conclude that investigating star clusters is a very useful tool in understanding galactic properties and exploring the history of the universe.

3 Methods

3.1 Observation

It was important to choose objects that would be sufficiently bright and in the right place in the sky for our observations. This was the basis of choosing our standard stars to calibrate from, SA 20-39 and 111-773. The clusters were chosen for similar reasons but also due to their interesting features. The chosen clusters were M52 and NGC 7789. Exposures of these stars and clusters were taken remotely using the PIRATE telescope. Calibration frames were also taken at the observation to help reduce the images of the objects and reduce the overall signal to noise in further calculations.

3.1.1 Choosing Standard Stars and Star Clusters

The selection of the standard stars took into consideration stars with well-known luminosity, as well as stars with appropriate altitude at time of observation. Similarly, the selection of star clusters took into consideration the altitude of the cluster candidates. Both altitude plots can be seen below in Figure 1.

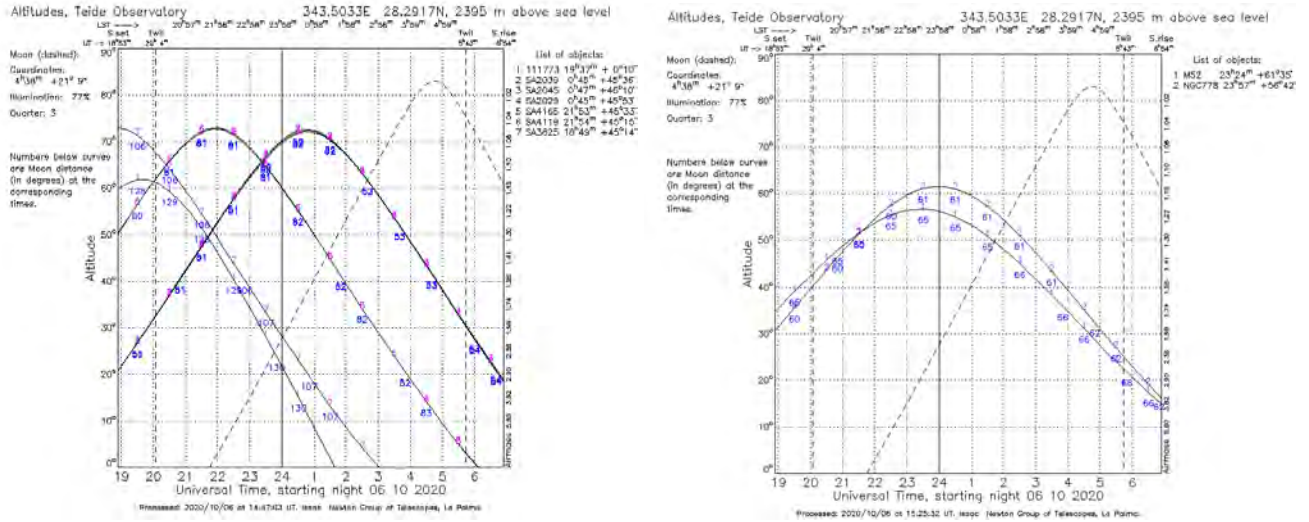


Figure 1: Altitude plots of the standard star candidates on the night of observing (left) and the two star clusters that were observed (right). The vertical dashed line indicates the observation starting time, and midnight marks the end of observation. Rising altitude after 2000 hours is deemed appropriate for observation.

Other criteria for cluster selection included clusters that were populous enough and had a significant proportion of stars still on the main sequence. NGC 7789 was selected for having a red population of stars, which implies significant evolution of its population. This provided a contrast to the younger M52. M52 was also selected for its merit of being well studied in the past: this gave a reference cluster to compare the results against, in order to highlight any major flaws with the analysis process.

On the night of 07/10/2020, the group convened virtually, and discussed the procedure of operating an Open University telescope^[26] through the internet. It was intended to take observational data on this night, but the weather was heavy rain at the telescope location. Instead, observation were taken on the night of 11/10/2020. The group reconvened and operated the PIRATE telescope on the island of Tenerife by using simple templates with right ascension and declination co-ordinates.

3.1.2 Star Cluster and Standard Star Observations

The group took initial exposures of the chosen standard stars and the star clusters, initially guessing the exposure times and analysing the output image in order to determine the best exposure time. This was done by checking whether the stars in the output images were saturated or not. Next, exposures centered on the clusters were taken to make sure the stars in the crowded field at the centre region were not saturated for the data analysis later on. In order to remove bad pixels from the observation, images of the star clusters were taken at three different offset pointings at 1" to each direction in the right ascension and declination.

For M52, 10x30 s exposure times were used in B and V-band at three different offsets, combining to 15 minutes in total. In U-band, it was 3x300 s at each offset, for 45 minutes in total. For NGC 7789, the images were taken for 15 minutes 3x5x60 s in the V and B-band and a total of 30 minutes 3x2x300 s was spent to take images in the U-band.

Two standard stars exposures of SA 20-39 and 111-773 were taken both at the start and at the end of the observation. These two standard stars were chosen explicitly because SA 20-39 has low elevation at the start and high elevation at the end of the observation night and vice versa for standard star 111-773 ¹.

3.1.3 Calibration Frames

Bias frames were taken with an exposure time of 0 seconds and were obtained automatically by PIRATE. After this, images of the twilight sky were taken for flat-field frames. The twilight sky was chosen as it is approximately uniform in brightness. By default, 60 s dark frames were also taken with a range of different exposures.

The observations taken can be found in greater detail in appendix A.

3.1.4 Data Organisation

The data obtained from PIRATE was downloaded on the CP Lab machines at the University of Edinburgh. It was then cleaned up and rearranged following the observing log that was written during the observation night (see appendix A). The individual image files for the reduction are FITS^[27] files. These hold an image header that encodes the information about the file and the details about the observation, such as band and elevation, and an array, which holds the image data.

For future brevity, "HDF" refers to the file used during for storage during data reduction, a *HDF5*^[28] file accessed through *h5py*.^[29]

3.2 Basic Data Reduction

Before performing any data analysis, images were reduced to improve the signal-to-noise ratio and remove artifacts. The overall process is show below in Figure 2.

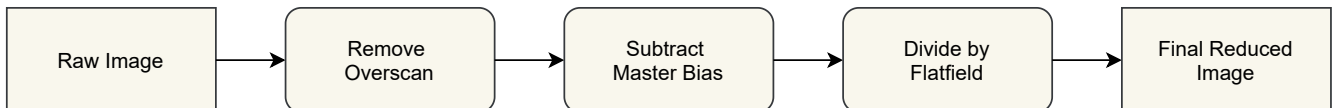


Figure 2: The steps of data reduction.

¹ 111-773 has high elevation at the start and lower at the end of the observation night.

3.2.1 Master Bias Frame

To counter readout noise in the CCD detector, a master bias frame was created. First, the overscan image border was removed from the edges of the images. The bias frames taken during observation were stacked in a NumPy^[30] array. To construct the master frame the mean of all these frames was taken. The master bias frame was then subtracted from all other images.

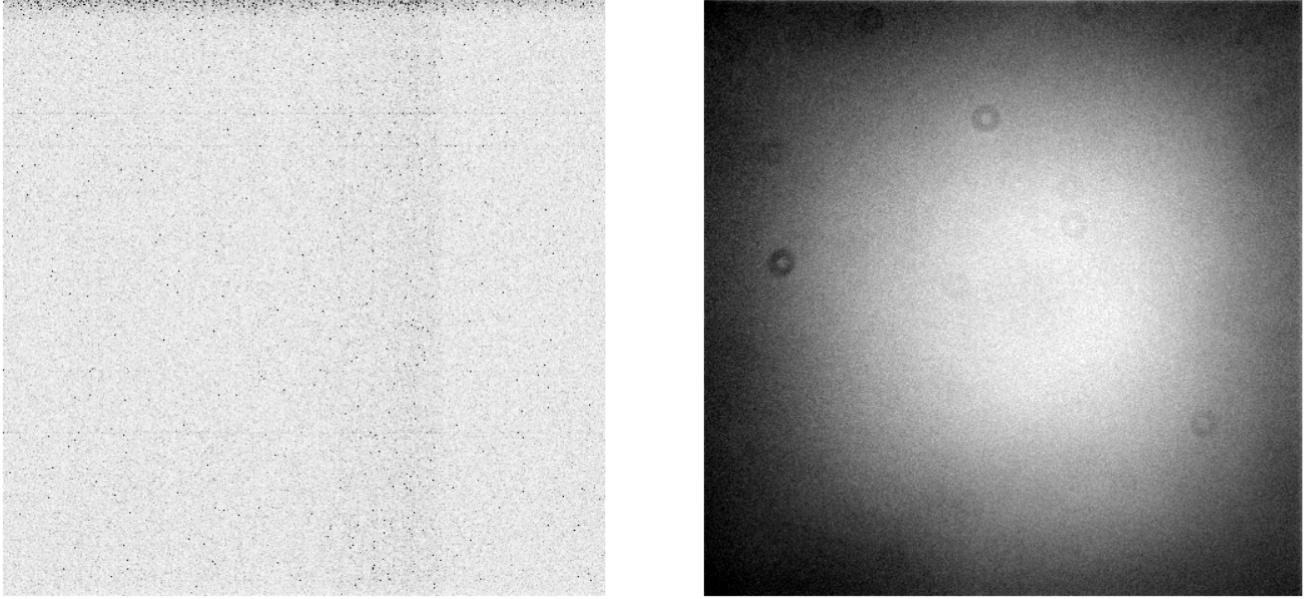


Figure 3: The master bias (left) with pixel intensity on a log scale and the flatfield in the V band (right) with pixel intensity on a linear scale. There is a very noticeable vignette on our flatfield which means there is heavy lens distortion of the outer field.

3.2.2 Flatfields

Flatfield frames were used to account for the difference in optical path length across the lens and remove the effects of dust. The master bias was subtracted from the flatfield frames and any images with saturated pixels were discarded from the calculation. A saturated pixel was defined as anything with an intensity of over 65,535 (maximum pixel value in the CCD of PIRATE). All of the flatfields were normalised by their means. Due to the work-from-home setup there were memory issues when reading in multiple FITS files to python^[31] so every flatfield was split into eight sections and each section was dealt with individually. The sections were stacked and the median value for each pixel was taken to remove the effect of extreme outlier pixels. The 8 sections of the final flatfield were then re-combined and normalised with the image mean. Images were divided by the flatfield after the master bias was subtracted from them.

3.2.3 Dark Current

It was assumed that dark frames would be unnecessary for the data reduction as the telescope dark current was low. To check this, dark frames were compared to a random cluster image by scaling up the dark frame exposure time to that of the image. The pixel intensity of the dark frames was found to be completely negligible and so was disregarded for further data reduction.

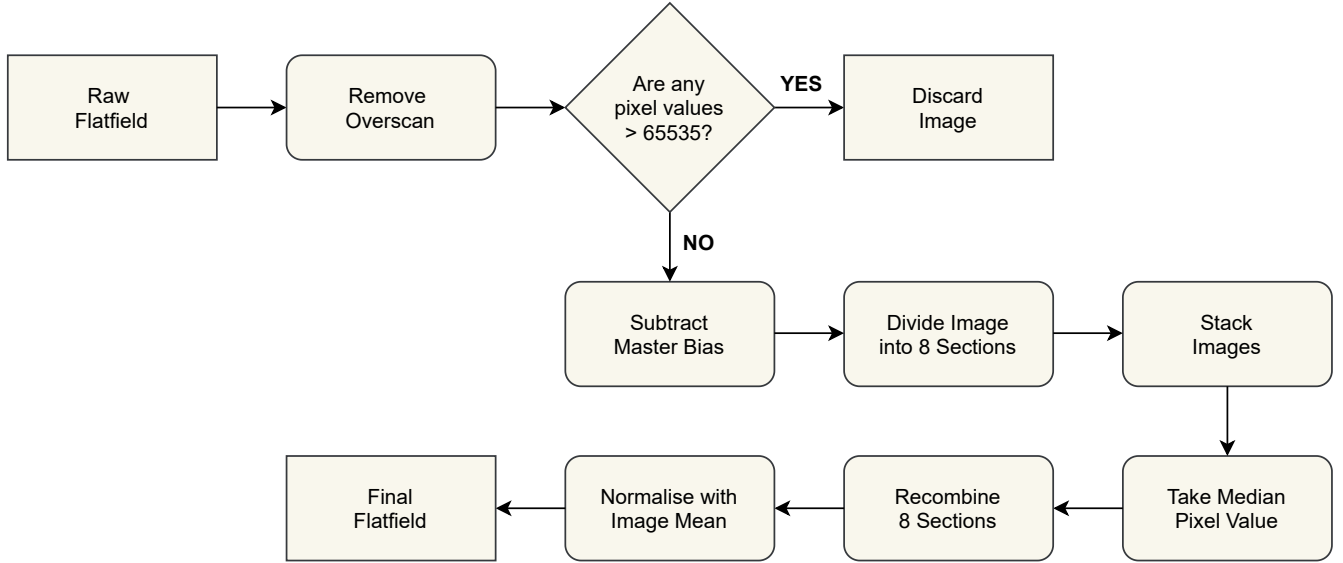


Figure 4: The steps taken to produce the flatfield frame.

3.3 Standard Star Calibration

Apparent magnitudes depend on a reference star unique to each reference system they are taken in. The aim of a reference system is to ensure that any observer, using any instrumentation at any location in the world, can record the same value m_λ for a target. Here we use the Vega system^[32]. In this system, apparent magnitudes are defined such that the apparent magnitude of Vega is zero for all passbands. The general equation for apparent magnitude for some passband λ is given by,

$$m_\lambda - m_{\lambda,v} = -\frac{5}{2} \log_{10} \left(\frac{f_\lambda}{f_{\lambda,v}} \right) \quad (1)$$

where m_λ is the apparent magnitude of the target and $m_{\lambda,v}$ is that of the reference star.^[32] f denotes the average spectral flux density observed for this passband, in units of flux per unit area per unit wavelength.

The passband denotes the region of the spectrum admitted for the observations, for this report being the U, B, V Johnson passbands^[33]. More generally, one can write,

$$m_\lambda = -\frac{5}{2} \log_{10} (F_\lambda) + z_\lambda \quad (2)$$

where F_λ is the time-normalized instrumental count taken by the recording instrument over the observations for the target, and z_λ defines a passband-dependent zero point that fixes the observation onto the reference system of choice.^[34]

F_λ varies with instrument used for observation of a given target as all instruments are unique in their response to a certain passband, and consequently z_λ will also vary with instrument. Local atmospheric effects also alter the value of F_λ , the atmospheric corrections being concerned with atmospheric absorption.

Instrumental count I_λ is a measure of the number of photons from the target that are recorded over the period the image of the target is taken, the integration. Aperture photometry is the preferred method for obtaining instrumental count from the image.

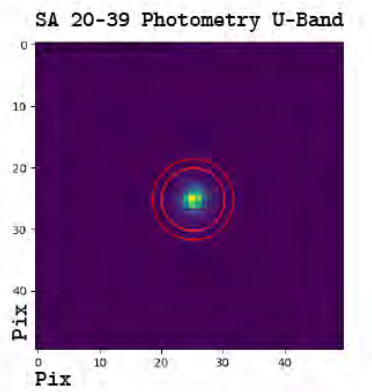


Figure 5: Example (clipped) image of a star, here the second standard-of-choice SA 20-39^[35]. Aperture photometry is demonstrated, aperture and inner annulus coaxial. The aperture clearly holds the flux of the target, and the annulus is noticeably faint. The density of the background in the annulus is calculated and used for background subtraction from the aperture.

3.4 Point Spread Function

A circular aperture was drawn about the target, from which the count $I_{\lambda,ap}$ was extracted as the sum of the values of all pixels within the aperture. See Figure 5 for an example. This included a contribution from the background count made up of stray diffuse light in the sky. An annulus was used for background estimation giving an estimated background density B_{λ} , either through a simple mean of the integrated flux of the annulus normalized to annulus area or more advanced methods. The full background contribution to the aperture can be found by multiplying the background density by the aperture area A_{ap} which returns,

$$I_{\lambda} = I_{\lambda,ap} - A_{ap}B_{\lambda} \quad (3)$$

Diffraction spreads the flux from the star over a given area, which blurs it, making stars appear as diffuse dots. The point spread function (PSF) is a quantity that describes this spread, unique to the instrument, and the convolution of the PSF with the unblurred field produces the observed data.

Generally the PSF is roughly Gaussian, and stars when imaged appear as diffuse circles that can be modelled as a 2D Gaussian in x, y pixel coordinates. The FWHM of such a Gaussian is $\approx 2.355\sigma$ to a good approximation.^[36]

3.4.1 Astrometry

Astrometry is the field of astronomy concerned with affixing a coordinate system to observations in space, this report being concerned with the ICRS coordinate system.^[34] This is usually done via plate-solving, roughly equivalent to repetitively overlaying images of the cosmos to the data in the hopes of finding one that overlaps, thus knowing which region of space your image lies in and allowing fixation of a coordinate grid in right ascension and declination, α and δ . α, δ are the celestial equivalent of longitude and latitude for the Earth.

Clearly apparent magnitudes are dependent on the distance to the target. Two stars of the same intrinsic properties will have different values of m_{λ} dependent on how distant they are to the earth, F_{λ} varying by an inverse-square law in distance^[34]. Absolute magnitudes are instead defined as being the apparent magnitude of the target were it at a distance of 10 pc^2 as opposed to the targets physical distance d , defined by^[34],

$$M_{\lambda} = m_{\lambda} - 5 \log_{10} \left(\frac{d}{10 \text{ pc}} \right) \quad (4)$$

²The parsec is defined as being $\approx 3.262 \text{ ly}$, ly being the light year.

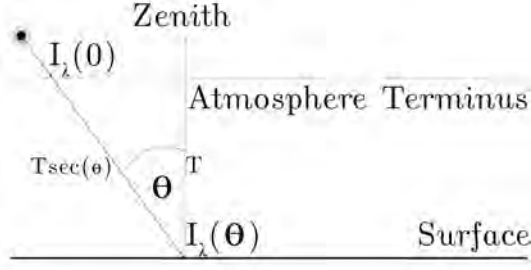


Figure 6: Illustration of optical paths taken by light from a target to the surface-bound observer. The path length scales approximately as $\sec \theta$, the airmass. For a zenith of zero degrees, the path length is proportional to the thickness of the atmosphere radially, T ^[37].

Light from the star must pass a distance S through the atmosphere to reach the surface, as shown in Figure 6. The instrumental count from a target reaching the surface following absorption is given by

$$I_{\lambda}(\theta) = I_{\lambda}(0) \exp(-\tau_{\lambda} \sec \theta) \quad (5)$$

where $\sec \theta$ is the secant of the zenith angle of the target, hereon airmass, and τ_{λ} is the optical depth, characteristic to the observation session and location. This is known as Lambert’s Law^[38]. $I_{\lambda}(0)$ is the instrumental count theoretically had above the atmosphere, the goal of our atmospheric absorption corrections. An accurate z_{λ} is contingent upon a reasonable atmospheric correction, otherwise z_{λ} would vary nightly for the observing instrument and time would be wasted with constant recalculation for the nights observing.

A single pass-band is considered here as an example to discuss the method by which τ_{λ} is calculated for both standard stars, 111773^[39] and SA 20-39^[35]. Atmospheric absorption corrections of their instrumental counts, and the deduction z_{λ} instrument will be discussed.

All code involved hereon is written in Python^[31] and run recursively for all provided standards, passbands, and elevations. ΔY indicates the error determined in any given quantity Y , while $\{Y_i\}$ will represent a set of values for some variable Y . All plots are produced using the `matplotlib`^[40] library unless otherwise noted.

3.4.2 Standard Star Photometry

All images were reduced appropriately. Following this, astrometric solutions are obtained via `Astrometry.net`^[41]. All astrometric fits were done using upload of `astropy`^{[42],[43]} `photutils.detection.IRAFStarFinder`, hereon `starfinder`, tables. This massively improved wait times for return of the astrometric fit, hereon the World Coordinate System (WCS) solution. The WCS solution allows conversion of image x, y to ICRS α, δ , and is encoded into the FITS header.

α, δ for the standard were taken from the appropriate reference catalogue^{[35],[39]} and were used to estimate the location of the standard in each image. The data is clipped to within ± 25 pix from the literature centroid. Using `scipy`^[44] a 2D gaussian was fitted to the target contained within the clip, estimating the FWHM of the target and better constraining the centroid for photometry.

Some example plots of FWHM vs. passband are illustrated in Figure 7. For each individual triplet of measurements, FWHM does not appear to vary massively, the U band differing from the V band by $\approx 10\%$. For this reason, it was decided that the fitted FWHM’s used for photometry would be 10% larger, to allow the same FWHM to be passed through reasonably for all three bands at the cost of a larger-than-necessary aperture for the V,B bands.

The package `astropy.photutils` was then used for simple aperture photometry of the standard in i . In units of FWHM, the aperture, inner and outer annuli have diameters of 3, 3 and 4 FWHM’s. An example image is shown in Figure 5 for SA 20-39 for the photometry of a data clip. The motivation for the aperture radius is that 3 FWHM’s should encompass virtually the entirety of the light from the target, and as such be a safe aperture choice. The error in I_{λ} was calculated via propagation of Equation (3), with the error in any given measurement from the

image assumed to follow Poisson statistics.^{[37],[34]} See appendix D.1 for propagation details. $\{I_{\lambda,i}\}$ was then saved to HDF for the next step in the processing pipeline.

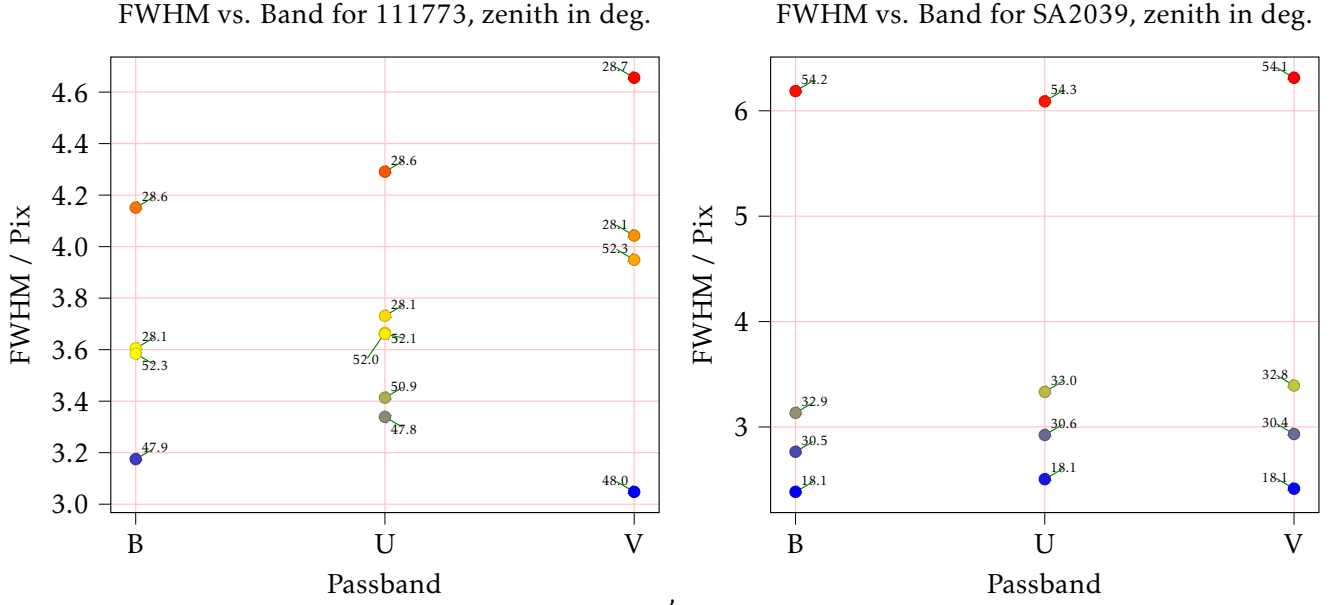


Figure 7: FWHM in pix vs. passband for 111-773 and SA 20-39. FWHM does not vary massively between the individual passbands, however it varies noticeably in each passband dependent on zenith angle, marked for each measurement.

3.4.3 Determining τ_{λ} & z_{λ}

Combining any two standard star measurements, each of which has unique airmass, it is possible to determine optical depth. Using Equation (5) and considering two different airmasses (images denoted i, j) for the same standard we find that:

$$\tau_{\lambda,(i,j)} = \frac{\ln I_{\lambda,i} - \ln I_{\lambda,j}}{\sec \theta_j - \sec \theta_i} \quad (6)$$

This was calculated for all unique combinations $i \neq j$. $\Delta \tau_{\lambda,(i,j)}$ is calculated appropriately via propagation of (6), see appendix D.2.

$\{\tau_{\lambda,(i,j)}\}$ is clipped against conditions of $0.2 \leq \tau_{\lambda,(i,j)} \leq 0.8$, with the remaining values sigma-clipped to $1-\sigma$ and the sigma-clipped mean used as the final value of τ_{λ} . This condition was chosen arbitrarily to fit the observed realistic range of τ_{λ} . $\Delta \tau_{\lambda}$ is set to $1-\sigma$, as for all reasonable values in $\{\tau_{\lambda,(i,j)}\}$ and the respective $\Delta \tau_{\lambda,(i,j)}$ was lower by at least an order of magnitude.

The atmospherically-corrected instrumental counts were then calculated using Equation (5) with errors propagated appropriately for all images i , giving $\{I_{\lambda,i}(0)\}$. See appendix D.3.

These were time-normalized with their errors against the integration of the images to give atmospherically corrected $\{F_{\lambda,i}\}, \{\Delta F_{\lambda,i}\}$. $\{z_{\lambda,i}\}$ was then calculated using Equation (2), and re-written as

$$z_{\lambda} = m_{\lambda,ref} + \frac{5}{2} \log_{10}(F_{\lambda}) \quad (7)$$

with reference values for $m_{\lambda,ref}$ taken for the standard from appropriate catalogues^{[35],[39]} and was sigma-clipped by $1-\sigma$, the mean taken as the accepted value z_{λ} . The error Δz_{λ} was taken as $1-\sigma$, with σ being larger than the propagated error by approximately a factor of 10 for all cases. We assumed negligible error in the reference values for m_{λ} .

3.5 Deep-stacking Cluster Images

In photometry, the signal to noise (S/N) ratio has marked significance. This is the ratio of the instrumental count that comes directly from the target against the error in this count, the error stemming from noise in the data, defined by^[34]

$$\frac{S}{N} = \frac{I_{\lambda}}{\Delta I_{\lambda}} \quad (8)$$

One method to increase S/N is by combining the data from multiple exposures of a target, so that noise is assumed to be random and with enough data it should smooth out. This is done by taking the simple mean of a set of images, summing the data and dividing by the number of exposures to get a stacked image with the same integration as the originals. For N aligned images $\{\Gamma_i\}$ of the same field, this “deep image” is given by,

$$\bar{\Gamma} = \frac{1}{N} \sum_{n=0}^N \Gamma_i \quad (9)$$

Note the stipulation of *aligned*: when observation is done, the telescope is aimed at some α, δ . This pointing typically does not remain perfectly accurate over multiple exposures, and thus when stacking images alignment is almost certainly required. Alignment may simply be translational, for example shifting an image j horizontally and vertically to align it to image i . In more complex cases, field rotation^[45] can plague image alignment, Alt-Azimuth^[34] telescope mounts being subject to this effect predominantly. The effect of field rotation is to rotate the imaging field over the night, and thus when aligning images taken using an Alt-Azimuth mounted telescope field derotation must also be done. PIRATE is one such Alt-Azimuth mounted telescope. See Figure 8 for a demonstration of alignment.

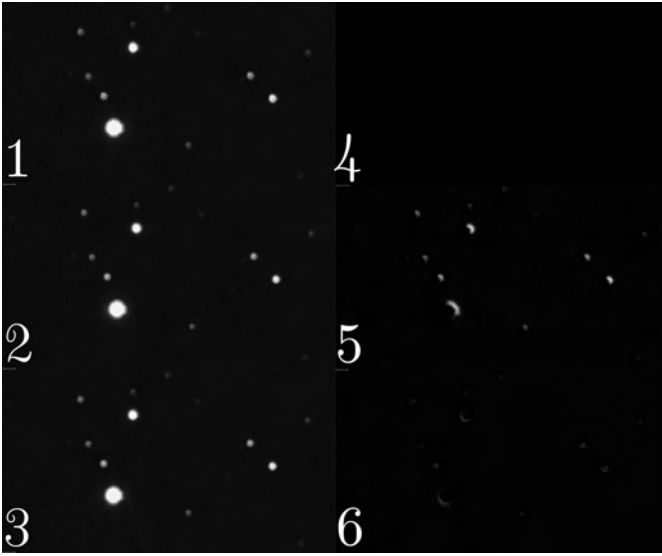


Figure 8: An example of the minor alignment issues encountered within each offset, here for the M52 V-Band, Offset 0. Here the issue is obviously translational, roughly 4 pixels. [1,2,3] are the zeroth sub, final sub, and aligned final sub, respectively. [4,5,6] are [1,2,3] subject to subtraction from [1]. For perfect alignment of a pair of identical images, one would expect a purely black image when subtracted from each other. Clearly [6] is darker than [5] overall, indicating that the local alignment routine is working. Images interpreted using *Aladin*^[46].

In astronomical imaging, offsets are utilized to minimize the effects of hot pixels and other imaging artifacts on the sensor. Using offsets results in hot pixels from one position on the sensor being spread over multiple positions

in the final mean stack of the field, rather than being concentrated in the original position of the hot pixel.

At this stage of data processing, deep images are produced for our clusters. For each cluster in our U,B,V pass-bands, the data consists of three offset fields, each field with a multitude of exposures, hereon sub-exposures. Novel code was written for alignment of images, both accounting for translational alignment and field derotation. The zeroth of any file directory denotes the first file within that directory. A single cluster was then considered.

3.5.1 Local Translational Alignment

For two images i, j not subject to field rotation in close translational proximity, the stars in the field should be approximately identical. Extracting sources in the field using starfinder returns a table of sources for each image, containing instrumental magnitudes and pixel coordinates \vec{r} .

Table j was clipped to not hold sources from within 10 pixels of the border, to ensure that the complementary source exists and was not past the image border in i . It was assumed the local offset between i, j was less than 10 pixels. The routine was written with small local offsets in mind, this is a safe assumption, with the routine in reality becoming inaccurate for offsets beyond ≈ 6 pixels in our usage case.

Roughly N sources existed in images i, j . For each source in i , a distance was calculated to each source in j . The source in j that minimizes this was chosen as the preliminary complementary source. The source must then pass the condition that the instrumental magnitudes differ by no more than an arbitrary value, chosen to be 0.25 Magnitudes, to finally be accepted as the complementary source. For this matched source, the vector $\vec{r}_s = \vec{r}_i - \vec{r}_j$ was calculated that maps from image j to image i , and was held in a NumPy array. The set of all $\{\vec{r}_s\}$ was then sigma-clipped and the mean was taken, and this mean translation was used to map image j onto image i by rolling the array by the translation required.

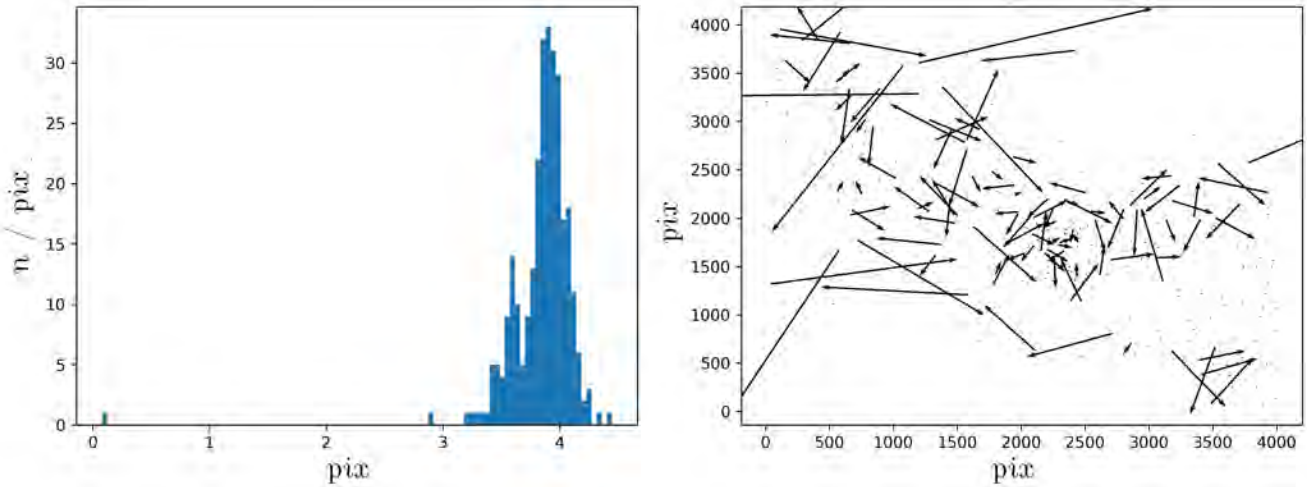


Figure 9: Left: The sigma-clipped histogram for the same stacking example: the sharp peak corresponds to the translation necessary to remap the image. Right: Example quiver plot for the local stacking routine, the same pair of images as in Figure 8. The multitude of small arrows are the “true” translational vectors required to align the offset, which are of similar magnitude and direction. The scatter of large random arrows are those of mismatched targets, and are expected to be random in direction and magnitude, as is observed: these are eliminated in sigma-clipping.

3.5.2 Offset Alignment

The aim of this was to align two images with a marked translational offset, alongside field rotation. First³ the field of j was de-rotated. The aim was to determine the rotation angle ϕ as illustrated in Figure 10.

Two arbitrary points in pixel coordinates were selected in image i to form a horizontal line, chosen as the image center and a point 500 pixels to the right, denoted a, b , forming a horizontal vector \vec{ba} . The image was plate-solved and ICRS coordinates for a, b calculated. The ICRS coordinates for a, b were then mapped onto pixel coordinates in the plate-solved image j , denoted a', b' , and the vector $\vec{b'a'}$ calculated. The angle ϕ between \vec{ba} and $\vec{b'a'}$ was calculated and j was de-rotated about its center using skimage.

Image translation was accounted for in a similar manner. The image center of i was mapped onto j via the same plate-solve method. The translation was determined via simply mapping the pixel coordinates, translating j by $\vec{aa'}$.

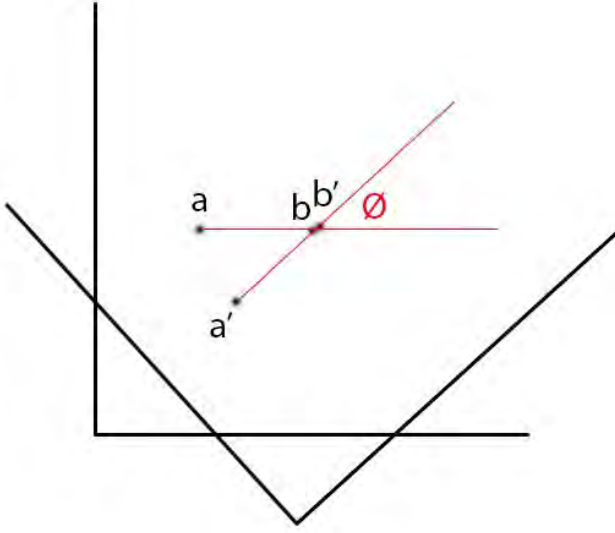


Figure 10: Accounting for field rotation. Here the primed image is rotated by ϕ relative to the unprimed image. If ϕ can be determined, derotation is readily possible.

3.5.3 Full Alignment and Stacking

For each passband, and for each offset, all sub-exposures were locally aligned relative to the zeroth offset. The assumption is that field rotation between the exposures for each offset is negligible: this held true in practice.

The sub-exposures were mean stacked, producing a deep offset image. The deep offset images were moved to a separate directory, where they were aligned relative to the zeroth offset. These images were once again run through local alignment. The motivation for this is that while the WCS solution may be accurate, it is not perfect and this step proved crucial. The set of deep offset images were finally mean stacked to produce the final deep cluster image for each passband, which was plate-solved automatically with a full upload of the FITS file for as accurate a solve as possible.

3.6 Cluster Photometry & CMD Diagrams

Stars occupy a discrete locus in stellar parameter space during their Main Sequence (MS) evolution.^[47] The parameters of $B - V$ colour and V-band absolute magnitude M_v , which when plotted together form a colour-magnitude

³The order did not necessarily matter, but the code will in the future be updated to do translation first to make the logic flow easier.

diagram, hereon CMD are important parameters.

An alternative parameter space widely used for the MS is that of $(U - B)$, $(B - V)$ colours. When plotted together for a population of stars, the resultant diagram is called a colour-colour diagram.

Stars spend most of their lives on the MS, burning hydrogen in their cores. Toward the end of their MS lives, stars track up the MS before turning off for their post-MS evolution. The turnoff point is unique⁴ to each star of some mass M and abundance ratio $[\text{Fe}/\text{H}]$, defined as

$$[\text{Fe}/\text{H}] = \log_{10} \frac{n_{\text{Fe}}}{n_{\text{Fe},\odot}} \quad (10)$$

where n_{Fe} is the Iron Abundance of the star, the fraction of the mass of the star concentrated in Iron. Hereon the metallicity will refer to $[\text{Fe}/\text{H}]$. While it will not be quoted with regularity, the units of metallicity are “dex”, the decimal exponent. MS evolution is not massively impacted by metallicity, but post-MS evolution is indeed impacted moderately by it^[48].

Using Equation (2) it can be seen that conventionally the more negative $B - V$ is, the brighter the star is in the B band as opposed to the V band. Intuitively this means the star must be hotter, as it emits more strongly in shorter wavelengths. This intuition is accurate and $B - V$ colour is significant because it may be accurately mapped to the effective temperature of a MS star. Absolute magnitude similarly tells us how luminous a star is intrinsically, as it can be directly compared to other known targets M_v , all of which for this parameter are at the same distance of 10 pc.

In this section extraction of photometry for our clusters in all available passbands, alongside preliminary star catalogue production are discussed. An application of our atmospheric corrections to the catalogue, and the arrival at our atmospherically-corrected star catalogues for each cluster are considered. The digestion Hipparcos-2^[49] data is used for comparison. A single cluster is assumed unless otherwise stated.

3.6.1 Source Selection

The brightest passband was used for source selection, here the V-band. Due to offset stacking, some regions of the field did not have a full stack of all the offsets. See the image edges in Appendix E as an example. This is more dramatic in the case of M52, where one of the offsets was mistakenly positioned at a larger distance than was required. We selected sources only from the valid regions, determined manually with the aid of *Aladin*^[46] and set for each cluster.

Starfinder was used to locate sources and identify their FWHM’s using a Gaussian kernel, with the FWHM adulterated by the same factor of 10% as for atmospheric corrections. The table was subsequently saved to HDF. The Starfinder was subject to several constraints, including:

1. Minimum peak threshold above which sources are viable. Sources less than this were not selected.
2. Sharpness, a measure of how “sharp” a source is. The peak flux minus the mean flux within the aperture, normalized to the peak flux.
3. Roundness, a measure of how round the source is. 1D Gaussians were fitted to each source by Starfinder along x, y , and the height h_x, h_y found. Roundness was defined as the difference divided by the sum for these quantities, where for our purposes we have used the absolute value.

Constraint [1] prevents starfinder from arbitrarily selecting every faint peak in the image: this was arbitrarily set to 20. Background counts across our images were upwards of ≈ 15 for the worst case, the U-band images of M52:

⁴For our purposes, we do not concern ourselves with any degeneracy that may be involved

the choice of 20 is just slightly above this worst case. This limitation prevented overly faint sources from being used.

Constraints [2,3] acted to prevent objects that weren't likely to be well-behaved stars from being selected. Arbitrarily, the conditions $1 \leq [2] \leq 2$ and $0 \leq [3] \leq 0.3$ were selected through visual examination of one of the sample catalogues starfinder produced.

3.6.2 Field Photometry

A single passband is considered here. The starfind table was read from HDF and the source coordinates extracted. Aperture photometry was then carried out for these sources.

A multitude of variations in the aperture photometry routine were trialled. Each routine had variation in choice of FWHM, background estimation, and target position corrections.

FWHM selection had two unique possibilities,

1. FWHM identical for all sources, as the sigma-clipped mean FWHM of the starfind table, fixed across passbands
2. FWHM variable for sources, as the FWHM from the starfind table, fixed across passbands

Background estimation had three unique possibilities, including

1. Simple Mean of annulus
2. Sigma-clipped Mean of annulus
3. Sigma-clipped Mean of entire field

Background estimation with [1] is as discussed previously for Equation (3). [2] differs in that the background density B_λ is in fact the sigma-clipped mean value of the annulus pixels. [3] instead used the sigma-clipped mean value of the entire field for B_λ , which was assumed to be dominated by the sky instead of stars.

Finally, target position estimation had two unique possibilities:

1. Original α, δ coordinates mapped into x, y of field
2. Original α, δ coordinates mapped into x, y of field, with subsequent localisation of the target

For re-positioning of a single target's aperture, sources were found in an arbitrary central region of a clip of the data, ≈ 40 pix wide, about the starfind coordinate. Figure 19 is an example of such a clip. The brightest source was used, and the aperture position for the clip was taken as being for the source's centroid. If the centroid x, y has shifted by more than an arbitrary tolerance from the starfind coordinate, chosen to be 5 pix, then the centroid was unchanged. Should this method fail the exception is caught and the centroid remains unchanged, though this did not occur in practice for reasonable sources.

Various combinations of the above possibilities in deducing a final photometry routine for our field photometry were explored. Following photometry, $\{I_{\lambda,i}\}$ were saved to HDF for the passband, along with $\{\Delta I_{\lambda,i}\}$: see Appendix D.1. θ and exposure time were also saved for future use. θ was taken from the first exposure that went to form this deep image and carried through in the image header since stacking.

3.6.3 Catalogue Production

Photometric data for all passbands was loaded and $\{I_{\lambda,i}(\theta)\}$ atmospherically corrected for $\{I_{\lambda,i}(0)\}$, with the error calculated accordingly: see Appendix D.3. Equation (2) was used to calculate $\{m_{\lambda,i}\}$ and $\{\Delta m_{\lambda,i}\}$: see Appendix D.4.

All information from each of the available passbands was then collated into a preliminary catalogue.

Preliminary CMD's using apparent B,V-band magnitudes were produced, alongside colour-colour diagrams, and the catalogue was subsequently passed on for further reduction.

3.7 Cluster Membership

Various methods were used to determine which objects were cluster members versus background stars in the image. Identifying cluster members would allow estimates of cluster radius, mass and age to be more robust and would also reduce the uncertainty on the reddening vector calculation.

3.7.1 Determination of Cluster Members Using Proper Motion

The proper motion of a star refers to the angular velocity which is seen as it moves across the sky. For star clusters the member stars have approximately equal proper motions as they were all formed from the same gas at the same time. This means that the proper motions can be used to determine which objects belong to the cluster versus the background.

A list of objects was taken from the GAIA Archive Data Release 2^[14]. The right ascension (RA) and declination (Dec) of the centre of the cluster and an estimate of the cluster radius was found from the literature and used to select objects (see Table 1). When selecting objects from GAIA, a lower magnitude cut of the g band magnitude was made. $g < 17$ was used as this was approximately the dimmest objects observed in our images. The GAIA tables were then cross matched with our objects by their right ascensions and declinations with a maximum error of 1" in the matching. Following matching, literature values of the proper motion of the cluster were used to determine the members. Cuts were performed for the proper motion within 1 and 2 x error tolerances of the literature value from the GAIA archive.

Measurement	M52	NGC7789
Centre RA / degrees	23 24 48.0 ^[50]	23 57 24.0 ^[51]
Centre Dec / degrees	+61 35 36 ^[50]	+56 42 30 ^[51]
Literature Radius / arcminutes	13' ^[19]	16' ^[12]
Proper Motion RA / mas/yr	-1.938 (147) ^[14]	-0.922 (140) ^[14]
Proper Motion Dec / mas/yr	-1.131 (154) ^[14]	-1.933 (130) ^[14]

Table 1: The literature values used for cluster membership determination.

3.7.2 Cluster Determination in aid of Extinction Coefficient - Visual Magnitude Cuts

In order to increase accuracy in the reddening/extinction coefficient calculation, it was important to use only the brightest stars on the main sequence. A table of these main sequence stars was made by determining the faintest

object in our cluster in the U-band from the cluster H-R diagram. The U-band was chosen to determine the cut-off as it had the lowest signal-to-noise ratio and so placed the constraint on our dimmest resolvable object. The graph was analysed by eye and cut-off values determined from where the colour axis featured only the main sequence. The magnitude cuts were then applied to the V band and a H-R diagram of this was plotted. The V band H-R diagram was then also cut with a minimum magnitude value determined again by-eye. For M52 and NGC7789 the minimum V-band magnitude values were taken to be **15.63** and **16.37** magnitudes respectively, and the B-V colour as less than **1.20** and **0.95**. This main sequence cluster table was then used for the reddening vector calculation.

Measurement	M52	NGC7789
V-Band Lower Limit / mag	15.63	16.37
BV-Colour Upper Limit	1.20	0.95

Table 2: The upper and lower limits used to determine cluster members.

3.8 Interstellar Extinction

Light emitted by stars is absorbed and scattered as it travels through the Interstellar Medium. The majority of absorption and scattering in the visible and infrared range is performed by dust between stars. This is referred to as interstellar extinction. Once the light reaches our planet, it travels through our turbulent atmosphere and is scattered again by N₂, O₂, and H₂O molecules. This is referred to as atmospheric extinction.

Fewer photons reach the receiver after extinction than they would otherwise: the perceived brightness, or flux, of the star to the observer has decreased. The amount by which the flux decreases due to extinction is not the same for all wavelengths of light: the difference in extinction between two adjacent bands of light (e.g. the B and V bands) is called the colour excess: $E(B - V)$. This quantity was used to determine the reddening vector of the cluster, along which the cluster was de-reddened.

Although the data had now been corrected for atmospheric extinction, interstellar extinction still needed to be taken into account to evaluate the true main-sequence turn-off of the cluster. The observed magnitude will be the sum of the star's intrinsic magnitude as observed from Earth and the amount of absorption measured in magnitudes. To find the magnitude without extinction, the absorption A_λ must be found.

$$m_{obs} = m_{true} + A_\lambda \quad (11)$$

The λ subscript describes the variation of extinction with wavelength. The extinction is larger at shorter wavelengths within the optical/infrared range so more blue light is absorbed by the dust and the light becomes redder.

To find A_λ , the colour excess can be defined:

$$E(B - V) = A_B - A_V \quad (12)$$

This is the change in colour between two bands due to the effect of differential extinction. Manipulating this equation gives

$$E(B - V) = A_V \left(\frac{A_B}{A_V} - 1 \right) \quad (13)$$

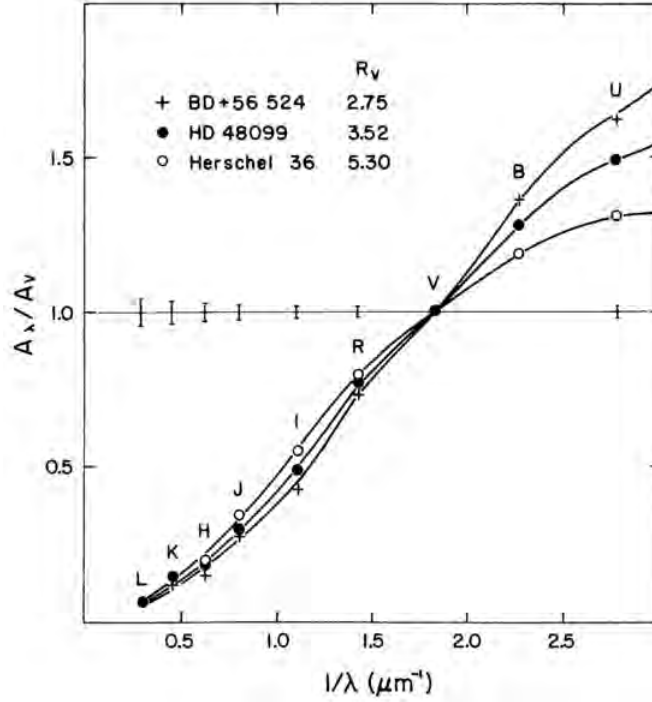


Figure 11: Extinction curve for optical/NIR regime from Cardelli *et al* (1989)^[11]. Shows roughly linear dependence for $1/\lambda$ making this an appropriate approximation.

A usual approximation to make here is that $A_\lambda \propto 1/\lambda$ in the optical regime. It is worth noting that this does not take into account the bump in absorption in the UV and the drop-off in the infrared due to dust re-emission as shown in figure 11. However, since the observations were performed using optical band filters, this is a valid approximation.

$$E(B - V) = A_V \left(\frac{\lambda_V}{\lambda_B} - 1 \right) \quad (14)$$

A well-informed choice of ratio of total-to-selective extinction, defined as $R = \frac{A_V}{E(B-V)}$, will give the best value for A_V . Here, the standard value for the diffuse interstellar medium, $R = 3.1$, was used for reddening calculations.^[11] Now $E(B - V)$ must be found. If the intrinsic B-V colour of the object is not already known, it can be found by use of a colour-colour diagram. A plot of (U-B) vs (B-V) will place the reddened, observed main sequence on the colour diagram. Plotting known main sequence star colours alongside this will reveal a shift in the main sequence as a result of reddening. The direction of this shift is determined by a reddening vector which has a slope calculated by:

$$\frac{E(U - B)}{E(B - V)} = \frac{A_B \left(\frac{\lambda_U}{\lambda_B} - 1 \right)}{A_V \left(\frac{\lambda_B}{\lambda_V} - 1 \right)} = \frac{\lambda_V \left(\frac{\lambda_B}{\lambda_U} - 1 \right)}{\lambda_B \left(\frac{\lambda_V}{\lambda_B} - 1 \right)} \quad (15)$$

again using $A_\lambda \propto 1/\lambda$.

Table 3 of Cardelli *et al* (1989)^[11] gives effective wavelengths for each filter as $\lambda_U = 2.78$, $\lambda_B = 2.27$, $\lambda_V = 1.82$ in units of μm^{-1} producing a reddening vector slope of 0.74324.

The observed main sequence can then be shifted back along the reddening slope until it sits on the intrinsic main

sequence. The amount of shift along the x and y axes give values for $E(B - V)$ and $E(U - B)$ respectively and thus A_V can be calculated.

A χ^2 test was performed to determine the optimal value of A_V where the observed main sequence was shifted to its optimal position to fit the intrinsic main sequence. The formula used to calculate the chi-squared value is as follows:

$$\chi^2 = \sum_i \frac{(r_{min})^2}{\sigma_i^2} \quad (16)$$

$$r_{min} = r_i - r_{actual} \quad (17)$$

where r_{min} is the minimum displacement of the stars in our cluster from the nearest star on the intrinsic main sequence, r_i is the positions of stars in our cluster, r_{actual} is the positions of stars in the intrinsic main sequence, and σ_i is the error propagated from the measurement of r_i .

3.9 Distance Determination

Once the magnitude of all the stars in M52 and NGC 7789 had been dereddened following their respective A_V values, the distance to both clusters was then determined by plotting a colour-magnitude diagram (BV diagram) of the clusters together with another main sequence of a different cluster with known distance. To do this, the main sequence of the Pleiades cluster (M45) was chosen due to its very low reddening and the fact that its distance is well-known from GAIA parallax measurement to be 135.8 pc^[15].

From the plotted BV diagram, the vertical shift which is necessary for the two main sequence to sit on top of each other is the *distance modulus* and was used to calculate the distance to our clusters, $d_{cluster}$, using the following formula:

$$m_{cluster} - m_{M45} = 5 \log_{10} \left(\frac{d_{cluster}}{d_{M45}} \right) \quad (18)$$

where $m_{cluster}$ is the apparent magnitude of the stars in our cluster, m_{M45} is the apparent magnitude of M45 cluster and d_{M45} is the distance to the M45 cluster. The left hand-side of equation 18 corresponds to the *distance modulus* and the distance, $d_{cluster}$ to both M52 and NGC 7789 in unit pc can be calculated from there.

The optimal value of vertical shift was determined using a χ^2 test; the vertical shift that has a minimum χ^2 value was chosen as our best estimate to calculate the distance to our clusters. The same formula was used from equation 16 and 17, changing the variables to be ⁵:

$$\begin{aligned} r_{min} &= \text{minimum vertical distance of the stars in our clusters from the M45 main sequence.} \\ r_i &= \text{apparent V-band magnitude of the stars in our cluster.} \\ r_{actual} &= \text{apparent V-band magnitude of the stars in M45 cluster.} \\ \sigma_i &= \text{errors in the V-band magnitude of the stars in our cluster.} \end{aligned} \quad (19)$$

The calculated distance to our clusters, $d_{cluster}$ was then compared with the distance calculated from GAIA parallax measurement^[15], d_{GAIA} using the formula:

$$d_{GAIA} = \frac{1}{\theta} \quad (20)$$

⁵ Assuming the apparent V-band magnitudes of the Pleiades stars have very small errors.

where d_{GAIA} is calculated in unit pc and θ is the parallax measurement of our cluster in unit $arcsec$.

3.10 Cluster Centre Estimation

3.10.1 Cluster Centre Estimation by Mean

To estimate the cluster centre, the right ascensions and declinations of all cluster members were averaged. The RA and Dec values were matched with the tables from the GAIA archive for the error on these measurements. The matching was done with an $1'$ error tolerance. The errors on the cluster centres were calculated by propagation of errors. An example of the equation is below for the RA coordinates, and the same process was applied for the Dec.

$$\sigma_{mean}(RA) = \frac{\sqrt{\sigma(RA_1)^2 + \sigma(RA_2)^2 + \dots + \sigma(RA_N)^2}}{\sqrt{N}} \quad (21)$$

An error estimate was also determined using histograms of the RA and Dec coordinates. The histogram data was then fit with a Gaussian curve and the sigma was found. From here the error on the mean was then found using the equation below, where N is the number of points and the same equation is used for the Dec coordinates.

$$\sigma_{mean}(RA) = \frac{\sigma(RA)}{\sqrt{N}} \quad (22)$$

3.10.2 Cluster Centre and Average Proper Motion Estimate by Kernel Density Estimation

Kernel density estimation (KDE) is a way to estimate the probability density function of a random variable in some parameter space. In this case the random variable is the position of the stars in the cluster in RA/Dec space and proper motion RA/ proper motion Dec space, and the KDE is estimating the location of the peak of the probability density function and hence the location of the cluster centre in both RA/Dec space and PMRA/PMDec space, and the average proper motion of the cluster.^[52] Code was written to represent each star by using a 2D Gaussian Kernel function, with a bandwidths of **0.25** and **0.05** for RA/Dec and PMRA/PMDec parameter spaces respectively using *scipy*^[44].

The proper motions were also determined using a KDE, the central value of proper motion was found, and for a perfectly symmetric, this is the average proper motion. Members are distributed roughly symmetrically in PM space, indicating good chance at correct PM estimation for cluster.

Errors on the estimates of the proper motion centroids using the KDE were determined by making radial density plots in proper motion space of the estimates, and estimating their full width half maximum (FWHM) by eye and hence estimated the sigma value by using the relation^[53],

$$FWHM = 2.355\sigma \quad (23)$$

3.11 Radius Estimation via Surface Density Plots

One of the initial goals was to provide an estimate for cluster radius and this was achieved with surface density plots. Plotting the surface density function would show a large surface density of bright stars near the centre of the cluster, which gradually decline to a background level. The radius value of this plateau is an approximation to the cluster radius.

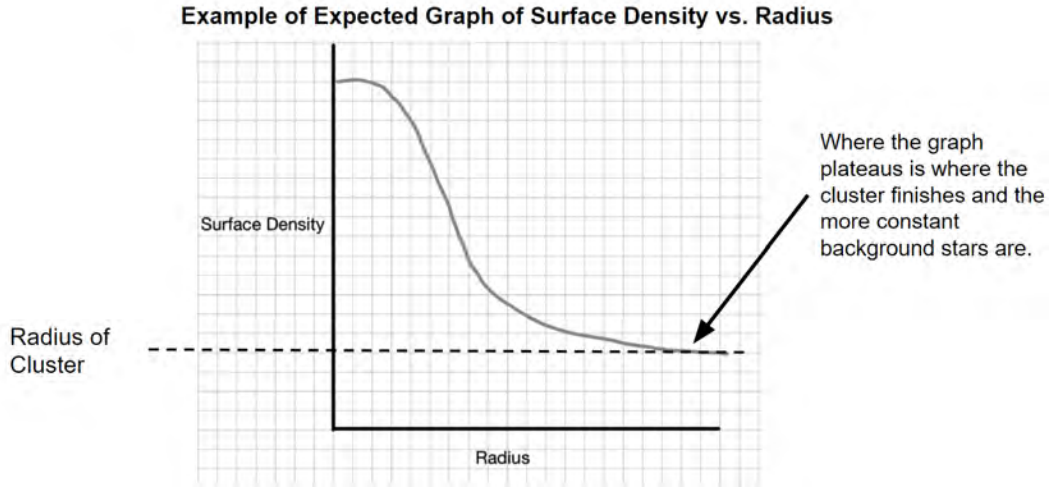


Figure 12: The radius can be estimated from the plot of surface density.

The surface density was calculated by summing up the number of objects within an annulus of and dividing this by the annuli area. Annuli increased by $\simeq 40''$ each step outwards depending on the magnitude value. This annuli size corresponded to 25 equally sized bins for each set of object radii. This curve was then fit with an exponential by the `scipy.optimize.curve_fit()` function in Python using a least-squares fit method. The background surface density was calculated using the total number of non-cluster members in the region of $r > 18'$. This limit was chosen as the largest radius used when doing cluster membership was $17'$ so it was reasonable to assume that past this point there would only be background stars present. The point of intersection of the background and surface density curve was taken as the value for the radius. The radius value was calculated over a range of magnitude cuts from lower limits of 16.0 - 12.5 and averaged to produce the final estimate.

The core radius, where surface density drops to 50% of its original value was also calculated.

The error on the radii of the clusters was determined by taking half of the range of estimates given by different magnitude cuts.

3.12 Isochrone Fitting

An alternative to estimating the turnoff by simply guessing the spectral class of stars about it is to fit an isochrone to the observed CMD. Isochrones delineate a locus that holds stars of the same age. This was the preferred method for estimating the age of a stellar population. These are often pre-calculated and available in stellar grids, massive tables that hold a menagerie of properties of numerical simulations of stellar evolution.^{[54],[55]} Some example isochrones are available in Figure 13.

In this section, a final catalogue for each cluster was produced, alongside their final de-reddened CMD's along side their absolute V-band magnitudes. Cluster age estimation was presented by geometrically fitting PARSEC/
COLIBRI^[56] isochrones to our data in $(B - V), M_V$, hereon CMD, parameter space. A brief overture is presented into alternative isochrones, using MIST^[57] isochrones in both CMD and $\log T_{eff}, \log L$, hereon log-log, parameter space. A single cluster is assumed throughout.

3.12.1 Final Catalogue

Once extinction values A_V and error ΔA_V had been calculated and membership estimated, the preliminary catalogue was revisited and trimmed down to the confirmed members, with *GAIA DR2* data for the confirmed mem-

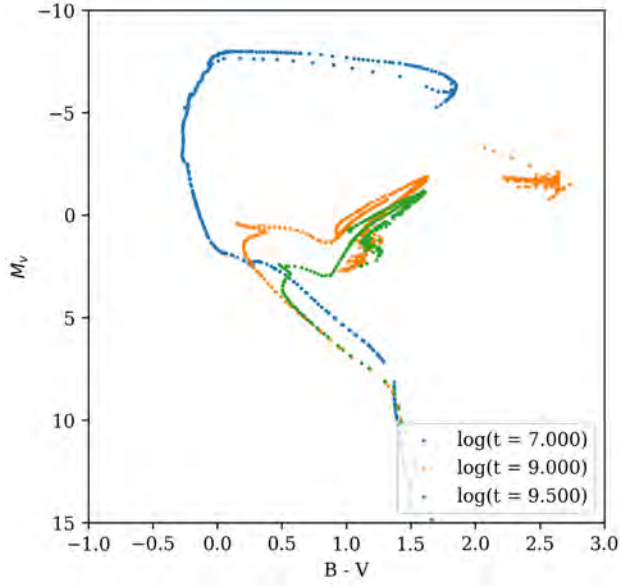


Figure 13: Illustration of a trio of isochrones in colour-magnitude form, taken from the PARSEC/-COLIBRI^[56] stellar grids. Ages of 10 My, 1 Gy, 3.16 Gy with $[\text{Fe}/\text{H}] = 0$ dex are shown. For the rather young population of 10 My, of which lighter stars are still settling into the MS locus, evolution has clearly progressed rapidly for massive stars: within 10 My many are already well on their way through their post-MS evolution, which occurs on timescales far shorter than t_{MS} . For the older populations of 1 & 3.16 Gy, the MS locus is clearly defined, and the turnoff point is clearly tracking down the MS as evolution progresses.

bers added.

Absolute V-band magnitude M_V was calculated and errors appropriately propagated: see appendix D.5 for details. M_V and $B - V$ colours were dereddened and errors calculated, see appendix D.6. Final CMD's were produced for the catalogue.

3.12.2 Geometric Isochrone Fitting

Geometric fitting of precalculated isochrones was used to give an estimate of cluster age as opposed to more traditional methods, taking inspiration from previous examples of this method.^{[54],[55]} Weighted least-squares fitting was used, with perpendicular offsets employed.^[58]

Let $\{y_i\}$ be the dataset and $m(t)$ represent the spline corresponding to the linearly-interpolated model isochrone of age $\log t$. The function to minimize, R^2 , is defined as,

$$R^2(t) = \sum_{n=0}^N w_i \left[\frac{\min|y_i - m(t)|}{\Delta \min|y_i - m(t)|} \right]^2 \quad (24)$$

where the weighting set $\{w_i\}$ is arbitrarily selected so as to maximize the accuracy of the fit. y_i is some data point defined for x_1, x_2 in parameter space. For our usage case x_1, x_2 were either the observables $(B - V), M_V$ or $\log T_{\text{eff}}, \log \frac{L}{L_{\odot}}$, mapped from our observables using the interpolated Rochester Modern Mean Dwarf Catalogue.^[59]

The error in the perpendicular distance to y_i from $m(t)$ ⁶ was taken as the maximum possible error for that point, as,

$$\Delta \min|y_i - m(t)| = \sqrt{(\Delta(B - V))^2 + (\Delta M_V)^2} \quad (25)$$

⁶Where this is $\min(y_i - m(t))$

The error in the extinction ratio was assumed to be negligible to other errors in our reduction.

In instances where parallax was not available from *GAIA DR2* for a target and hence M_V not calculable, the data point was ignored from all analyses. In future implementations, using a comparable parallax from another cluster member may be an alternative option that may allow a rough preservation of the data point at the cost of assuming that the data point indeed lies in the cluster.

The model $m(t)$ takes the form $m(t, ([Fe/H]))$. The second variable was fixed for each run of the routine to simplify this process, relying on manual comparison of the produced plots of R^2 to estimate which $[Fe/H]$ provides the most reliable plot for $R^2(t)$. $R^2(t)$ was generated about the literature range of values of $\log t$ for the cluster for some time-step $\Delta \log t$.

The produced curve for $R^2(t)$ was smoothed using a `savgol`^[60] filter to eliminate excessive jitter in the data.

3.12.3 Isochrone Error Estimation

For error estimation, the equivalence between $R^2(t)$ and χ^2 was assumed, and the minimization^[61] of χ^2 was used to estimate error.

Let $\{O_i\}$ data with expected values $\{E_i\}$, where each data point is considered as a single bin, and define,

$$\chi^2 = \sum_{i=1}^N \frac{(O_i - E_i)^2}{\sigma_i^2} \quad (26)$$

where σ_i^2 is the variance in the data point O_i and N defines the number of data-points.^[61] The degrees of freedom k were defined for χ^2 as the number of independent variables that our calculation depends upon. For the usage case, $k = 1$: $E_i = E_i(t)$.

In relating χ^2 to $R^2(t)$, it was assumed that the difference between O_i and E_i was their geometric separation in parameter space⁷, σ_i^2 defined similarly.

The assumption of $R^2 = \chi^2$ was tenuous, less so if $\{w_i\}$ was equal to unity, in which case $\chi^2 \approx R^2$. This assumption was further skewed by the fact that in χ^2 minimization, `savgol`-filtered $R(t)^2$ was used. For this purpose, the window length and number of smoothing iterations were both kept as low as reasonably possible.

The final errors were defined using standard χ^2 distribution tables, with confidence intervals estimated.^{[53],[62]} The estimated the final error in $\log t, t$ was half the width of the 3σ confidence interval, despite asymmetries that present themselves in such intervals during χ^2 minimization.^{[53],[61]}

3.13 Initial Mass Function Fitting

When a star cluster undergoes formation, stars with a wide range of masses are formed. Considering the cluster as a whole, it is possible to define the Stellar Initial Mass Function, hereon the IMF.

The IMF $\xi_I(m)$ is defined such that $\xi_I(m)\Delta m$ is the number density of stars within the mass range $[m, m + \Delta m]$ in the cluster at the time of formation.

The IMF is only observable about the time of initial formation for the cluster. When observing star clusters, we see the PD MF: the Present-day Mass Function. Analogous to the IMF it defines $\xi(m)$ but for the present day, ξ_{pm} .

⁷This is the perpendicular distance on the colour-magnitude diagram from the data-point to the isochrone.

In lower mass ranges, the PDMF is approximately equal to the IMF.^[63] We may deduce an explanation for this by assuming the star cluster only produces stars at formation, we fix the size of our stellar population and its contents.

Massive stars rapidly evolve and reach their demise, with less massive stars surviving with low mass loss until the present day. The original population is relatively unchanged for less massive stars which reside at their relatively constant positions on the MS, while the PDMF for more massive stars will likely be significantly lower than the IMF for the same region as these stars have all effectively died off.

Naturally star birth continues even after cluster formation, which may give rise to faults in assuming the PDMF is equivalent to the IMF, however it is a reasonable assumption for less massive stars. Hereon we will interchangeably use PDMF and IMF, as $\xi(M)$.

The general form for $\xi(m)$ is given by the Salpeter IMF.^[64] This form of the IMF was discovered empirically based on the solar neighbourhood, and is given by,

$$\xi(m) \left(\frac{\Delta m}{M_{\odot}} \right) = \xi_0 \left(\frac{m}{M_{\odot}} \right)^{-\alpha} \left(\frac{\Delta m}{M_{\odot}} \right) \quad (27)$$

where ξ_0 is a constant related to the stellar number density of the cluster. α is a positive constant dependent on the mass range being studied, traditionally taking the value of $\alpha = -2.35$ for stars on mass scales comparable to the sun. Most of the mass of a cluster must be concentrated in the lighter stars, as so few larger ones will exist due to the power-law nature of the IMF.

In this section, the obtained PIMF's for our clusters alongside their overplotted Salpeter IMF's are presented. The integrated masses for our clusters, given some assumptions, are also estimated. Unless otherwise stated, only one cluster is considered at one time.

3.13.1 Obtaining and fitting an IMF

The catalogue for the cluster members was first retrieved, with V-band absolute magnitudes extracted. Utilising the Rochester catalogue, it was interpolated and the mass as a function of absolute V-band magnitude was found. The V-band absolute magnitudes were mapped into mass using this function, with the assumption being that all the mapped data-points lay squarely on the MS locus given by the Rochester catalogue.

The masses for all cluster members were binned to produce a histogram in some range, and the median mass for each bin calculated, bin-size tuned to produce a reasonable looking histogram, and resembled what would be expected for the Salpeter equation (27).

The peak of the histogram was used using Equation (27) to estimate a value for ξ_0 for the cluster.

3.13.2 Integrated mass estimation

The IMF ξm describes the number density of stars between some finite mass range $[m, M + \Delta m]$. In the reduction, this density was defined as the total number of stars within this mass range for the volume of the entire cluster. Hereon it was assumed m represents the mass of some star in units of M_{sun} to simplify.

Using equation (27) and assuming a valid mass range $[m_1, m_2]$ for the integration, the total cluster mass^[65], M_C , was found using,

$$dM_C = m\xi(m) = \xi_0 m^{1-\alpha}$$

$$M_C = \xi_0 \int_{m_1}^{m_2} m^{1-\alpha} dm = \frac{\xi_0}{2-\alpha} \left[m^{2-\alpha} \right]_{m_1}^{m_2} \quad (28)$$

$$(29)$$

A value of M_C for each cluster was found. In this deduction, it was assumed ξ_0 was as previously estimated, with the usual $\alpha = 2.35$. The standard lower mass limit where it was typically accepted that $\alpha \neq 2.35$ is $\approx 0.5M_\odot$.^[65] This limit was used as M_1 in our integration, setting M_2 to infinity.

An estimate on the total observed stellar mass of the cluster was placed, by summing the masses for all observed stars. This mass was expected to be significantly lower than the literature value, as only a portion of all the stars in the cluster were sampled.

4 Results and Discussion

4.1 Observation

The final reduced images of the clusters are shown in Figure 14. Referring to images of the clusters found on Aladin which are shown in Figure 15, they look similar and therefore the final reduced images have been a success.

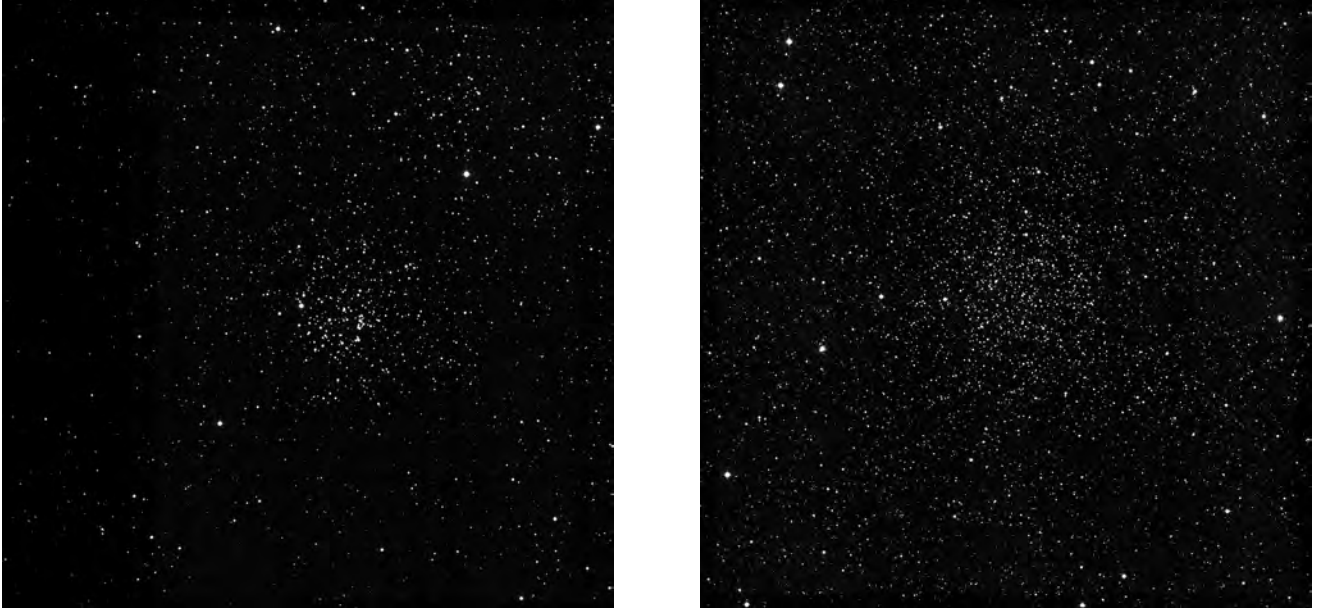


Figure 14: Our final reduced images from our observations. Field of view for these images is $43' \times 43'$.

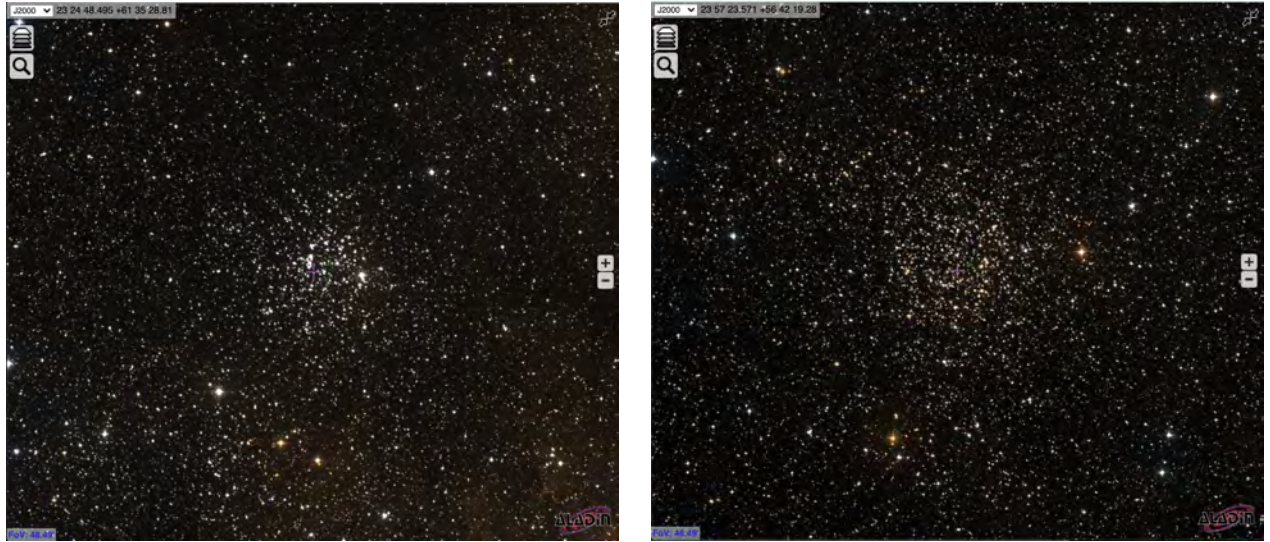


Figure 15: Figures from Aladin with both image's field of view at $48.49' \times 48.49'$. On the left is M52 and on the right NGC7789.^[46]

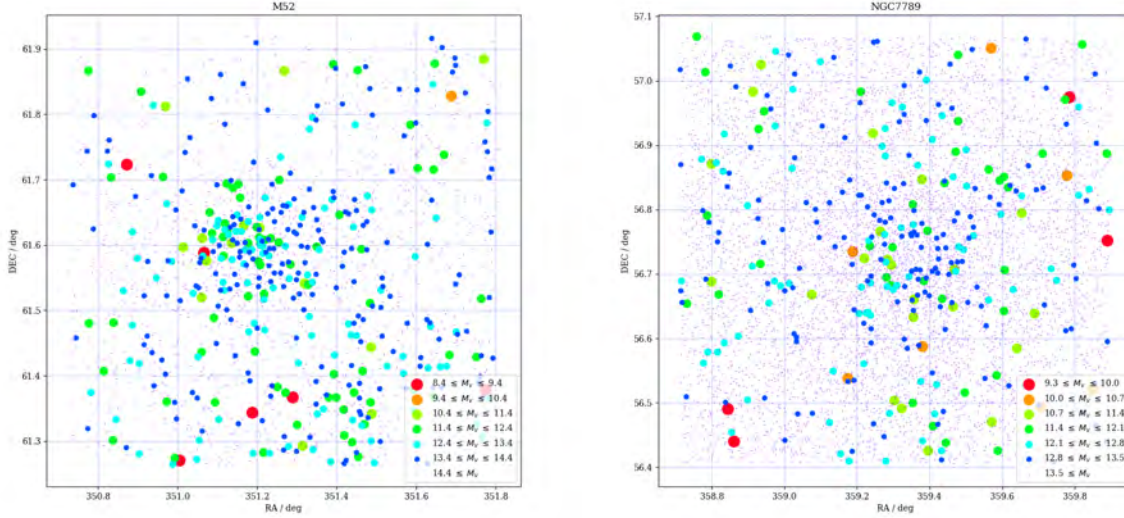


Figure 16: Illustration of sources observed in the fields for M52 (left) & NGC 7789 (right), magnitudes illustrated by point area. These illustrations have been atmospherically corrected.

4.2 Standard Star Calibration

The code was run for all available data for the standard stars 111-773 and SA 20-39. The resultant $\{\tau_\lambda\}$ and $\{z_\lambda\}$ for 111-773 are demonstrated in table 3. In the case of SA 20-39, the code failed to produce a coherent result for $\{\tau_\lambda\}$.

In speculating the reason for this failure, the altitude plots in Figure 1 were first considered. We see that zenith θ decreases for SA 20-39 over the observing session. In terms of the expected value of (atmospherically uncorrected) instrumental count $I_\lambda(\theta)$ given by equation 5, it was expected that observed I_λ was to only increase over the observations. This was not satisfactorily observed.

Passband	τ_λ	$\Delta\tau_\lambda$	$\frac{\Delta z_\lambda}{z_\lambda}$	z_λ	Δz_λ
U	0.573	0.018	0.031	18.258	0.012
B	0.411	0.005	0.012	20.526	0.007
V	0.313	0.008	0.026	20.501	0.001

Table 3: Optical depths τ_λ and zero-points z_λ for observations of standard star 111-773 with their propagated errors.

Atmospheric seeing^[37] or other observational anomalies may have impacted the result, as reduction proceeded perfectly for the well-behaved data of 111-773. See Figure 17 for an example of the anomalous instrumental counts observed from SA 20-39, paired with well-behaved data for 111-773 which varies monotonically for the observations as expected.

To further investigate whether seeing was responsible for the anomalous results of SA 20-39, one plausible method would be to atmospherically correct the instrumental counts for each image, and then estimate their standard deviation σ . If σ were notable relative to the counts, it would imply that the optical depth was varying on timescales less than that of the observation session^[34] in the vicinity of SA 20-39, a sign of atmospheric seeing.

As valid results only existed for the reduction of data for 111-773, these results were used and SA 20-39 disregarded from future analyses. SA 20-39 was not revisited as clearly the observations were plagued by some observational factor that would preclude any reliable reduction of the data.

Observation	111-773	SA 20-39
1	289385	354960
2	288742	341401
3	257863	373384
4	247109	356605

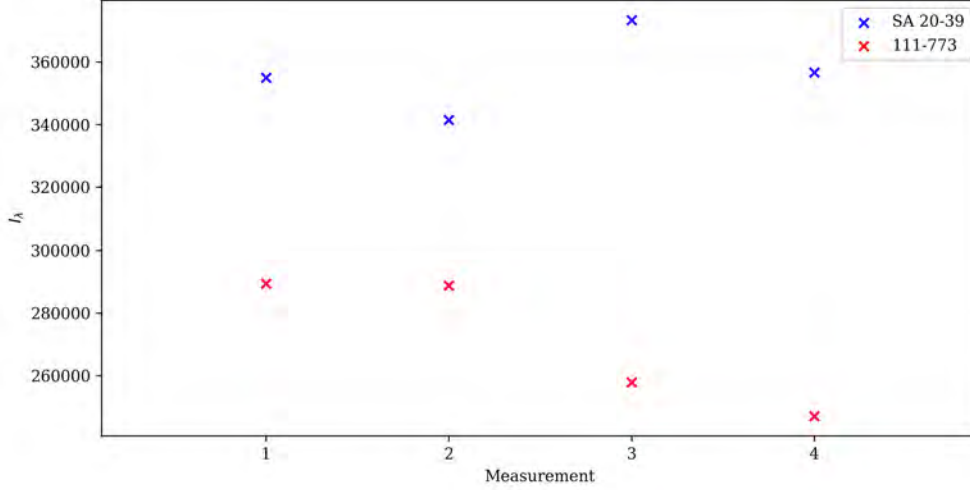


Figure 17: Top: Table for instrumental count I_λ for raw V-band photometry of 111-773 and SA 20-39. Bottom: Graphical representation of this table. Defying expectations, I_λ for SA 20-39 decreased in certain instances for later observations. It is thought this may be due to seeing, as all calibrations and processing proceeded unhitched for 111-773, which was well-behaved. Similar results are observed for the B, U pass-bands.

4.3 Deep Stacking

IRAF^[66] was trialled for stacking, namely `xregister` and `wregister` for identification of the transformations necessary for alignment. This did not succeed for our usage case, motivating the use of novel code.

The stacking routines trialled produced satisfactory results. Final deep images for our cluster may be viewed in Appendix E. An example of how efficacious local stacking routines were can be seen in Figure 8.

In future implementations of the local stacking routine, using `scikit-learn` to effect translation would be more suitable as it allows flux-preserving array translation by non-integer values. Our translation method relied upon rolling the array the integer pixel translation calculated, which inherently limits the precision of stacking: only integer translations were possible.

Overall there were no issues, however in applying these routines, several performance concerns were addressed.

Local alignment is processor intensive in that it scales with N^2 sources in the field. Offset alignment requires WCS solutions, which require upload, wait, and download times to the `Astrometry.net` API. Multiprocessing was used to hasten the process, allowing multiple offsets in multiple passbands to be worked simultaneously. This

massively sped up processing times, especially with regard to plate-solving.

4.4 Photometry

4.4.1 Source Selection

Source selection is visualized in Appendix F for both clusters. Clearly the field number density is larger for NGC 7789 than for M52. NGC 7789 also appears denser and larger than M52, which is as expected: NGC 7789 is an older cluster than M52 and is also larger in size^{[67],[16],[1],[18]}. An improvement to source selection would have been to use lower thresholds for sources: clearly more sources may have been extracted for M52 but weren't.

4.4.2 Photometry

The final photometry routine that was used for all data reduction consisted of variable FWHM's with simple mean background estimation, paired with re-positioning of the aperture center.

Using identical FWHM's for all sources lead to slightly underestimating the instrumental count for larger-than-average targets. Source-dependent variable FWHM proved the most viable, giving suitably sized apertures unique to each source across all passbands. The difference was marginal but noticeable in the data by eye.

Background estimation by simple annular means proved the most reliable for the final reduction. The sigma-clipped background density for the entire field was used, which was assumed to be dominated by the sky instead of stars. This assumption that the sky dominates the background proved reasonable, providing comparable results to using simple annular means. An example histogram showing approximately Gaussian distributions for the background count of our data is illustrated in Figure 18 showing what is typically expected for sky background^[34].

Using sigma-clipped aperture means for background density proved extremely unreliable. For each matched cluster data-set $\{(V_i - G_{i,BP})\}$ was calculated and the standard deviation σ taken for the brightest 500 members. GAIA G_{BP} and Johnson-Cousins V passbands have roughly the same effective wavelength^[68] and consequently we expect a low σ to indicate good photometry. Simple aperture means gave σ of 0.3, 0.1 for M52, NGC 7789 respectively, while sigma-clipped aperture means gave $\sigma \geq 2$ by-eye for all matched members. This difference from GAIA DR2 photometry was the deciding factor in not using sigma-clipped aperture means.

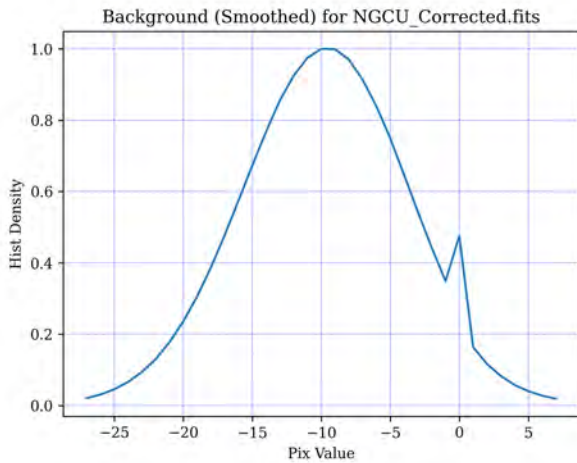


Figure 18: Smoothed normalized histogram for NGC 7789 U-band deep image array, clipped to $1 - \sigma$ about the sigma-clipped median. Clearly image calibrations and stacking have been successful, as the background density lies close to 0 with the majority of the image being dominated by the counts that lie within the domain of this approximately-normal histogram. This data was the worst-behaved of all deep images with regard to calibration.

The astrometric fits in the data varied by upwards of $\approx 2''$. This can be seen in Figure 19. The starfind coordinate mapped to the data for the target is clearly not in the same location as it's centroid. The effect of this positioning

error was minor and indeed did not prove to be a barrier to data reduction, but was nonetheless accounted for with source re-positioning used.

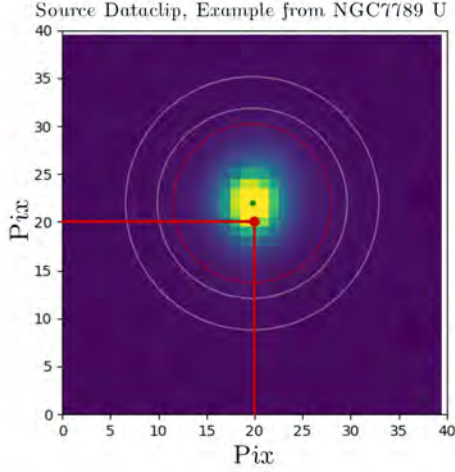


Figure 19: Dataclip for an example target in the U-band, for NGC7789. The clip is centred upon the starfind α, δ . Clearly the target is not at the starfind coordinate: the WCS solution differs between each passband for the cluster. This requires recentering of the aperture centroid locally to better capture the flux of the target.

In future implementations of this method, it would be ideal to use the average shift required to remap the centroids to estimate the difference in the astrometric fit between passbands: with larger sets of images, it may allow estimation of the error in their astrometric fits.

4.4.3 Preliminary CMD's

Preliminary CMD's are given in appendix G. The morphology of these CMD's matches that of CMD's produced using *GAIA DR2* data for the cluster's local neighbourhoods indicating good photometry and standard star calibrations, although these do not match precisely due to differences between our pass-bands and those of *GAIA*. *GAIA DR2* These CMD's are provided in appendix I. The presence of the Red Giant Branch for NGC7789 as a distinct feature in our observed preliminary CMD about $(B - V), V = (1.05, 13.2)$.

Preliminary colour-colour diagrams have been produced, given in appendix H. For both clusters, the presence of a large plume of data-points was notable. These points correspond to relatively faint data with large uncertainties in their U-band magnitudes.

Assuming Poisson errors, in which a count of N has error \sqrt{N} , S/N should approximately scale as

$$\frac{S}{N} = \frac{\Delta I_\lambda}{I_\lambda} = N^{-\frac{1}{2}} \quad (30)$$

I_λ is noticeably lower for the U-band when compared to the B,V passbands for the data. Consequently, the fractional error for the U-band is expected and indeed has been observed to be noticeably greater than that of the B,V passbands, as $N_U \ll N_{B,V}$ and hence $N_U^{-\frac{1}{2}} N_{B,V}^{-\frac{1}{2}}$.

4.5 Cluster Membership Determination

Method	Number of Objects	
	M52	NGC7789
Proper motion - 1 x error tolerance	209	529
Proper motion - 2 x error tolerance	396	1033
Visual magnitude cut	781	1976
Literature Value	193 ^[69]	624 ^[22]

Table 4: Cluster members for each method.

4.5.1 Determination of Cluster Members Using Proper Motion

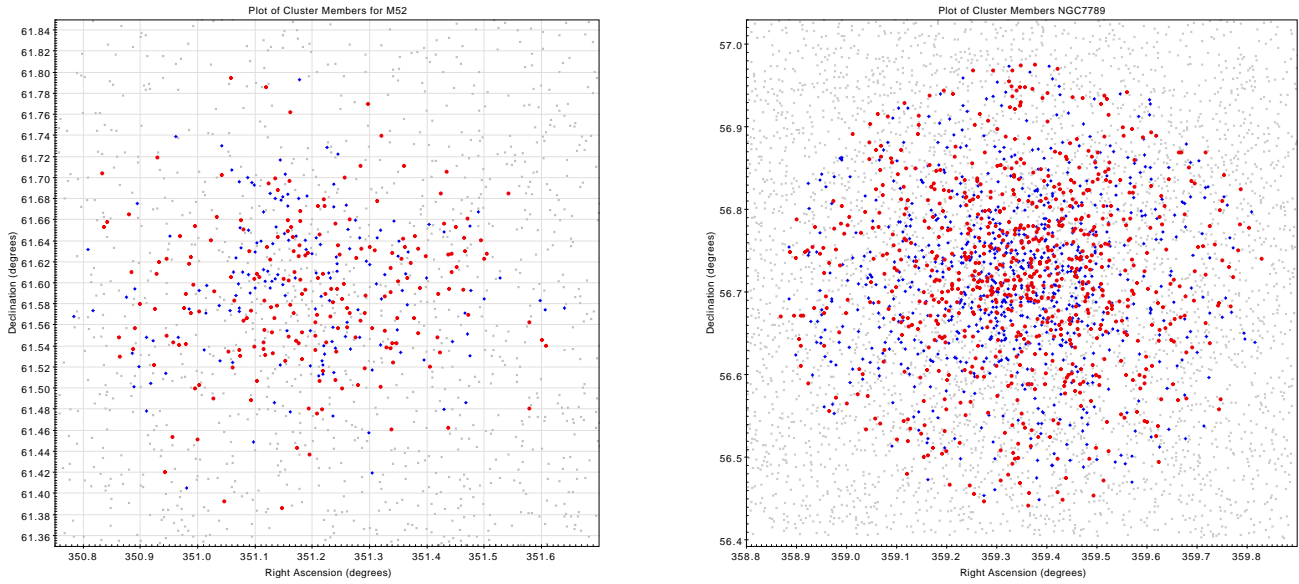


Figure 20: The cluster members of M52 (left) and NGC7789 (right). Cluster members from a 1 error tolerance are shown in red and a 2 error tolerance in blue with background objects in grey.

It was found that there were **209** cluster members in M52 and **529** cluster members in NGC7789 using 1 x error tolerance, with **369** in M52 and **1033** in NGC7789 for a 2 x error tolerance. From comparison to literature values for the number of cluster members from different papers, the 2 x error tolerance gave far too many data points. The 1 x the error with the literature value radius value is within 8% of the literature value for M52 and 15% for NGC7789.

The slight discrepancy in the literature value of 193 cluster members from our data for M52 may be attributed to the fact that the study used a radius of 9' instead of our value of 13' and so it is reasonable to assume they would have a lower number of cluster members. Our value for cluster members of NGC 7789 is significantly lower than the literature. This is likely due to the limitations of our data only going down to a magnitude of approximately 17. Other groups have detected fainter objects than we were able to, hence our underestimate.

The proper motion method used has a high dependence on literature values for radius and average proper motion of the cluster. There were a wide range of estimates found for the radius of NGC7789 which meant that there was

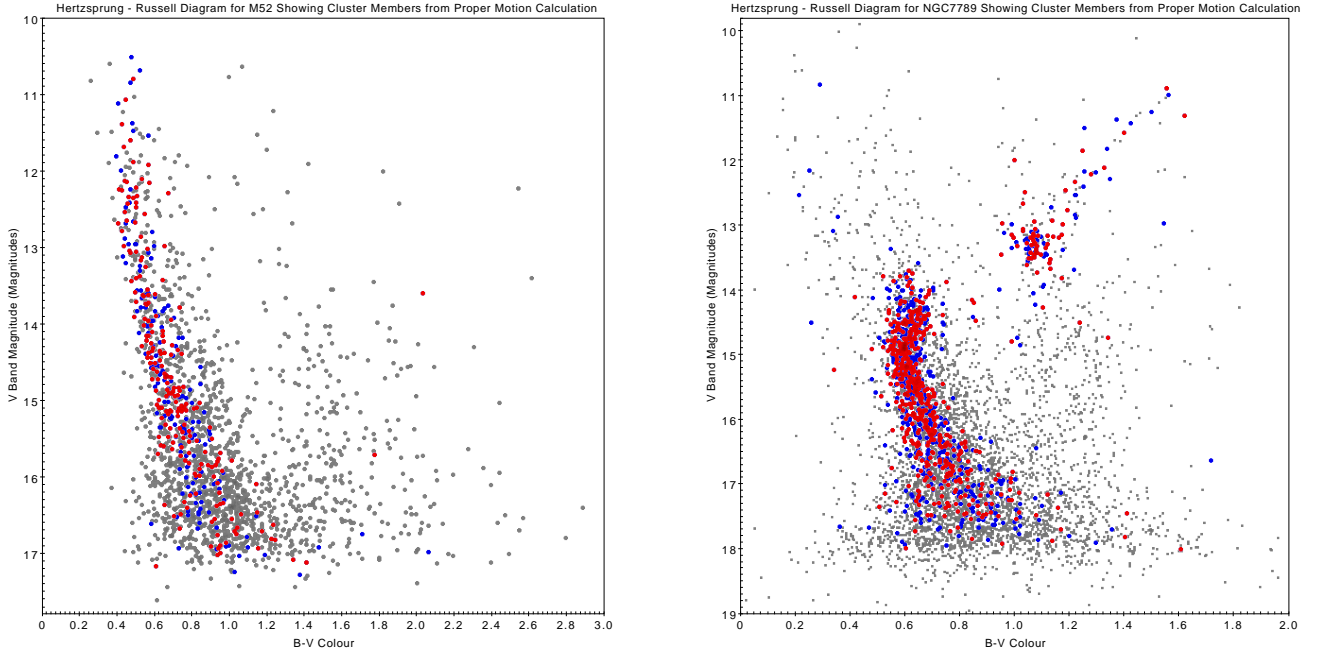


Figure 21: H-R diagrams with highlighted cluster members of M52 (left) and NGC7789 (right). Cluster members from a 1 error tolerance are shown in red and a 2 error tolerance in blue with background objects in grey.

less confidence on the membership value than for M52.

In Figure 20, the determined members for both clusters look to be sensible, with random distribution radially. It is clear from the NGC7789 plot that the radius is heavily limiting the number of cluster members as the density of cluster members is still relatively high at the radius cut of 16', suggesting that the cluster boundary has not yet been reached.

Looking at the H-R diagram (Figure 21) it is reassuring to see a tight main sequence, as would be expected of correct cluster members. The H-R diagram of NGC7789 also clearly shows the main sequence turn-off and the red giant branch.

4.5.2 Cluster Determination in aid of Extinction Coefficient - Visual Magnitude Cuts

The visual magnitude cut method was primarily designed to select the brightest main sequence objects in each cluster to improve the A_v calculation. It is clear when comparing to the proper motion cut method that visual cuts of the HR diagram are not robust for selecting cluster members. Despite this, plotting the cluster members does show a clear central density decreasing to a background level. The H-R diagrams also show that the red giant branch has been successfully excluded which was vital for the A_v calculation.

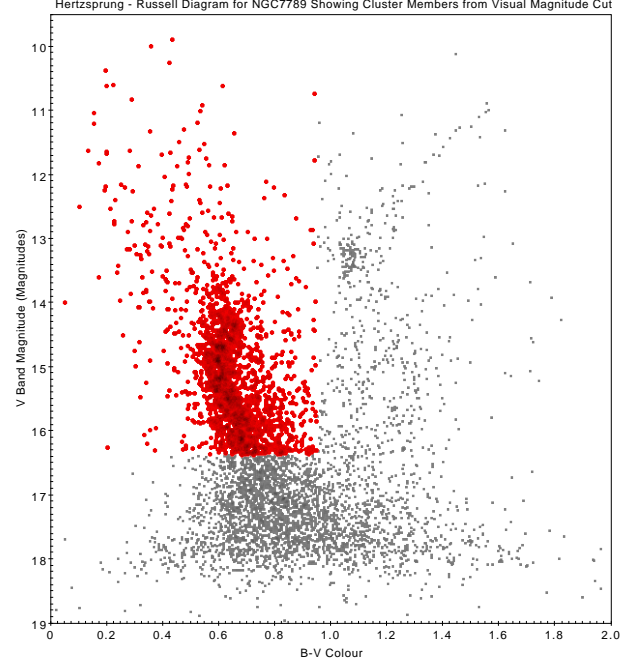
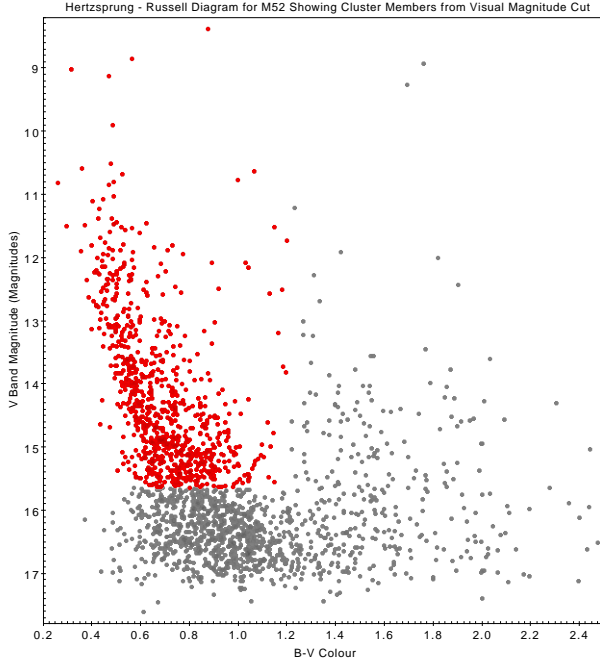


Figure 22: The HR diagrams of M52 (left) and NGC7789 (right). Cluster members determined from the visual magnitude cuts are shown in red with the background stars shown in grey.

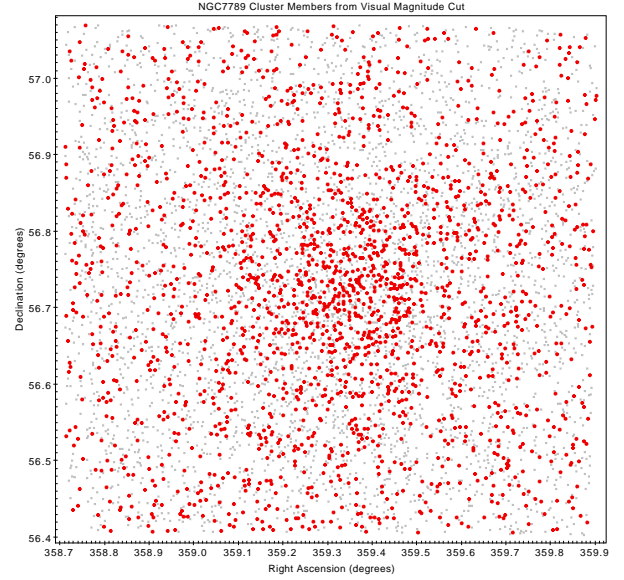
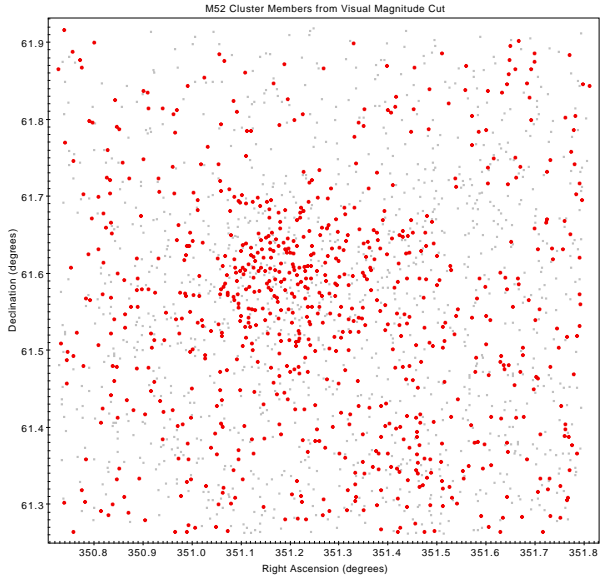


Figure 23: The cluster members of M52 (left) and NGC7789 (right) using a visual magnitude cut. Cluster members are in red and background stars are in grey.

4.6 Reddening

The reddening value, A_v was calculated using the data from cluster membership determination. Since there are two methods in determining the cluster membership, the A_v values from each methods will be compared and analysed further in this section.

4.6.1 Data from Cluster Membership Proper Motion: 1 x error tolerance

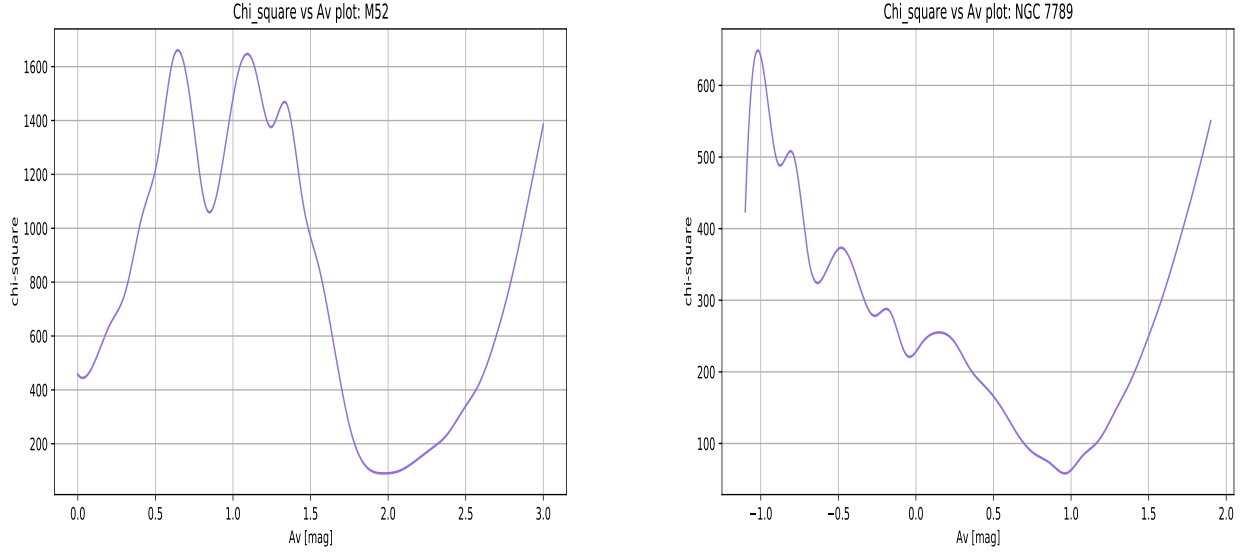


Figure 24: χ^2 graph of M52 (left) and NGC7789 (right). The minimum χ^2 shows the optimal A_v value required to deredden our data.

The χ^2 value for a range of A_v was calculated using equation 16 and the χ^2 graph plotted is seen in Figure 24. Based on Figure 24, the minimum χ^2 is when A_v values are ≈ 1.966 Magnitudes and ≈ 0.967 Magnitudes for M52 and NGC 7789 respectively. Error for the A_v values were calculated up to 3σ confidence interval.

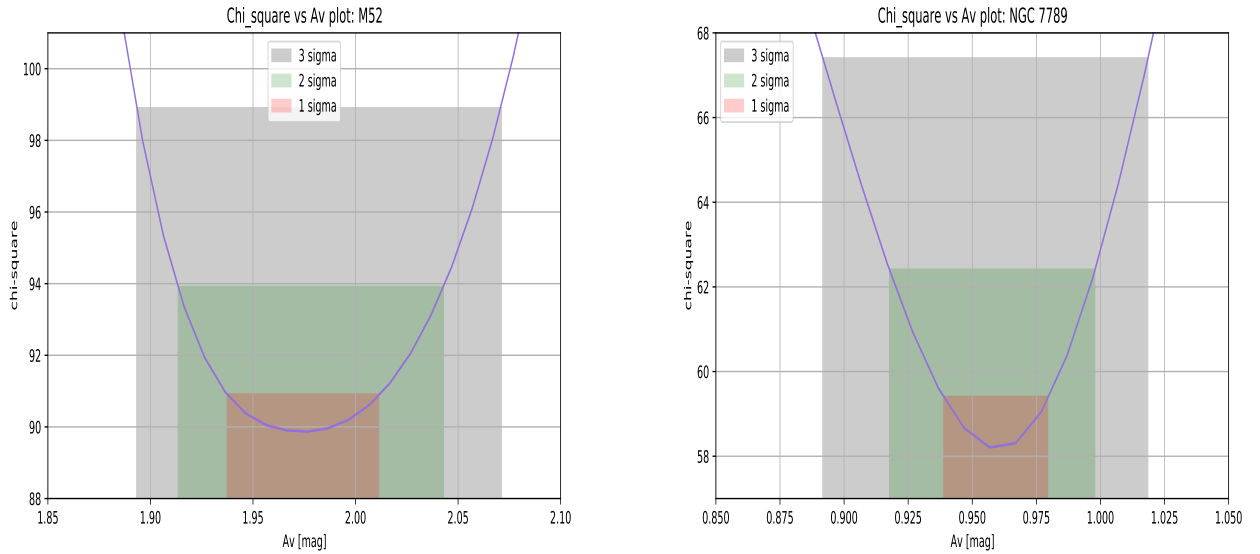


Figure 25: Zoomed in version of χ^2 plot in Figure 24. A_v values error determination for M52 (left) and NGC7789 (right). Red region is the 1σ confidence interval, green region is the 2σ confidence interval and grey region is the 3σ confidence interval for the optimal A_v values.

Confidence Interval	A_v Values [mag]	
	M52	NGC7789
1σ	1.97 (4)	0.97 (2)
2σ	1.97 (6)	0.97 (4)
3σ	1.97 (9)	0.97 (6)
Literature Value	2.015 ^[12]	0.8-0.9 ^[10]

Table 5: A_v values including error (cluster membership proper motion with 1 x error tolerance).

Based on Figure 25 and Table 5, 1σ confidence interval was determined by calculating the interval where $\Delta\chi^2 = 1$, which is the point below and above the best-fitting value of A_v . This is where the χ^2 increases by one from the minimum value. Similarly, 2σ and 3σ confidence interval were calculated when $\Delta\chi^2 = 4$ and 9 respectively. The σ confidence intervals are the statistical uncertainty of our calculated A_v values. This is expected to come from systematic errors while determining the cluster membership and photometry calculation.

Table 5 also shows that the literature value for M52 lies within 2σ confidence interval of the calculated A_v whereas for NGC 7789, our calculated A_v value is accurate to within 3σ confidence interval when compared with the literature value. A_v calculation for M52 is more accurate compared to NGC 7789. This is because NGC 7789 is an older cluster, hence most of the stars in this cluster had evolved from the main sequence resulting in less data to be analysed in the A_v calculation. We were using data from main sequence of both clusters to calculate the optimal A_v values as we were comparing it with the intrinsic main sequence from Fitzgerald et al^[70] (see Figure 26).

Since 2σ and 3σ confidence interval are just the statistical error, the uncertainty for the final A_v values was selected from 1σ confidence interval. Hence, the final A_v values calculated from cluster membership (1 x error tolerance) data was found to be 1.97(4) Magnitudes and 0.97(2) Magnitudes for M52 and NGC 7789 respectively. With these final A_v values of both clusters, our data was dereddened by producing a colour-colour diagram (UBV diagram):

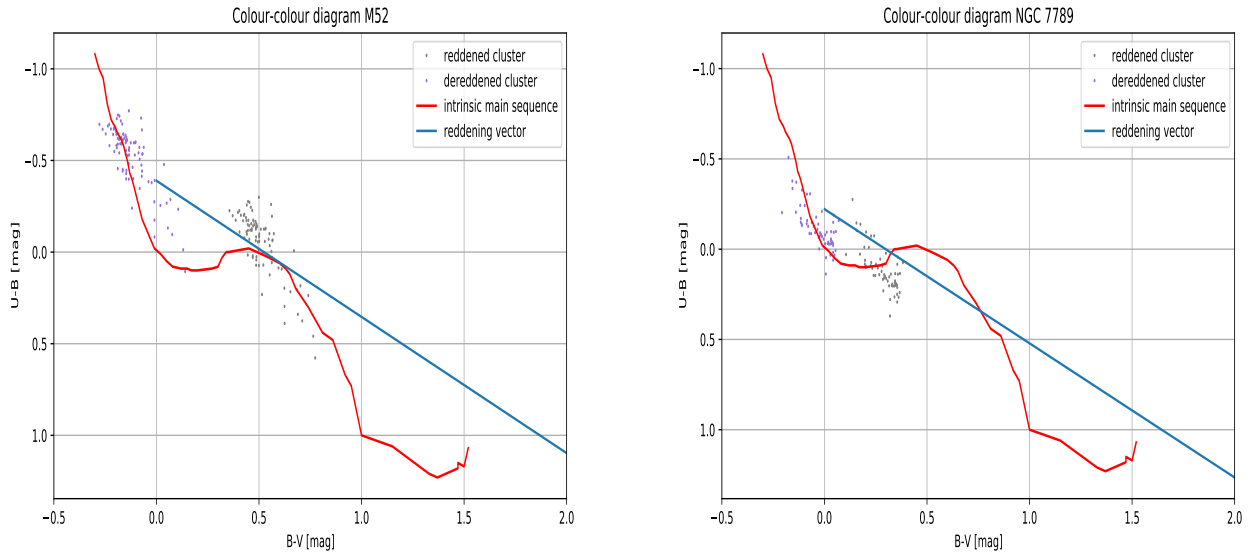


Figure 26: UB color-color diagram of M52 (left) and NGC7789 (right). Red line is the intrinsic main sequence taken from Fitzgerald et al^[70]. The blue line is the reddening vector that have a slope of 0.74324.

In the UB color-color diagram, the main sequence of M52 and NGC7789 was translated across the reddening vector, in

increment of the calculated A_v values. The reddened data is shown in grey, and the corrected, dereddened data is shown in purple. We can see that the dereddened data does sit on top of the intrinsic main sequence. This is because the optimal values of A_v was chosen where χ^2 was at its minimum: that is, at which point the positions of the cluster data was closest to the intrinsic main sequence.

4.6.2 Data from Cluster Membership Proper Motion Matched with the Older Catalogue

By using a new set of data from cluster membership proper motion (1 x error tolerance) that was matched with the older catalogue, the same χ^2 graph, its error and the UBV diagram as in Figure 24, 25 and 26 was plotted (see Appendix B). The results obtained from this data are shown as follows:

Confidence Interval	A_v Values [mag]	
	M52	NGC7789
1 σ	1.896 (5)	1.18 (2)
2 σ	1.90 (2)	1.18 (7)
3 σ	1.90 (4)	1.2 (1)
Literature Value	2.015 ^[12]	0.8 - 0.9 ^[10]

Table 6: A_v values including error (cluster membership proper motion matched with the older catalogue).

From table 6, the final A_v values was chosen to be the one with 1 σ confidence interval which is 1.896 (5) Magnitudes and 1.18 (2) Magnitudes for M52 and NGC7789 respectively. The literature values for both clusters did not lie anywhere in between 1 σ and 3 σ confidence intervals. This is assuming the statistical uncertainties in the calculation of σ confidence intervals are huge, due to the high systematic error when matching the older catalogue with cluster membership proper motion data.

4.6.3 Final Reddening Value

The table below summarises the final A_v values calculated from this section:

Method	A_v Values [mag]	
	M52	NGC7789
Cluster Membership	1.97 (4)	0.97 (2)
Cluster Membership Matched with the Older Catalogue	1.896 (5)	1.18 (2)

Table 7: Final A_v values.

4.7 Distance Determination

This section will present the distance to M52 and NGC 7789 using the A_v values calculated from two different cluster membership data as in Section 4.6.

4.7.1 Data from Cluster Membership Proper Motion: 1 x error tolerance

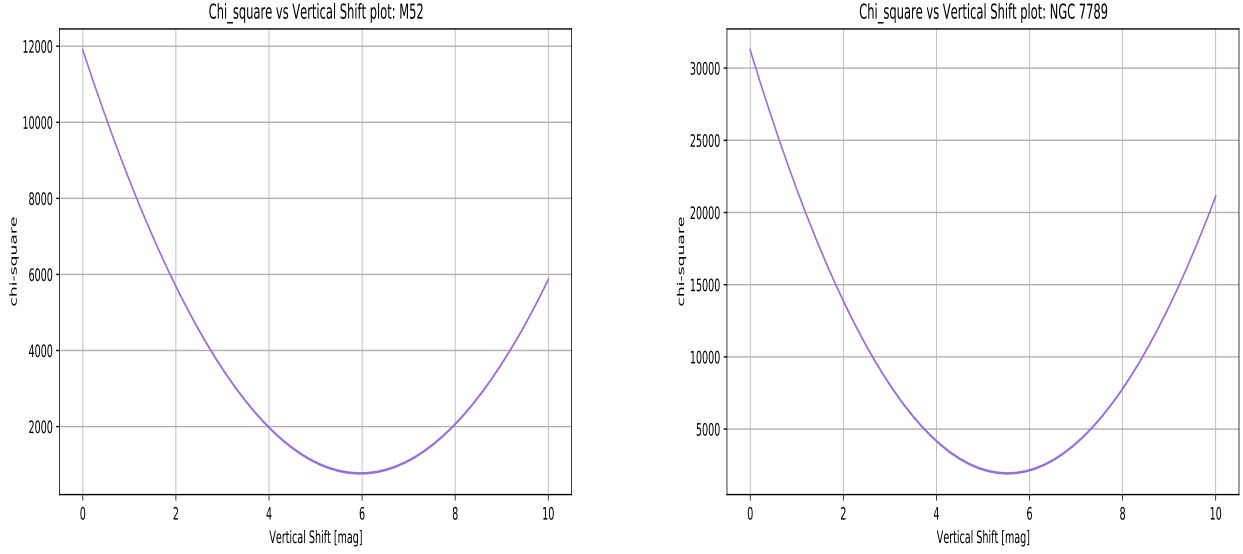


Figure 27: χ^2 graph of M52 (left) and NGC 7789 (right). The minimum χ^2 value shows the optimal vertical shift required for the two main sequences in the BV diagram to sit on top of each other.

Figure 27 shows that a minimum χ^2 was obtained when the vertical shifts are ≈ 5.92 Magnitudes and ≈ 5.51 Magnitudes for M52 and NGC 7789 respectively. Distances to the clusters were then determined using equation 18 by substituting the vertical shift for the *distance modulus* value on the left hand-side of the equation. Error for the vertical shift values as well as the distance were calculated up to 3σ confidence intervals as follows:

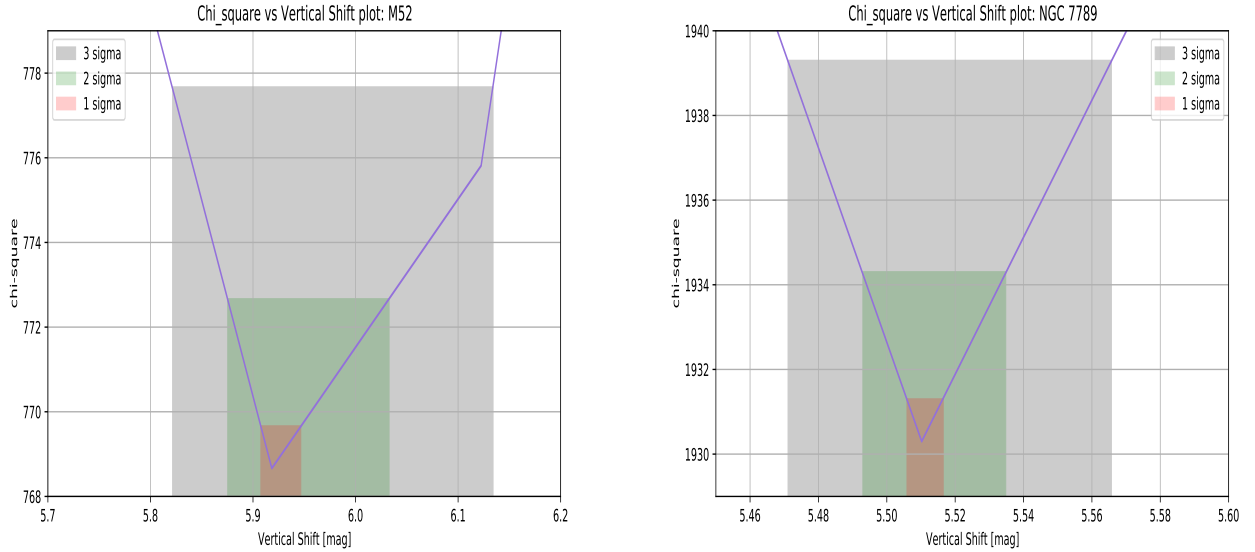


Figure 28: Zoomed in version of χ^2 plot in Figure 27. Vertical shift error determination for M52 (left) and NGC7789 (right). Red region is the 1σ confidence interval, green region is the 2σ confidence interval and grey region is the 3σ confidence interval for the optimal vertical shift values.

Confidence Interval	Vertical Shift Values [mag]		Distance [pc]	
	M52	NGC7789	M52	NGC7789
1 σ	5.92 (2)	5.510 (5)	2070 (19)	1718 (4)
2 σ	5.92 (8)	5.51 (2)	2070 (80)	1718 (16)
3 σ	5.9 (2)	5.51 (5)	2100 (200)	1720 (40)
Literature Value: GAIA Parallax Measurement ^[15]	-	-	1677.85	2207.51

Table 8: Vertical shifts and their respective distance including error (cluster membership proper motion with 1 x error tolerance).

From Table 8, the final value for the distance was chosen to be the one within a 1σ confidence interval which is 2070 (19) pc and 1718 (4) pc for M52 and NGC7789 respectively. It was also deduced that the literature values for both distance did not lie anywhere within $1\sigma - 3\sigma$ confidence interval. Besides high statistical error coming from systematics uncertainty while calculating the σ confidence interval, distance to the clusters is complicated to be determined due to high interstellar absorption that light suffered on its way toward us.

The dereddened cluster data that was shifted following the calculated vertical shift value is shown in the BV diagram:

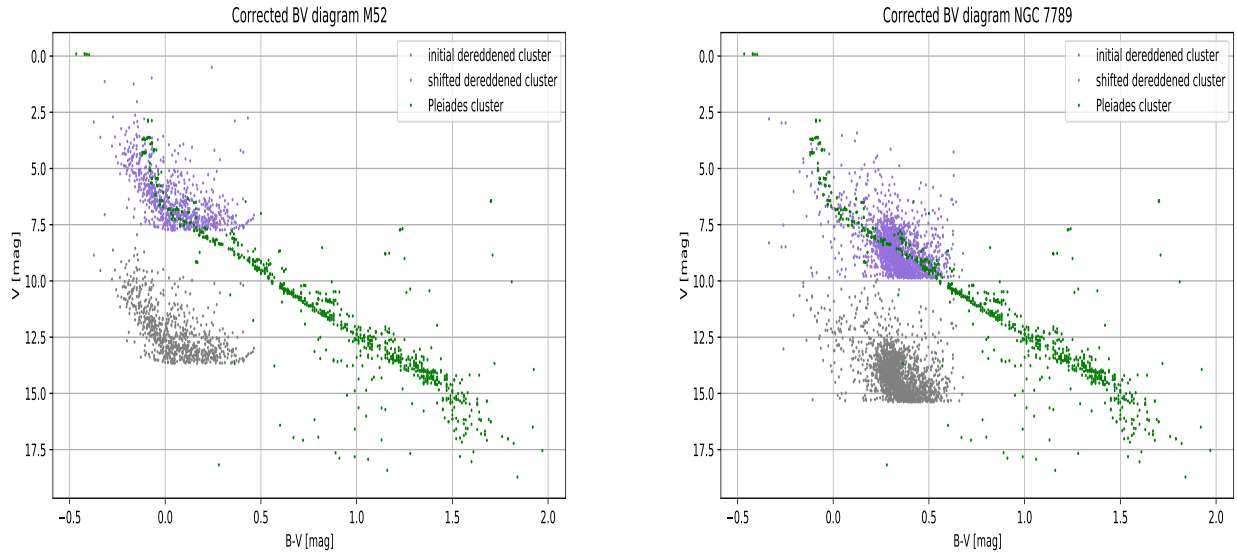


Figure 29: BV diagram for M52 (right) and NGC7789 (left). Green data points are the main sequence of Pleiades cluster (M45), the original dereddened cluster (grey) and the shifted dereddened cluster (purple). M45 cluster has a very low reddening with well-known distance from the GAIA parallax measurement to be 135.8 pc.

It can be seen that the shifted dereddened cluster following the calculated vertical shift value does sit on top of the M45 main sequence. This is because the optimal value of vertical shift was chosen when its χ^2 value was at its minimum, which indicates the minimum vertical distance between our clusters main sequence and the M45 main sequence.

4.7.2 Data from Cluster Membership Proper Motion Matched with the Older Catalogue

By matching the cluster membership proper motion data (1 x error tolerance) with the older catalogue, a different A_v values were calculated for M52 and NGC7789. Hence, by using cluster data that was dereddened using a new optimal A_v value, the χ^2 graph, its σ error determination and the BV diagram as in Figures 27, 28 and 29 were plotted for this section and can be seen in appendix B. Results obtained from the new dereddened data is shown in the following table:

Confidence Interval	Vertical Shift Values [mag]		Distance [pc]	
	M52	NGC7789	M52	NGC7789
1 σ	5.6 (1)	6.21 (4)	1810 (80)	2370 (40)
2 σ	5.6 (2)	6.21 (16)	1810 (170)	2370 (170)
3 σ	5.6 (3)	6.2 (2)	1800 (300)	2400 (200)
Literature Value: GAIA Parallax Measurement ^[15]	-	-	1677.85	2207.51

Table 9: Vertical shifts and their respective distance including error (cluster membership proper motion matched with the older catalogue).

The final value of the calculated distance for this section was chosen to be the one with 1 σ confidence interval which is 1810 (80) pc and 2370 (40) pc for M52 and NGC7789 respectively. The literature value of the distance from GAIA parallax measurement lies within 2 σ error from the calculated distance in Table 9 for both clusters. This shows that distance calculation in this section is more accurate compared to the one calculated in Section 4.7.1.

4.7.3 Final Distance and Reddening Value

Method	Distance [pc]		Percentage Error [%]	
	M52	NGC7789	M52	NGC7789
Cluster Membership	2070 (19)	1718 (4)	23.4	22.2
Cluster Membership Matched with the Older Catalogue	1810 (80)	2370 (40)	7.9	7.4
Literature Value: GAIA Parallax Measurement ^[15]	1677.85	2207.51	-	-

Table 10: Comparison of calculated distance using two different dereddened data for M52 and NGC7789, with their respective percentage error.

When comparing the results of the calculated distance from two dereddened cluster data sets, it was found that the distance to both clusters is more accurate when the data from cluster membership proper motion (1 x error tolerance) matched with the older catalogue was used. For M52, this data gives percentage error of 7.9% from the literature value which is lower than the percentage error from the original cluster membership proper motion, that was calculated to be 23.4% from the literature value. Same goes for the percentage error of NGC7789 as presented in Table 10. Hence, the calculated distance and A_v values from the cluster membership matched with the older catalogue data was chosen as the final results and it is summarised as follows:

Method	Distance [pc]		A_v value [mag]	
	M52	NGC7789	M52	NGC7789
Cluster Membership Matched with the Older Catalogue	1810 (80)	2370 (40)	1.896 (5)	1.18 (2)
Literature Value	1677.85 ^[15]	2207.51 ^[15]	2.015 ^[12]	0.8-0.9 ^[10]

Table 11: Final results for the calculated distance and A_v values for M52 and NGC7789.

4.8 Cluster Centre Estimation

Method	Centre (RA, Dec) / degrees			
	M52		NGC7789	
Mean (equation)	351.20 (2)	61.59 (5)	359.32 (2)	56.75 (5)
Mean (histogram)	351.197 (12)	61.591 (5)	359.316 (8)	56.748 (4)
Kernel Density	351.17 (2)	61.59 (5)	359.33 (2)	56.72 (5)
Literature Value	351.20 ^[50]	61.59 ^[50]	359.35 ^[51]	56.70 ^[51]

Table 12: Determined cluster centres.

4.8.1 Cluster Centre Estimation by Mean

The cluster centre calculated from each of our methods were consistent with each other and the literature values, suggesting that the value obtained was accurate. Our surface density (Figures 34 and 35) also showed the expected shape, with the maximum in the first annulus which suggests a correct estimate of the cluster centre. The histogram plots of the RA, Dec are shown in Figures 30 and 31.

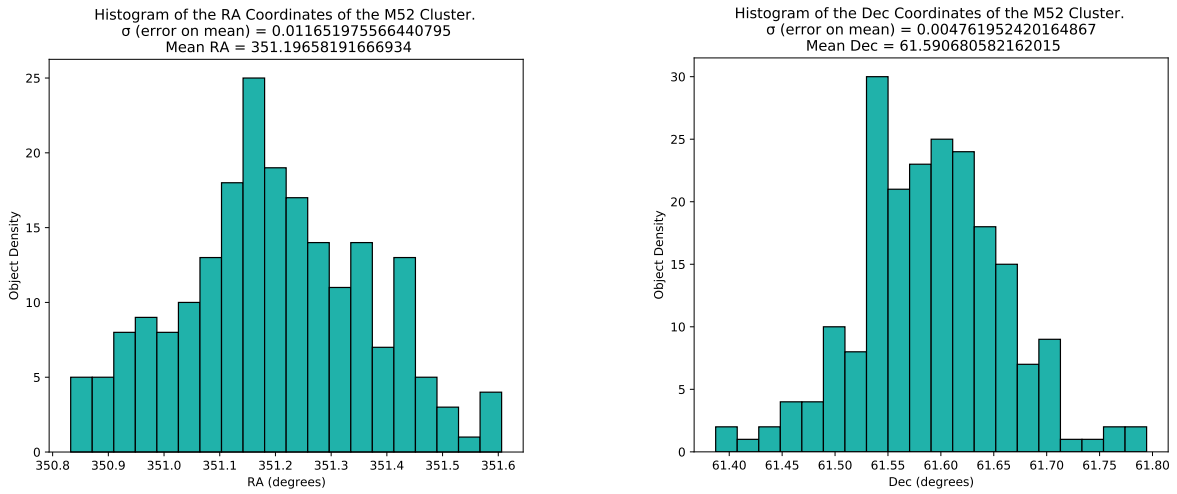


Figure 30: The histograms of the RA, Dec for M52 cluster with the error in the mean shown in the title.

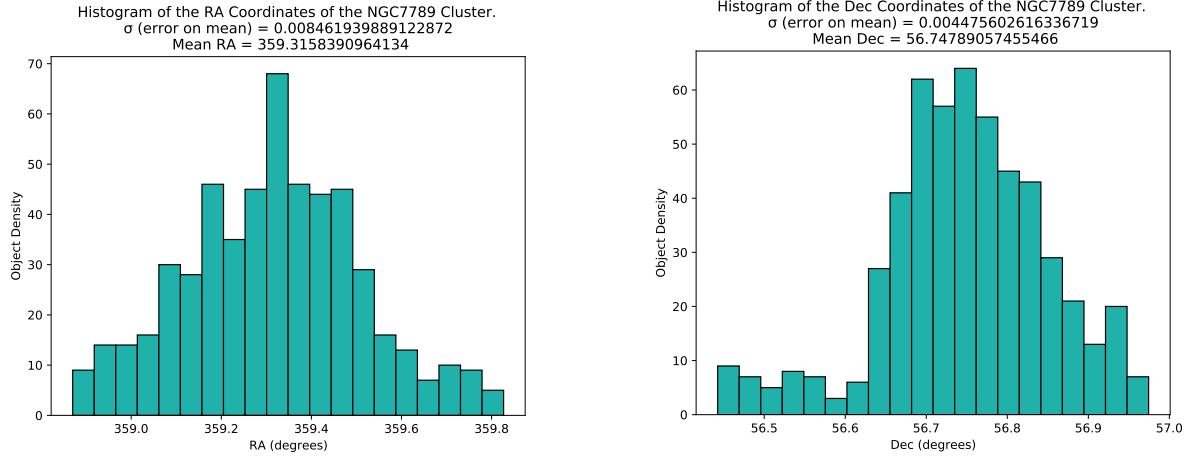


Figure 31: The histograms of the RA, Dec for NGC7789 cluster with the error in the mean shown in the title.

4.8.2 Cluster Centre and Average Proper Motion Estimate by Kernel Density Estimation

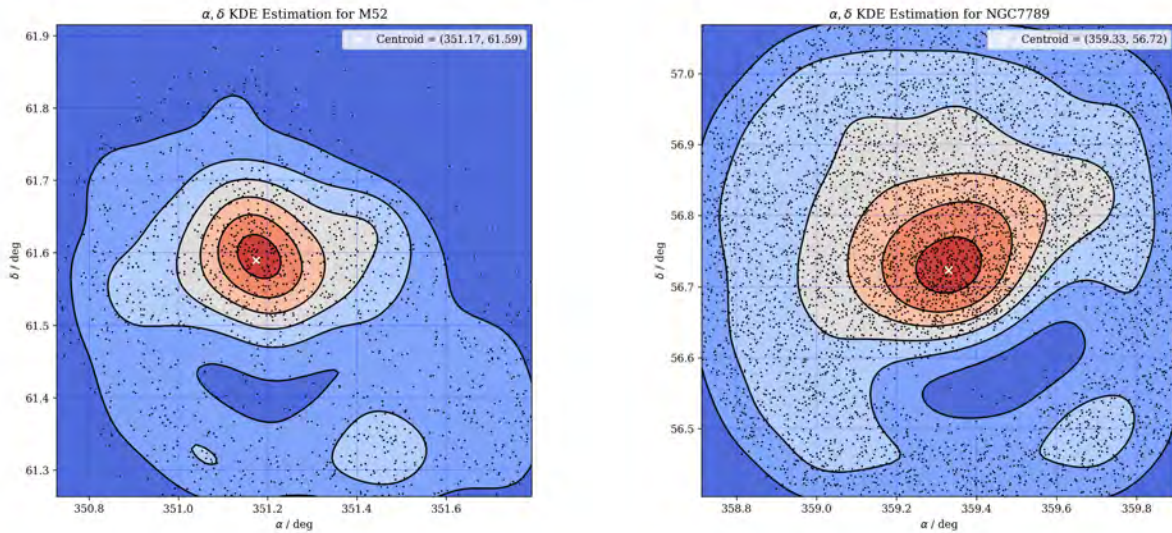


Figure 32: The KDE plot for the RA, Dec of M52 (Left) and NGC 7789 (Right). Determined centre of cluster shown in the top right of the plots.

The kernel density estimation plots are shown below in Figures 32 and 33. From these estimations it was determined that the cluster center for M52 was, (351.17, 61.59) degrees and for NGC 7789, (359.33, 56.72). The proper motion values found were found to be for M52, (-1.95, -1.14) and for NGC7789, (-0.96, -1.95). For the proper motion, the values obtained from the KDE plots closely match the literature values.

In the plot of the RA, Dec of NGC 7789 shown in Figure 32, there is a area of the plot that is severely lacking in stars in the right of the diagram (below 56.75 degrees). This does not appear in the plots of the cluster members shown in Figure 20. Due to the lack of hole in the cluster member plots that were made, it is hypothesised that there is dust obscuring the image. The dust is behind the star cluster implicating observation of distant field stars.

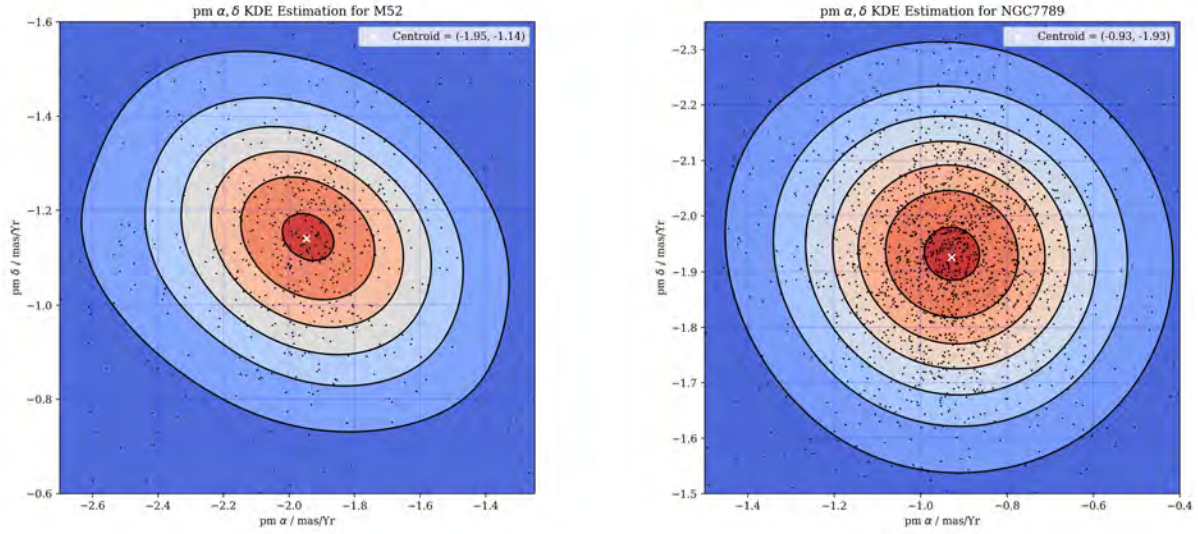


Figure 33: The KDE plot for the proper motion of M52 (Left) and NGC 7789 (Right).

	Average Proper Motion at Centroid (RA, Dec) / mas/yr	
Method	M52	NGC7789
Kernel Density Plots	-1.95 (11), -1.14 (11)	-0.96 (10), -1.95 (10)
Literature Value	-1.938 (147) ^[14] , -1.131 (154) ^[14]	-0.922 (140) ^[14] , -1.933 (13) ^[14]

Table 13: Determined average proper motion for the centroid of the clusters.

4.9 Radius Estimation via Surface Density Plots

	Radius / degrees		Core Radius / degrees	
Method	M52	NGC 7789	M52	NGC 7789
Surface Density Plots	0.21(4)	0.20(5)	0.06 (2)	0.08 (3)
Literature Value	0.15 ^[69] - 0.22 ^[19]	0.13 ^[21] - 0.26 ^[12]	0.06 ^[13]	0.12 ^[17]

Table 14: Determined cluster radii.

From the Figure 34 and 35, the radius of the clusters were determined and displayed on Table 14. The M52 radius is consistent with the literature range. For NGC 7789, the result is consistent with the literature however there was a very large range of values found from the literature which does reduces the confidence of the result. Looking visually at the plots the values calculated seem sensible and look to represent the point of intersection. Taking the average value of many intersections also helped to make the value more robust and using an exponential fit also improved the value as the intersection was not affected by the noise of the plot. When using our radii for cluster membership determination above, the number of members found was consistent with literature values, also suggesting our calculated values for cluster radius are sensible.

The core radius was also calculated using these plots. For M52, the core radius value exactly agrees with the literature value. For NGC 7789, the determined core radius is 0.04 degrees off the literature value, with the error taken into consideration, this is only 0.01 degrees off the literature value, and therefore is deemed to be an

acceptable result.

The exponential fit looked to be consistent with the data, with the residuals randomly scattered about 0, however the large amount of noise in the data means that only around 50% of the residuals cross the x-axis. This could likely be improved by reducing the number of annuli used for the surface density calculation, however this would be a trade-off with the accuracy of the radius estimation as the resolution of the intersection point would be larger. For this reason, the annuli number was not changed to reduce the noise for exponential fitting.

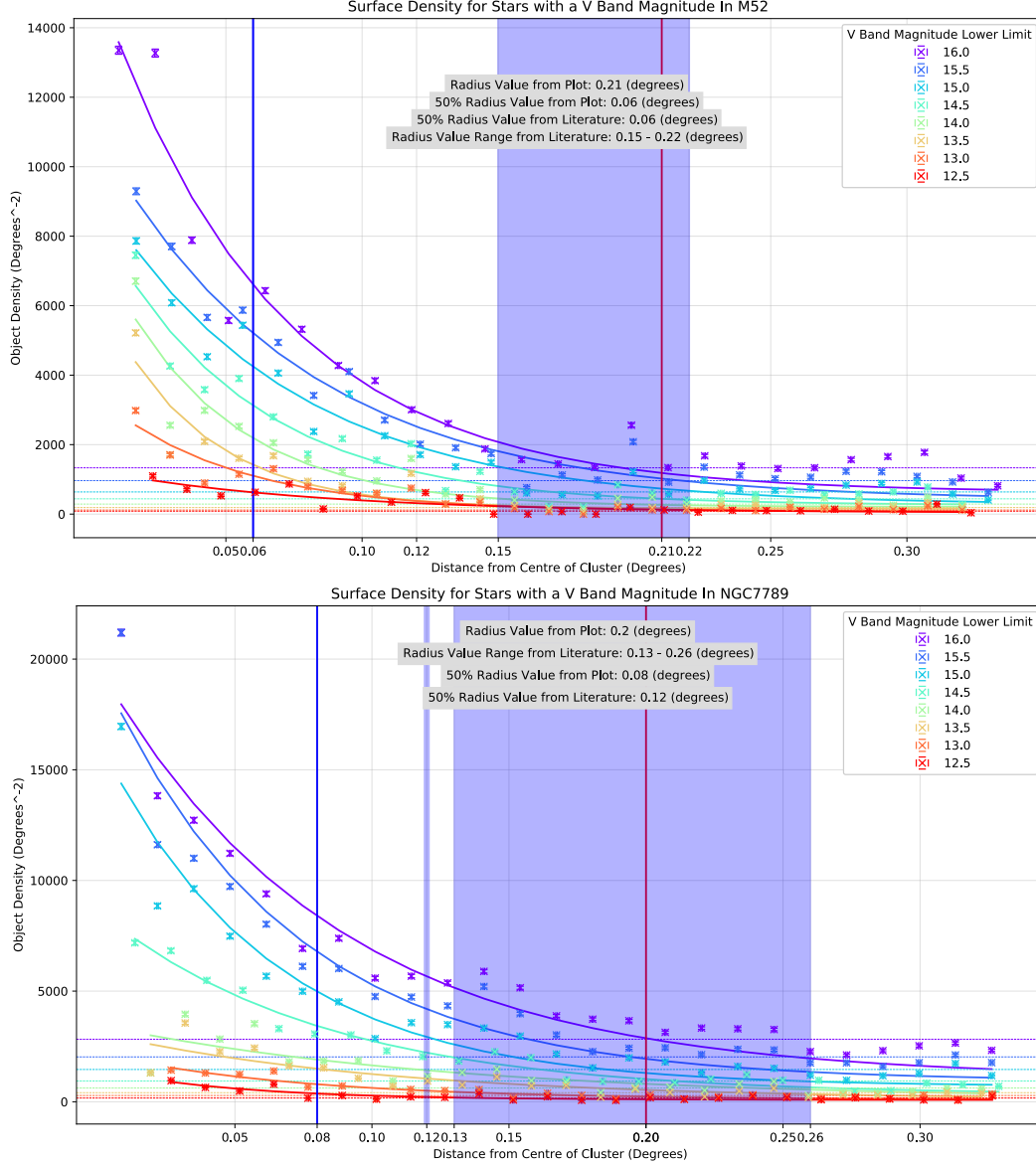


Figure 34: Surface density plots with an exponential fit for the V band for M52 (top) and NGC 7789 (bottom) across a range of magnitude cuts. The determined radius is shown as the red line and the literature range as the purple box. The determined core radius shown as the blue line with the literature value as a small purple line (unseen in M52 plot because the literature value exactly equals the determined value).

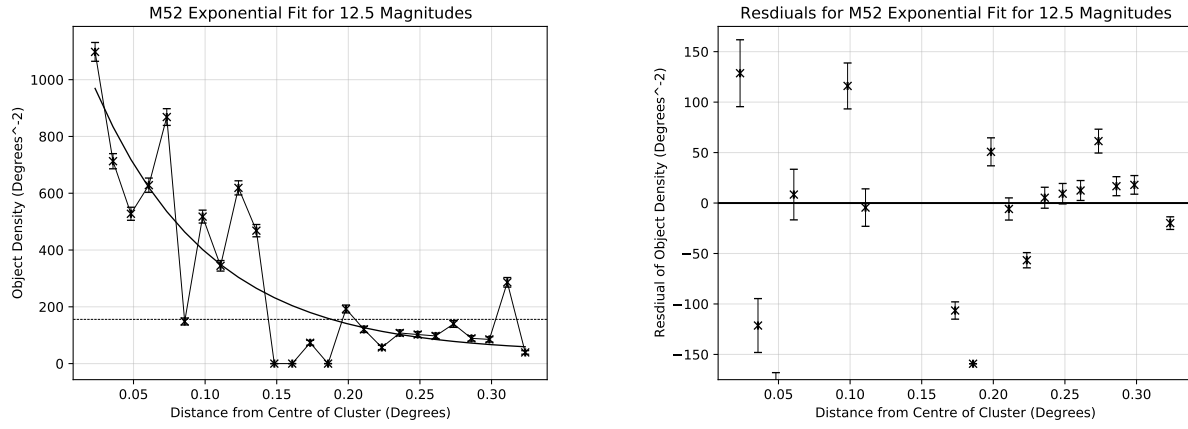


Figure 35: An example of the exponential fit with residual plot for the 12.5 magnitude M52 surface density.

4.10 Isochrone Fitting

4.10.1 Preliminary Fits using MIST: UBVR(I) & Temperature-Luminosity

Initial attempts at fitting isochrones made use of the `isochrones`^[71] package, which used *MIST*^[57] stellar grids. These attempts were made in the parameter spaces of both $\log T, \log L$ (log-log) and $(B - V), M_V$ (CMD), using theoretical stellar grids for the former and synthetic CMD stellar grids constructed from real data for the latter. Log-log data for our clusters was mapped from CMD data using the Rochester Modern Mean Dwarf catalogue.^[59] Best-fit isochrones are illustrated in appendix L, with results in table 15.

These results were obtained in the process of building the isochrone fitting code to examine whether our method would prove feasible. Fitting in log-log parameter space was initially examined as `isochrones` readily allowed download and interpolation of MIST theoretical isochrones, giving rapid retrieval of reference isochrones for fitting.

Age estimates for M52 proved only barely acceptable, lying toward the upper limit of previous estimates circa 160 My^[72], with metallicity close to literature values $[Fe/H] \approx 0$ ^[13]. For NGC 7789 the age estimate was suspect, lying beyond the cusp of the lower bound of previous uncontested modern estimates about 1.3 Gy^{[73],[74]}, whilst the metallicity estimate lied within the wide range of literature values of $0.1 \leq [Fe/H] \leq -0.35$.^{1998PASP..110.1318G, [73]} Some estimates for the age of NGC 7789 go as low as 1.1 Gy^{[75],[73]} though these estimates are heartily contested in later reviews.^[67]

Both age determinations residing about the bounds of literature values in log-log space casted doubt on our mapping, motivating the use of MIST UBVR(I) synthetic CMD's for isochrone fitting. `isochrones` does not readily interpolate MIST synthetic CMD isochrones and consequently the time steps available for fitting, $\Delta \log t$, were limited to that of the synthetic CMD's, in steps of 0.1 dex. MIST UBVR(I) stellar grids store magnitudes in a menagerie of passbands, however not for the Johnson-Cousins U,B,V passbands: we used the Tycho B,V passbands, which had to be converted to the Johnson-Cousins system^{[76],[77]}. This introduced a possible source of error in isochrone fitting, as any inconsistency in magnitude conversion would result in isochrones being positioned incorrectly in our CMD's.

Fitting using MIST UBVR(I) isochrones in CMD parameter space proved consistently reliable for age estimates, with age determinations for both M52 and NGC 7789 lying squarely within the range of previous literature estimates. Best-fit metallicity remained unchanged. To avoid the concerns associated with mapping CMD parameter

space to log-log parameter space that made themselves evident with these preliminary fittings, the decision to fit isochrones in CMD parameter space was taken.

Cluster	Parameter Space	[Fe/H]	Age
M52	$(B - V), M_V$	0.00	60 My
	$\log T, \log L$	0.00	138 My
NGC7789	$(B - V), M_V$	-0.10	1.35 Gy
	$\log T, \log L$	-0.10	1.26 Gy

Table 15: Preliminary best-estimates obtained using MIST isochrones by way of weighted least-squares fitting, in $\log T, \log L$ (log-log) & $(B - V), M_V$ (CMD) parameter spaces. These were obtained using earlier reduced data, prior to improvements in the reduction code which gave more members, better estimates for optical depth, and improved cluster photometry, and error estimation was not carried out.

4.10.2 Final Fits using PARSEC/COLIBRI CMD Isochrones

In deciding to fit in CMD parameter space, a key limitation of the MIST UBVR(I) synthetic CMD isochrones was discovered: the available time-step of $\Delta \log t \approx 0.1$ dex is rather large. The RGB for NGC 7789 was fairly offset from all trialled isochrones that accurately fit the MS turnoff, requiring far older ages, which was concerning. It was decided to use an alternative set of isochrones: the PARSEC/COLIBRI^[56] isochrones. These were downloaded in steps of $\Delta \log t = 0.001$ dex for $6 \leq \log t \leq 10.4$, for $-0.30 \leq [Fe/H] \leq 0.30$ in steps of 0.05 dex, with a linear interpolator written to provide isochrones to the fitting routine.

Final isochrone fits are shown in appendix K. These made use of PARSEC/COLIBRI isochrones. See Figure 36 for visualization of our errors and confidence intervals against χ^2 . See Table 18 for final estimates on age and error, to 3σ confidence. The metallicities which provided the cleanest and lowest $\chi^2(t)$ curves are 0.05, -0.30 dex for M52, NGC 7789 respectively, and form our estimate for cluster metallicities.

In χ^2 minimization one expects a minimized value of $\chi^2 \approx N$.^[61] This was somewhat observed in the scaling of χ^2 between data-sets, but not observed in a perfect fashion numerically.

The least-squares statistic $R^2(t)$ was equivalent to χ^2 by assumption, with the difference being that each datapoint was weighted by some w_i : the w_i were arbitrarily chosen, all satisfying $w_i \leq 1$. Per this weighting regime, it was expected the observed minimum χ^2 to be less than N for each cluster. This was observed.

From the reduction, $N_{M52}, N_{NGC7789} \approx 200,500$ and $\chi^2_{M52}, \chi^2_{NGC7789} \approx 370,850$. The N were roughly twice as large as the χ^2 . This result was better than expected, possibly implying the assumption of $\chi^2 \approx R^2$ was somewhat reasonable. These were all purely approximate values for the sake of introspection.

Sigma	CI [$\log t$] / dex	$\Delta \log t$ / dex
1σ	[7.980, 8.056]	0.038
2σ	[7.942, 8.096]	0.077
3σ	[7.837, 8.154]	0.159

Table 16: Confidence intervals & errors determined during final age estimation for M52. [Fe/H] estimate as 0.05.

Sigma	CI $[\log t] / \text{dex}$	$\Delta \log t / \text{dex}$
1σ	[9.153,9.162]	0.005
2σ	[9.147,9.166]	0.010
3σ	[9.141,9.170]	0.015

Table 17: Confidence intervals & errors determined during final age estimation for NGC 7789. $[\text{Fe}/\text{H}]$ estimate as -0.30.

Previous age estimates for M52 (NGC 7654) lie between a rough lower limit of 25 My^[78] and a rough upper limit of 160 My^[72], with any number of attempts to constrain age typically lying within this range.^{[13],[79]} There is an inherent difficulty in age determination for young OC's such as M52 due to the steep turnoff, which does not vary significantly for a wide range of age estimates, as can be seen in the final isochrone fits for M52 and the rather wide 3σ confidence interval for age determination. The 3σ confidence interval lies entirely within this range, indicating reasonable accuracy in our age determination attempt, though the error estimates are notably larger than those of previous studies.^[13]

Cluster	$\log t / \text{dex}$	$\text{CI}_{3\sigma} / \text{dex}$	t	$\text{CI}_{3\sigma}$
M52	8.023(159)	[7.837,8.154]	105(37) My	[69, 143] My
NGC 7789	9.157(15)	[9.141,9.170]	1.44(5) Gy	[1.38, 1.48] Gy

Table 18: Obtained age determination and associated 3σ confidence intervals final determinations for M52 & NGC7789, in both exponent and non-exponent forms. $[\text{Fe}/\text{H}]$ used were 0.05 & -0.30 respectively, our best estimates for metallicity of these clusters.

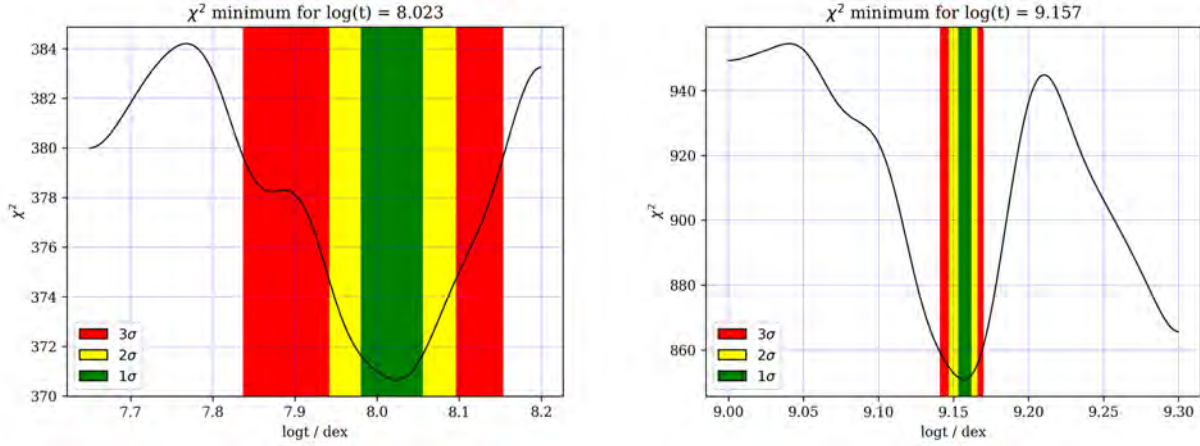


Figure 36: Error estimation in final age determinations for M52 (left) & NGC7789 (right), 1,2,3 σ confidence intervals illustrated.

This error can be attributed to the rough method by which it was calculated, which did not follow the full statistical rigour that is typical in estimating error for weighted least-squares fitting.

An improved method for error estimation may be by estimation of the sensitivity of our age estimate to error in the data. By introducing error randomly in the CMD data and measuring the average change in age estimate from some average geometric error in the CMD,

$$\Delta\epsilon = \sqrt{(\Delta(B - V))^2 + (\Delta M_V)^2}$$

it may be possible to estimate $\Delta \log t$ for some estimate at $\Delta\epsilon$ based on our distribution of errors in $B - V$ and M_V , by first estimating the sensitivity of $\Delta \log t$ to $\Delta\epsilon$:

$$\frac{\partial \log t}{\epsilon} \approx \frac{\Delta \log t}{\Delta\epsilon} \therefore \Delta \log t \approx \Delta\epsilon \frac{\partial \log t}{\epsilon}$$

In the case of NGC 7789, previous age estimates generally give a range of 1.3 to 1.6 Gy.^{[73],[74]} The entirety of our 3σ confidence interval for age determination of NGC 7789 indeed lies within this range, indicating reasonable age estimation.

Age estimates may theoretically lie beyond 1.6 Gy if the peculiar red giant branch (RGB) morphology of NGC 7789 is to be fitted accurately^{[67],[80]} with one such estimate lying close to 2 Gy.^[81]

It was impossible to investigate this due to an abnormality in the CMD offset between the RGB and MS turnoff. The magnitude of the relative offset between the RGB and MS turnoff appeared to be 0.5, 0.8 for the relevant paper^[67] while for the data it manifests as 0.5, 1.0 therefore no explanation was found for this, as the turnoff and MS appear identical to that of the previous study.

4.11 IMF Fitting

Obtained mass estimates are displayed in table 19. See Figure 37 for the resultant PDMF's of the clusters and their Salpeter fits.

In the case of NGC 7789 a literature value for M_C is given by $6620(763) M_\odot$.^[82] The estimate for integrated cluster mass lies outside this range, lying within 2σ of the literature value. Observed stellar mass for NGC 7789 was lower than the literature value for cluster mass by a factor of ≈ 5.5 . This demonstrated that the observed membership must only be a small fraction of the entire cluster, that of only the brightest stars present. This matches expectation that most of a stellar population's mass will be concentrated in its lighter stars.

Integrated cluster mass for M52 was larger than the literature value of $\approx 1,200 M_\odot$ ^[79] by approximately 60%, with our observed mass being $\approx 50\%$ of the total literature mass. These large percentage differences are concerning and potentially illustrate error with the calculations. The observed stellar mass is significantly lower than the integrated cluster mass and indeed the literature value, matching expectations.

Cluster	M_C	M_{Obs}
M52	$1920 M_\odot$	$610 M_\odot$
NGC7789	$5670 M_\odot$	$1210 M_\odot$

Table 19: Estimate for cluster mass M_C for M52 & NGC 7789 based on integration of the Salpeter IMF down to $0.50 M_\odot$, including an estimate for the observed masses of the clusters.

Overall Salpeter IMF's proved to be a good fit against the observed PDMF's for the clusters, serving as supporting evidence to the presence of a universal IMF.^[65]

The PDMF for M52 harbours, fractionally compared to the peak of the PDMF, more stars at higher masses than that of NGC 7789's PDMF. This matches expectation: M52 is younger and thus more massive stars from initial

cluster formation will still be present in the cluster and thus contribute to the PDMF, while NGC 7789 is far older and thus only more recently formed massive stars will contribute to the PDMF, of which there are generally fewer as the star formation rate for massive stars decays rapidly with age for a star cluster when compared to that of less massive stars.^{[83],[63]}

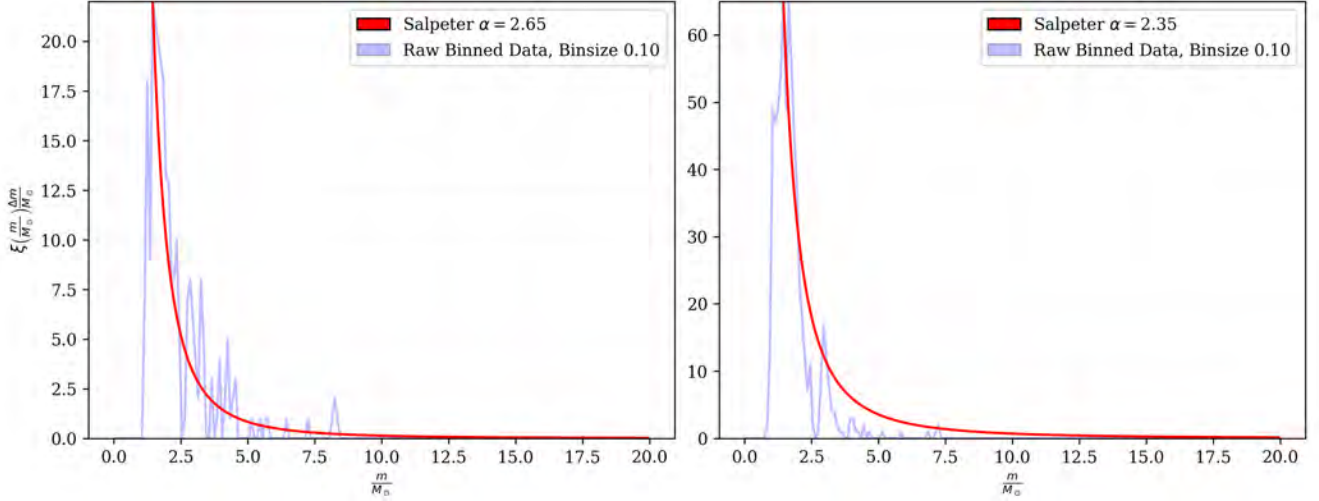


Figure 37: Observed Present-day Mass Function (PDMF) plots for M52 (left) and NGC7789 (right). The Salpeter IMF^[64] has been fitted and over-plotted for each cluster.

4.12 [FSR 2007] 0433: Serendipitous cluster discovery in M52 Image Field

Toward the periphery of our images of M52 we discovered an extra open cluster with an extremely small membership which showed up as a local peak in KDE estimation for M52. It was determined through visual comparison to other local clusters^[15] about the determined cluster centroid that this cluster was [FSR 2007] 0433.^[84]

4.12.1 Reddening & Distance

The determined parameters for interstellar reddening and distance are displayed in Table 20. Using *GAIA DR2* distances to our cluster membership gave a mean distance estimate of 2840(46) pc, where error is estimated as the standard deviation. This agrees with our distance determination to our cluster membership. The sole literature estimate gives a value of 2,300 pc^[84] for distance, which somewhat agrees with our determination of $d \approx 2,800(700)$ pc. We note that in the previous literature estimate an automatic survey was used. Distance determination did not rely on direct methods such as distance modulus calibration or parallax and inherently had error without minor optimization being implemented, and such error was not quoted.^[84] Our extinction estimate appears reasonable, having resulted in accurate distance calibrations. Plots produced in determining the reddening and distance to this cluster can be found in appendix C.

Parameter	Value	Error _{1σ}
A_V	1.98	0.04
d	2,800 pc	700 pc

Table 20: Reddening and distance estimates with error for [FSR 2007] 0433, to 1σ .

4.12.2 Centroid, Proper Motion & Membership

The determined cluster centroid coordinates, radius, and mean proper motion estimates are displayed in Table 21. These were determined via KDE, with plots displayed in Figure ?? . Centroid coordinates match literature^[84]: previous proper motion estimates do not exist. Our centroid estimate matching literature motivated further study of the cluster. Cluster membership is shown in Table 27 with visualization of the cluster field displayed in Appendix M. The limited nature of this cluster membership made deducing errors in centroid and mean proper motion impossible for our methods, with radius itself being *extremely* rough and ill-constrained.

Parameter	Value
Centre RA	+23 25 50 40
Centre Dec	+61 19 48 00
Radius	6'
Proper Motion RA / mas/yr	-4.01
Proper Motion Dec / mas/yr	-2.07

Table 21: Cluster centroid, radius & proper motion estimates for [FSR 2007] 0433. Errors are not quoted, as this cluster was not of primary interest and membership was highly limited, limiting error estimation.

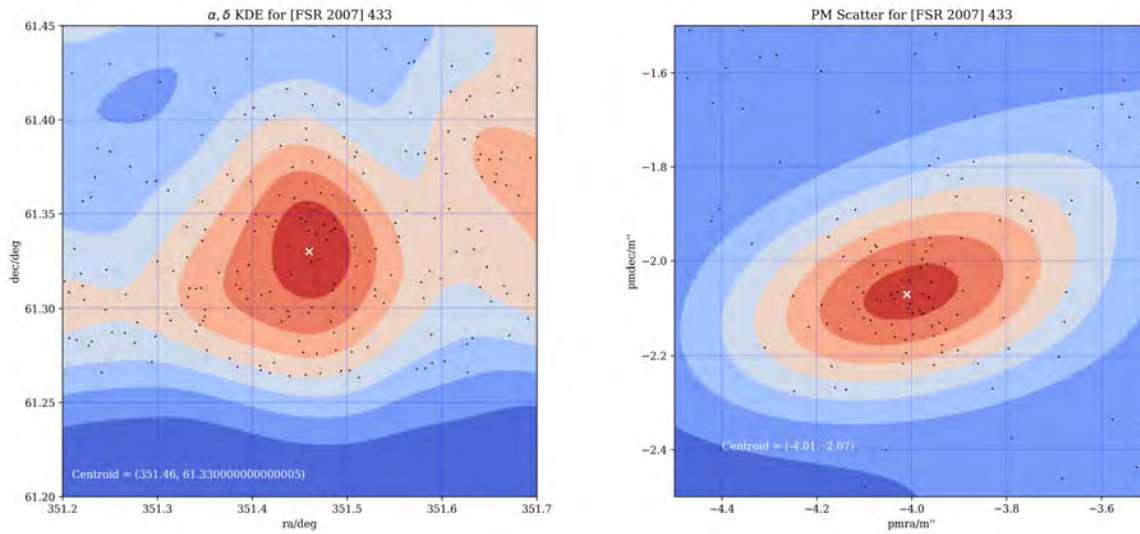


Figure 38: KDE estimation for [FSR 2007] 0433. Left: Position. Right: Proper motion.

4.12.3 Isochrone fitting

Parameter	Value	CI _{3σ}
$\log t$	7.09	[6.97, 8.52]

Table 22: Age estimation with 3σ confidence interval for [FSR 2007] 0433. $[\text{Fe}/\text{H}] = -0.1$.

Despite limited membership, an attempt was made to estimate cluster age: see Table 22 for results and Figure 39 for graphical representation. The obtained 3σ confidence interval is extremely wide: this is to be expected when fitting so few data-points via a χ^2 -based minimization.^[53] This interval indicates a plausible age range of 9.3 My to 331 My: this is extremely wide, however it does serve in providing a rough age estimate to where none previously existed. The $[\text{Fe}/\text{H}]$ estimate of -0.1 for the cluster is certainly arbitrary in light of limited membership: fitting metallicity by-eye proved impossible and this estimate was taken due to having given the lowest possible value of χ^2 during minimization for each set of isochrones.

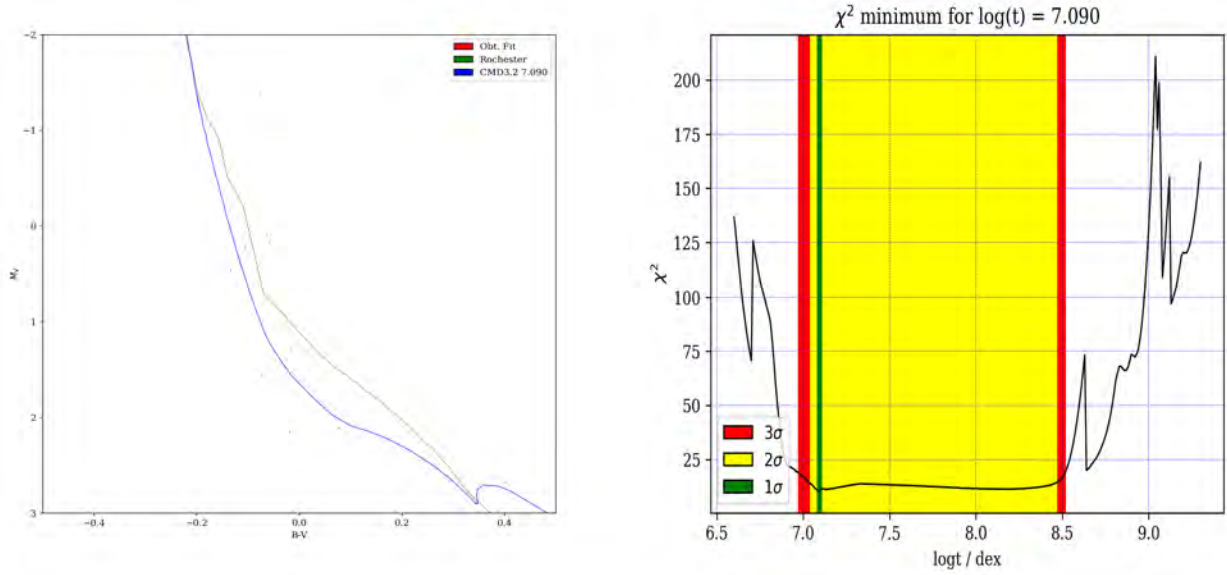


Figure 39: Left: Best-fitting isochrone for [FSR 2007] 0433, $[\text{Fe}/\text{H}]=-0.1$. Right: Confidence intervals deduced during age estimation for [FSR 2007] 0433.

5 Conclusion and Further Work

From exposures taken in October 2020 using the PIRATE telescope, the data from two star clusters was taken: M52 and NGC7789. This was then successfully reduced and calibrated using two standard stars, SA 20-39 and 111-773, and results were drawn such as cluster membership, reddening, distance, age, metallicity and integrated cluster mass. The standard star calibration was successful for one standard, 111-773 but unfortunately not for SA 20-39: we attribute this to poor seeing. Cluster membership was obtained initially by a manual apparent-magnitude cut, however this was noticeably less accurate than our final method of constraining by mean cluster proper motions and radial distance from the fitted centroid for the cluster. The determined memberships were found to be 209 for M52 and 529 for NGC 7789. The angular radii of the clusters were determined using surface density plots: these were found to be 0.21 (4) degrees for M52, and 0.20 (5) degrees for NGC 7789. Core radii of the clusters were also determined, being 0.06 (2) for M52, and 0.08 (3) for NGC 7789. The interstellar reddening A_V was determined to be 1.896(5) mags for M52, and 1.18(2) mags for NGC 7789. From this result, the distance to the clusters were determined to be 1810(80) pc for M52 and 2370(40) pc for NGC7789. Cluster ages were estimated using isochrone fitting and were found to be 69-143 Myr for M52, and 1.38-1.48 Gyr for NGC 7789, to 3σ . Abundance ratios for the clusters were determined to be 0.05 dex for M52 and -0.30 dex for NGC 7789. Salpeter IMF's were fitted to the mass distributions for both clusters, interpolated using a stellar grid model, and integrated cluster mass found: for M52 this was 1920 M_\odot , and for NGC 7789 5670 M_\odot . Total observed stellar mass was similarly determined, as 610 M_\odot for M52, and 1210 M_\odot for NGC 7789.

Whilst undertaking reduction, a second cluster was discovered serendipitously in the image field of M52, thought to be [FSR 2007] 0433. The results for this cluster were determined as follows: extinction coefficient A_V to be 1.98 (4), distance to the cluster as 2800 (700) pc, and log age of the cluster as 7.09 with a 3σ confidence interval of [6.97, 8.52]. Age determination proved difficult due to low determined cluster membership of 10 members. Cluster centroid was estimated by KDE, as [+23 25 50 40, +61 19 48 00] with a cluster radius of 6'. The mean proper motion of the cluster was determined by KDE as (-4.01, -2.07) mas/yr.

Future research for these clusters could include determining the presence of differential reddening across the clusters to investigate whether dust obscuration differs across the cluster. Deeper images taken for FSR [2007] 0433 may improve membership estimation and better constrain the age.

Result	M52	NGC 7789	[FSR 2007] 0433
Cluster Members	209	529	10
A_V / magnitudes	1.896(5)	1.18(2)	1.98(4)
Distance / pc	1810(80)	2370(40)	2800(700)
Centre (RA, Dec) / degrees	(351.20(2), 61.59(5))	(359.32(2), 56.75(5))	(351.46, 61.33)
Proper Motion (RA, Dec) / mas/yr	(-1.95(11), -1.14(11))	(-0.96(10), -1.95(10))	(-4.01, -2.07)
Radius / degrees	0.21(4)	0.20(5)	0.10
Core Radius / degrees	0.06(2)	0.08(3)	-
Age Range / Myr	[69, 143]	[1380, 1480]	[6.97, 8.52]
Metallicity [Fe/H] / dex	0.05	-0.30	-
Integrated Mass / M_\odot	1920	5670	-
Observed Luminous Mass / M_\odot	610	1210	-

Table 23: Summary of results.

6 Acknowledgements

A special thanks to our supervisor Ross McLure who has been advising us throughout this project and also to Philip Best and Colin Snodgrass for listening to and marking our group presentation. Thanks to Massissilia Hamadouche for helping us out with the observation. We thank the Open University for letting us operate the PIRATE telescope.

References

- [1] “M52”. In: *Encyclopedia of Astronomy and Astrophysics*. Ed. by P. Murdin. 2000, p. 6052. doi: [10.1888/0333750888/6052](https://doi.org/10.1888/0333750888/6052).
- [2] Mark R. Krumholz, Christopher F. McKee, and Joss Bland-Hawthorn. “Star Clusters Across Cosmic Time”. In: *Annual Review of Astronomy and Astrophysics* 57.1 (2019), pp. 227–303. doi: [10.1146/annurev-astro-091918-104430](https://doi.org/10.1146/annurev-astro-091918-104430). URL: <https://doi.org/10.1146/annurev-astro-091918-104430>.
- [3] P. Kroupa, S. Aarseth, and J. Hurley. “The formation of a bound star cluster: from the Orion nebula cluster to the Pleiades”. In: *Monthly Notices of the Royal Astronomical Society* 321.4 (Mar. 2001), pp. 699–712. ISSN: 1365-2966. doi: [10.1046/j.1365-8711.2001.04050.x](https://doi.org/10.1046/j.1365-8711.2001.04050.x). URL: <http://dx.doi.org/10.1046/j.1365-8711.2001.04050.x>.
- [4] J. G. Hills. “The effect of mass loss on the dynamical evolution of a stellar system - Analytic approximations”. In: 235 (Feb. 1980), pp. 986–991. doi: [10.1086/157703](https://doi.org/10.1086/157703).
- [5] K. A. Janes and R. L. Phelps. “The Galactic System of Old Star Clusters: The Development of the Galactic Disk”. In: 108 (Nov. 1994), p. 1773. doi: [10.1086/117192](https://doi.org/10.1086/117192).
- [6] Brad M. S. Hansen et al. “The White Dwarf Cooling Sequence of the Globular Cluster Messier 4”. In: *The Astrophysical Journal* 574.2 (Aug. 2002), pp. L155–L158. doi: [10.1086/342528](https://doi.org/10.1086/342528). URL: <https://doi.org/10.1086/342528>.
- [7] Brian Chaboyer. “Globular Cluster Age Dating”. In: *Astrophysical Ages and Times Scales*. Ed. by Ted von Hippel, Chris Simpson, and Nadine Manset. Vol. 245. Astronomical Society of the Pacific Conference Series. Jan. 2001, p. 162.
- [8] Bruce G. Elmegreen and Yuri N. Efremov. “A Universal Formation Mechanism for Open and Globular Clusters in Turbulent Gas”. In: *The Astrophysical Journal* 480.1 (May 1997), pp. 235–245. doi: [10.1086/303966](https://doi.org/10.1086/303966). URL: <https://doi.org/10.1086/303966>.
- [9] P. J. E. Peebles and R. H. Dicke. “Origin of the Globular Star Clusters”. In: 154 (Dec. 1968), p. 891. doi: [10.1086/149811](https://doi.org/10.1086/149811).
- [10] N. T. Kaltcheva. “Photographic UVBY Photometry of the Open Cluster M52”. In: 173.1 (Nov. 1990), pp. 69–76. doi: [10.1007/BF00642563](https://doi.org/10.1007/BF00642563).
- [11] Jason A. Cardelli, Geoffrey C. Clayton, and John S. Mathis. “The Relationship between Infrared, Optical, and Ultraviolet Extinction”. In: 345 (Oct. 1989), pp. 245–256. doi: [10.1086/167900](https://ui.adsabs.harvard.edu/abs/1989ApJ...345..245C). URL: <https://ui.adsabs.harvard.edu/abs/1989ApJ...345..245C>.
- [12] N. V. Kharchenko et al. “Astrophysical parameters of Galactic open clusters”. In: 438.3 (Aug. 2005), pp. 1163–1173. doi: [10.1051/0004-6361:20042523](https://doi.org/10.1051/0004-6361:20042523). arXiv: [astro-ph/0501674](https://arxiv.org/abs/astro-ph/0501674) [astro-ph].
- [13] A. K. Pandey et al. “NGC 7654: An interesting cluster to study star formation history”. In: 374 (Aug. 2001), pp. 504–522. doi: [10.1051/0004-6361:20010642](https://doi.org/10.1051/0004-6361:20010642).
- [14] T. Cantat-Gaudin et al. “A Gaia DR2 view of the open cluster population in the Milky Way”. In: 618, A93 (Oct. 2018), A93. doi: [10.1051/0004-6361/201833476](https://doi.org/10.1051/0004-6361/201833476). arXiv: [1805.08726](https://arxiv.org/abs/1805.08726) [astro-ph.GA].
- [15] SIMBAD Astronomical Database - CDS. <http://simbad.u-strasbg.fr/simbad/>. Accessed: 2021-02-27.
- [16] Xin-hua Gao. “Memberships, Distances, and Proper Motions of the Open Clusters NGC 2112, NGC 2477, NGC 7789, and Collinder 261 from Gaia-DR2”. In: 130.994 (Dec. 2018), p. 124101. doi: [10.1088/1538-3873/aae0d2](https://doi.org/10.1088/1538-3873/aae0d2).
- [17] Zhen-Yu Wu et al. “BATC 13 Band Photometry of the Open Cluster NGC 7789”. In: 133.5 (May 2007), pp. 2061–2071. doi: [10.1086/512189](https://doi.org/10.1086/512189). arXiv: [astro-ph/0701282](https://arxiv.org/abs/astro-ph/0701282) [astro-ph].
- [18] *Messier Object 52. The Messier Catalogue*. <https://www.messier.seds.org/m/m052.html>. Accessed: 2021-02-27.
- [19] Len Adam. *Imaging the Messier Objects Remotely from Your Laptop*. 2018.

- [20] *Messier 52*. Freestarcharts. <https://freestarcharts.com/messier-52>. Accessed: 2021-02-27.
- [21] *NGC 7789*. *Observing at Skyhound*. https://observing.skyhound.com/archives/oct/NGC_7789.html. Accessed: 2021-02-27.
- [22] Andrew C. Nine et al. “WIYN Open Cluster Study. LXXXII. Radial-velocity Measurements and Spectroscopic Binary Orbits in the Open Cluster NGC 7789”. In: 160.4, 169 (Oct. 2020), p. 169. doi: [10.3847/1538-3881/abad3b](https://doi.org/10.3847/1538-3881/abad3b). arXiv: [2003.09732](https://arxiv.org/abs/2003.09732) [astro-ph.SR].
- [23] *NGC 7789*. *The Messier Catalogue*. <http://messier.obspm.fr/xtra/ngc/n7789.html>. Accessed: 2021-02-27.
- [24] *The Importance of Star clusters*. <http://people.tamu.edu/~kevinkrisciunas/msfit.pdf>. Accessed: 2021-03-04.
- [25] *Star Clusters and the Milky Way*. https://www.e-education.psu.edu/astro801/content/18_p4.html. Accessed: 2021-03-04.
- [26] S. Holmes et al. “PIRATE: a remotely operable telescope facility for research and education”. In: *Publications of the Astronomical Society of the Pacific* 123.908 (2011), pp. 1177–1187. URL: <http://oro.open.ac.uk/30573/>.
- [27] D. C. Wells, E. W. Greisen, and R. H. Harten. “FITS - a Flexible Image Transport System”. In: 44 (June 1981), p. 363.
- [28] The HDF Group. *Hierarchical data format version 5*. 2010. URL: <http://www.hdfgroup.org/HDF5>.
- [29] Andrew Collette. *Python and HDF5*. O’Reilly, 2013.
- [30] Charles R. Harris et al. “Array programming with NumPy”. In: *Nature* 585 (2020), pp. 357–362. doi: [10.1038/s41586-020-2649-2](https://doi.org/10.1038/s41586-020-2649-2).
- [31] Guido Van Rossum and Fred L. Drake. *Python 3 Reference Manual*. Scotts Valley, CA: CreateSpace, 2009. ISBN: 1441412697.
- [32] S Littlefair. *PHY217 Observational Techniques for Astronomers*. URL: <http://slittlefair.staff.shef.ac.uk/teaching/phy217/lectures/principles/L04/index.html>.
- [33] Johnson, H. L. and Morgan, W. W. “Fundamental stellar photometry for standards of spectral type on the Revised System of the Yerkes Spectral Atlas.” In: 117 (May 1953), p. 313. doi: [10.1086/145697](https://doi.org/10.1086/145697).
- [34] Frederick R. Chromey. *To Measure the Sky: An Introduction to Observational Astronomy*. 2nd ed. Cambridge University Press, 2016. doi: [10.1017/CB09781316424117](https://doi.org/10.1017/CB09781316424117).
- [35] Arlo U. Landolt. “UBVRIPHOTOMETRIC STANDARD STARS AROUND THE SKY AT 50 deg DECLINATION”. In: *The Astronomical Journal* 146.5 (Oct. 2013), p. 131. doi: [10.1088/0004-6256/146/5/131](https://doi.org/10.1088/0004-6256/146/5/131). URL: <https://doi.org/10.1088/0004-6256/146/5/131>.
- [36] *Gaussian Function*. URL: <https://mathworld.wolfram.com/GaussianFunction.html>.
- [37] Ross McLure. *Observational Astronomy Notes*. 2019.
- [38] Barry A. Bodhaine et al. “On Rayleigh Optical Depth Calculations”. In: *Journal of Atmospheric and Oceanic Technology* 16.11 (1999), pp. 1854–1861. doi: [10.1175/1520-0426\(1999\)016<1854:ORODC>2.0.CO;2](https://doi.org/10.1175/1520-0426(1999)016<1854:ORODC>2.0.CO;2). URL: https://journals.ametsoc.org/view/journals/atot/16/11/1520-0426_1999_016_1854_orodc_2_0_co_2.xml.
- [39] Arlo U. Landolt. “UBVRI Photometric Standard Stars in the Magnitude Range 11.5 < V < 16.0 Around the Celestial Equator”. In: 104 (July 1992), p. 340. doi: [10.1086/116242](https://doi.org/10.1086/116242).
- [40] J. D. Hunter. “Matplotlib: A 2D graphics environment”. In: *Computing in Science & Engineering* 9.3 (2007), pp. 90–95. doi: [10.1109/MCSE.2007.55](https://doi.org/10.1109/MCSE.2007.55).
- [41] Dustin Lang et al. “Astrometry.net: Blind Astrometric Calibration of Arbitrary Astronomical Images”. In: 139.5 (May 2010), pp. 1782–1800. doi: [10.1088/0004-6256/139/5/1782](https://doi.org/10.1088/0004-6256/139/5/1782). arXiv: [0910.2233](https://arxiv.org/abs/0910.2233) [astro-ph.IM].

- [42] Astropy Collaboration et al. “Astropy: A community Python package for astronomy”. In: 558, A33 (Oct. 2013), A33. doi: [10.1051/0004-6361/201322068](https://doi.org/10.1051/0004-6361/201322068). arXiv: [1307.6212](https://arxiv.org/abs/1307.6212) [astro-ph.IM].
- [43] Astropy Collaboration et al. “The Astropy Project: Building an Open-science Project and Status of the v2.0 Core Package”. In: 156.3, 123 (Sept. 2018), p. 123. doi: [10.3847/1538-3881/aabc4f](https://doi.org/10.3847/1538-3881/aabc4f). arXiv: [1801.02634](https://arxiv.org/abs/1801.02634) [astro-ph.IM].
- [44] Pauli Virtanen et al. “SciPy 1.0: Fundamental Algorithms for Scientific Computing in Python”. In: *Nature Methods* 17 (2020), pp. 261–272. doi: [10.1038/s41592-019-0686-2](https://doi.org/10.1038/s41592-019-0686-2).
- [45] Larry McNish. *RASC Calgary Centre - Field Rotation with an Alt-Az Telescope Mount*. Jan. 2014. URL: https://calgary.rasc.ca/field_rotation.htm.
- [46] F. Bonnarel et al. “The ALADIN interactive sky atlas. A reference tool for identification of astronomical sources”. In: 143 (Apr. 2000), pp. 33–40. doi: [10.1051/aas:2000331](https://doi.org/10.1051/aas:2000331).
- [47] Henny J.G.L.M. Lamers and Emily M. Levesque. *Understanding Stellar Evolution*. 2514-3433. IOP Publishing, 2017. ISBN: 978-0-7503-1278-3. doi: [10.1088/978-0-7503-1278-3](https://doi.org/10.1088/978-0-7503-1278-3). URL: <http://dx.doi.org/10.1088/978-0-7503-1278-3>.
- [48] S.F. Green and M.H. Jones. *An Introduction to the Sun and Stars*. Cambridge University Press, 2015. ISBN: 9781107492639. URL: <https://books.google.co.uk/books?id=cJjLrQEACAAJ>.
- [49] F. van Leeuwen. “Validation of the new Hipparcos reduction”. In: 474.2 (Nov. 2007), pp. 653–664. doi: [10.1051/0004-6361:20078357](https://doi.org/10.1051/0004-6361:20078357). arXiv: [0708.1752](https://arxiv.org/abs/0708.1752) [astro-ph].
- [50] Zhen-Yu Wu et al. “The orbits of open clusters in the Galaxy”. In: *Monthly Notices of the Royal Astronomical Society* 399.4 (Nov. 2009), pp. 2146–2164. ISSN: 1365-2966. doi: [10.1111/j.1365-2966.2009.15416.x](https://doi.org/10.1111/j.1365-2966.2009.15416.x). URL: <http://dx.doi.org/10.1111/j.1365-2966.2009.15416.x>.
- [51] Y. Xin and L. Deng. “Blue Stragglers in Galactic Open Clusters and Integrated Spectral Energy Distributions”. In: *The Astrophysical Journal* 619.2 (Feb. 2005), pp. 824–838. ISSN: 1538-4357. doi: [10.1086/426681](https://doi.org/10.1086/426681). URL: <http://dx.doi.org/10.1086/426681>.
- [52] *Kernel Density Estimation*. <https://deeppai.org/machine-learning-glossary-and-terms/kernel-density-estimation>. Accessed: 2021-02-28.
- [53] K. F. Riley, M. P. Hobson, and S. J. Bence. “Statistics”. In: *Mathematical Methods for Physics and Engineering: A Comprehensive Guide*. 3rd ed. Cambridge University Press, 2006, pp. 1221–1304. doi: [10.1017/CB09780511810763.034](https://doi.org/10.1017/CB09780511810763.034).
- [54] C. M. Frayn and G. F. Gilmore. “The analysis of red giant branch photometry in galaxies”. In: *Monthly Notices of the Royal Astronomical Society* 337.2 (Dec. 2002), pp. 445–458. ISSN: 0035-8711. doi: [10.1046/j.1365-8711.2002.05918.x](https://doi.org/10.1046/j.1365-8711.2002.05918.x). eprint: <https://academic.oup.com/mnras/article-pdf/337/2/445/18643682/337-2-445.pdf>. URL: <https://doi.org/10.1046/j.1365-8711.2002.05918.x>.
- [55] C. M. Frayn and G. F. Gilmore. “The analysis of isochrone fitting methods for red giant branch photometry, and tip red giant branch distance determination”. In: *Monthly Notices of the Royal Astronomical Society* 339.3 (Mar. 2003), pp. 887–896. ISSN: 0035-8711. doi: [10.1046/j.1365-8711.2003.06250.x](https://doi.org/10.1046/j.1365-8711.2003.06250.x). eprint: <https://academic.oup.com/mnras/article-pdf/339/3/887/2936444/339-3-887.pdf>. URL: <https://doi.org/10.1046/j.1365-8711.2003.06250.x>.
- [56] Paola Marigo et al. “A NEW GENERATION OF PARSEC-COLIBRISTELLAR ISOCHRONES INCLUDING THE TP-AGB PHASE”. In: *The Astrophysical Journal* 835.1 (Jan. 2017), p. 77. ISSN: 1538-4357. doi: [10.3847/1538-4357/835/1/77](https://doi.org/10.3847/1538-4357/835/1/77). URL: <http://dx.doi.org/10.3847/1538-4357/835/1/77>.
- [57] Aaron Dotter. “MESA ISOCHRONES AND STELLAR TRACKS (MIST) 0: METHODS FOR THE CONSTRUCTION OF STELLAR ISOCHRONES”. In: *The Astrophysical Journal Supplement Series* 222.1 (Jan. 2016), p. 8. ISSN: 1538-4365. doi: [10.3847/0067-0049/222/1/8](https://doi.org/10.3847/0067-0049/222/1/8). URL: <http://dx.doi.org/10.3847/0067-0049/222/1/8>.

- [58] Eric W Weisstein. *Least Squares Fitting*. URL: <https://mathworld.wolfram.com/LeastSquaresFitting.html>.
- [59] Mark J. Pecaut and Eric E. Mamajek. “Intrinsic Colors, Temperatures, and Bolometric Corrections of Pre-main-sequence Stars”. In: 208.1, 9 (Sept. 2013), p. 9. doi: [10.1088/0067-0049/208/1/9](https://doi.org/10.1088/0067-0049/208/1/9). arXiv: [1307.2657](https://arxiv.org/abs/1307.2657) [astro-ph.SR].
- [60] Jianwen Luo, Kui Ying, and Jing Bai. “Savitzky–Golay smoothing and differentiation filter for even number data”. In: *Signal Processing* 85.7 (2005), pp. 1429–1434. issn: 0165-1684. doi: <https://doi.org/10.1016/j.sigpro.2005.02.002>. URL: <https://www.sciencedirect.com/science/article/pii/S0165168405000654>.
- [61] Gary Varner. URL: <https://www.phys.hawaii.edu/~varner/PHYS305-Spr12/DataFitting.html>.
- [62] Rob Reid. URL: <http://www.reid.ai/2012/09/chi-squared-distribution-table-with.html>.
- [63] Ferguson, Annette. “The Milky Way Galaxy.” In: *Astrophysics Notes, Sem 1* (2020), p. 4.
- [64] Edwin E. Salpeter. “The Luminosity Function and Stellar Evolution.” In: 121 (Jan. 1955), p. 161. doi: [10.1086/145971](https://doi.org/10.1086/145971).
- [65] Nate Bastian, Kevin R. Covey, and Michael R. Meyer. “A Universal Stellar Initial Mass Function? A Critical Look at Variations”. In: *Annual Review of Astronomy and Astrophysics* 48.1 (Aug. 2010), pp. 339–389. issn: 1545-4282. doi: [10.1146/annurev-astro-082708-101642](https://doi.org/10.1146/annurev-astro-082708-101642). URL: <http://dx.doi.org/10.1146/annurev-astro-082708-101642>.
- [66] National Optical Astronomy Observatories. *IRAF: Image Reduction and Analysis Facility*. Nov. 1999. ascl: [9911.002](https://www.ascl.net/ascl/9911.002).
- [67] Munhwan Gim et al. “The open cluster NGC 7789. II. CCD VI photometry”. In: *Publications of the Astronomical Society of the Pacific* 110 (Sept. 1998). doi: [10.1086/316266](https://doi.org/10.1086/316266).
- [68] C. Jordi et al. “Gaia broad band photometry”. In: 523, A48 (Nov. 2010), A48. doi: [10.1051/0004-6361/201015441](https://doi.org/10.1051/0004-6361/201015441). arXiv: [1008.0815](https://arxiv.org/abs/1008.0815) [astro-ph.IM].
- [69] *Messier 52*. <https://www.messier-objects.com/messier-52/>. Accessed: 2021-02-28.
- [70] M. Pim Fitzgerald. “The Intrinsic Colours of Stars and Two-Colour Reddening Lines”. In: 4 (Feb. 1970), p. 234. URL: <https://ui.adsabs.harvard.edu/abs/1970A&A....4..234F>.
- [71] Timothy D. Morton. *isochrones: Stellar model grid package*. Mar. 2015. ascl: [1503.010](https://www.ascl.net/ascl/1503.010).
- [72] M. Viskum et al. “A search for delta Scuti stars in northern open clusters. I. CCD photometry of NGC 7245, NGC 7062, NGC 7226 and NGC 7654”. In: 328 (Dec. 1997), pp. 158–166.
- [73] G. Carraro and C. Chiosi. “The Galactic system of old open clusters: age calibration and age-metallicity relation”. In: 287 (July 1994), pp. 761–768.
- [74] Munhwan Gim et al. “The Open Cluster NGC 7789. I. Radial Velocities for Giant Stars”. In: 110.752 (Oct. 1998), pp. 1172–1182. doi: [10.1086/316241](https://doi.org/10.1086/316241). arXiv: [astro-ph/9807057](https://arxiv.org/abs/astro-ph/9807057) [astro-ph].
- [75] P. Mazzei and L. Pigatto. “Intermediate-age open clusters as discriminators between overshooting and classical evolutionary models.” In: 193 (Mar. 1988), pp. 148–158.
- [76] Seiichi Yoshida. Jan. 2021. URL: http://www.aerith.net/astro/color_conversion.html.
- [77] Michael S. Bessell. “The Hipparcos and Tycho Photometric System Passbands”. In: *Publications of the Astronomical Society of the Pacific* 112.773 (July 2000), pp. 961–965. doi: [10.1086/316598](https://doi.org/10.1086/316598). URL: <https://doi.org/10.1086/316598>.
- [78] G. L. H. Harris and R. G. Deupree. “Effects of heavy-element abundances on the color-magnitude diagrams of young clusters in the Galaxy and the Magellanic Clouds.” In: 209 (Oct. 1976), pp. 402–410. doi: [10.1086/154733](https://doi.org/10.1086/154733).

- [79] C. Bonatto and E. Bica. “Methods for improving open cluster fundamental parameters applied to M52 and NGC3960”. In: *Astronomy Astrophysics* 455.3 (Aug. 2006), pp. 931–942. issn: 1432-0746. doi: [10.1051/0004-6361:20065315](https://doi.org/10.1051/0004-6361:20065315). url: <http://dx.doi.org/10.1051/0004-6361:20065315>.
- [80] L. Girardi, J. -C. Mermilliod, and G. Carraro. “On the peculiar red clump morphology in the open clusters NGC 752 and NGC 7789”. In: 354 (Feb. 2000), pp. 892–898. arXiv: [astro-ph/0001068](https://arxiv.org/abs/astro-ph/0001068) [[astro-ph](https://arxiv.org/abs/astro-ph/0001068)].
- [81] E. Paez et al. “The Oldest Galactic Open Clusters - New CCD Photometry and Colour / Magnitude Diagrams”. In: 169.1-2 (July 1990), pp. 41–44. doi: [10.1007/BF00640683](https://doi.org/10.1007/BF00640683).
- [82] Zhen-Yu Wu et al. “Mass of open cluster NGC 7789”. In: *Chinese Physics Letters* 26 (Feb. 2009), p. 029701. doi: [10.1088/0256-307X/26/2/029701](https://doi.org/10.1088/0256-307X/26/2/029701).
- [83] Mark H. Jones, Robert J. A. Lambourne, and Stephen Serjeant. *An Introduction to Galaxies and Cosmology (2nd ed)*. Cambridge: Cambridge University Press/Open University, Jan. 2015. url: <http://oro.open.ac.uk/44361/>.
- [84] Anne S. M. Buckner and Dirk Froebrich. “Properties of star clusters – I. Automatic distance and extinction estimates”. In: *Monthly Notices of the Royal Astronomical Society* 436.2 (Sept. 2013), pp. 1465–1478. issn: 0035-8711. doi: [10.1093/mnras/stt1665](https://doi.org/10.1093/mnras/stt1665). eprint: <https://academic.oup.com/mnras/article-pdf/436/2/1465/13764051/stt1665.pdf>. url: <https://doi.org/10.1093/mnras/stt1665>.

A Observing Log

Date: 11 October 2020 Telescope: PIRATE, Tenerife, Spain

SCIENCE FRAME Total: 143 Files

- We used binning: 1x1 for all observations in Science Frame
- Standard star SA2039 at elevations of about 36, 57 and 72 degrees (U, B, V)
- Standard star 111773 at elevations of about 61 and 38 degrees (U, B, V)
- M52 in U,B,V. In B and V bands, this was 10x30 sec at each of three slightly offset pointings (for bad pixel removal), making 15 mins in total. In U band it was 3x300 sec at each of the three pointings, for 45 mins in total. - NGC7789 in U,B,V, with similar strategy to above, but 15 mins in V,B (3x5x60sec) and 30 mins in U (3x2x300sec).

Notes for observation:

- It looked to be about a 5 percent sky coverage of wispy clouds at twilight (obviously not too sure after that). We didn't see any evidence that the dataset was affected, but if a cloud hit a standard star observation it will be obvious in the atmospheric extinction plots, and that data can be discarded (we have 5). For the target, the repeated observations mean that, again, any with a cloud effect should be noticeable by a drop in counts, and compensated for / discarded.
- **[Important]**: The brightest star in the M52 cluster, although unsaturated in the initial images, saturated in V in the later images as seeing improved - so just be careful to measure that one from only the first images.

Notes for calibration files:

- Dark frame: by default only 60 sec darks are taken, and we have a range of different exposures. In principle we could try to scale to other exposure times using a (dark - bias) frame to determine the dark current, assuming that this is linear with time. However, in practice the dark current is very low, and we are fine just using bias frames. Need to check this - use the dark frames. If there are missing calibration files, then have a look in the "*CalibrationFilesMidOct*" directory, one directory level up: that should contain a full set. The calibration is supposedly stable for several days, so even though some of these may be taken a day before or after the observation run, that's fine (they take a full set of calibration frames over a 2-day period).
- One important thing to note about the flats is that these will have been taken in twilight, when the sky is changing in brightness. Therefore they need to be multiplicatively scaled before combining them.

A.1 Observation Data

Standard Star	Right Ascension	Declination	Band	Time of Obs	Elevation	Exposure Time(sec)
111773	19h37m16s	00°10'59"	U	1928	62°	30
111773			U	1944	62°	30
111773			U	2202	43°	30
111773			U	2218	38°	30
111773			U	2223	38°	30
111773			U	2224	38°	30
111773			B	1929	62°	10
111773			B	1944	62°	10
111773			B	2203	43°	10
111773			B	2225	38°	10
111773			V	1929	62°	10
111773			V	1945	62°	10
111773			V	2203	43°	10
111773			V	2225	38°	10
SA2039	00h45m34.1s	45°36'48.2"	U	1946	33°	30
SA2039			U	2001	35°	60
SA2039			U	2205	57°	60
SA2039			U	2219	59°	60
SA2039			U	0002	72°	60
SA2039			B	1947	33°	10
SA2039			B	2003	35°	20
SA2039			B	2206	57°	20
SA2039			B	2221	59°	20
SA2039			B	0003	72°	20
SA2039			V	1948	33°	10
SA2039			V	2003	35°	20
SA2039			V	2207	57°	20
SA2039			V	2221	59°	20
SA2039			V	0004	72°	20

Table 24: Astronomical data for images of 2 standard stars

Observation	Number of Frames		
	U	B	V
Standard Stars			
Standard Star - SA2039	5	5	5
Standard Star - 111773	6	4	4
M52			
Offset 1	3	10	11
Offset 2	3	10	10
Offset 3	3	10	10
NGC7789			
Offset 1	2	5	5
Offset 2	2	5	5
Offset 3	2	5	5
Calibration Frames			
Flatfields	7	6	4
Bias Frames	24		
Dark Frames	11		

Table 25: Summary of observations taken.

Star Cluster	Right Ascension	Declination	Band	Time of Obs	Elevation	Exposure Time(sec)
M52	23h24m02s	61°35'00"	U	2002	45°	60*2
M52	23h24m02s	61°35'00"	B	2004	45°	30*2
M52	23h24m02s	61°35'00"	V	2005	45°	30*2
M52	23h24m02s	61°35'00"	U	2031	48°	300*3
M52	23h24m02s	61°35'00"	B	2023	47°	30*10
M52	23h24m02s	61°35'00"	V	2017	47°	30*10
M52	23h25m32s	61°36'22"	U	2107	51°	300*3
M52	23h25m32s	61°36'22"	B	2047	49°	30*10
M52	23h25m32s	61°36'22"	V	2053	49°	30*10
M52	23h25m16s	61°34'22"	U	2145	54°	300*3
M52	23h25m16s	61°34'22"	B	2100	50°	30*10
M52	23h25m16s	61°34'22"	V	2138	53°	30*10
NGC7789	23h57m00s	56°44'00"	U	2208	57°	60
NGC7789	23h57m00s	56°44'00"	B	2209	57°	30
NGC7789	23h57m00s	56°44'00"	V	2210	57°	30
NGC7789	23h57m00s	56°44'00"	U	2227	58°	300*2
NGC7789	23h57m00s	56°44'00"	B	2237	60°	60*5
NGC7789	23h57m00s	56°44'00"	V	2243	60°	60*5
NGC7789	23h57m08s	56°45'00"	U	2249	60°	300*2
NGC7789	23h57m08s	56°45'00"	B	2255	61°	60*5
NGC7789	23h57m08s	56°45'00"	V	2306	62°	60*5
NGC7789	23h56m52s	56°43'00"	U	2313	62°	300*2
NGC7789	23h56m52s	56°43'00"	B	2323	63°	60*5
NGC7789	23h56m52s	56°43'00"	V	2353	62°	60*5

Table 26: Astronomical data for images of 2 star clusters. Here, the exposures were repeated to capture the fainter images, hence the Repeat multiples in Exposure Time.

B Reddening and Distance Plot: Cluster Membership Proper Motion Matched with the Older Catalogue

B.1 Reddening plot for M52 and NGC7789

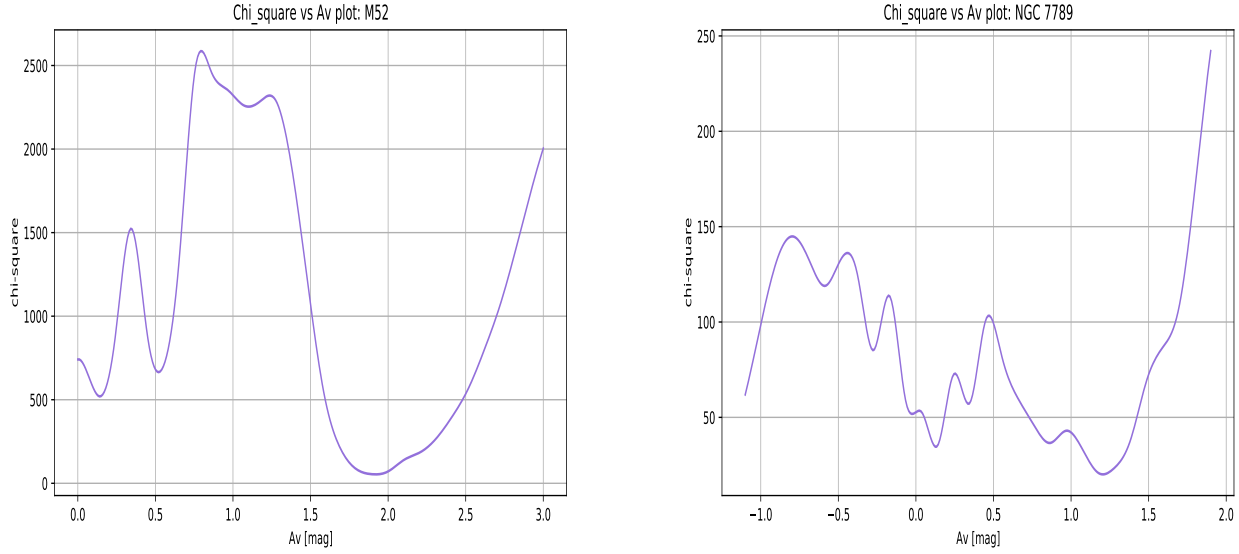


Figure 40: Chi-squared graph of M52 (left) and NGC7789 (right). The minimum chi-squared shows the optimal A_v value required to deredden our data.

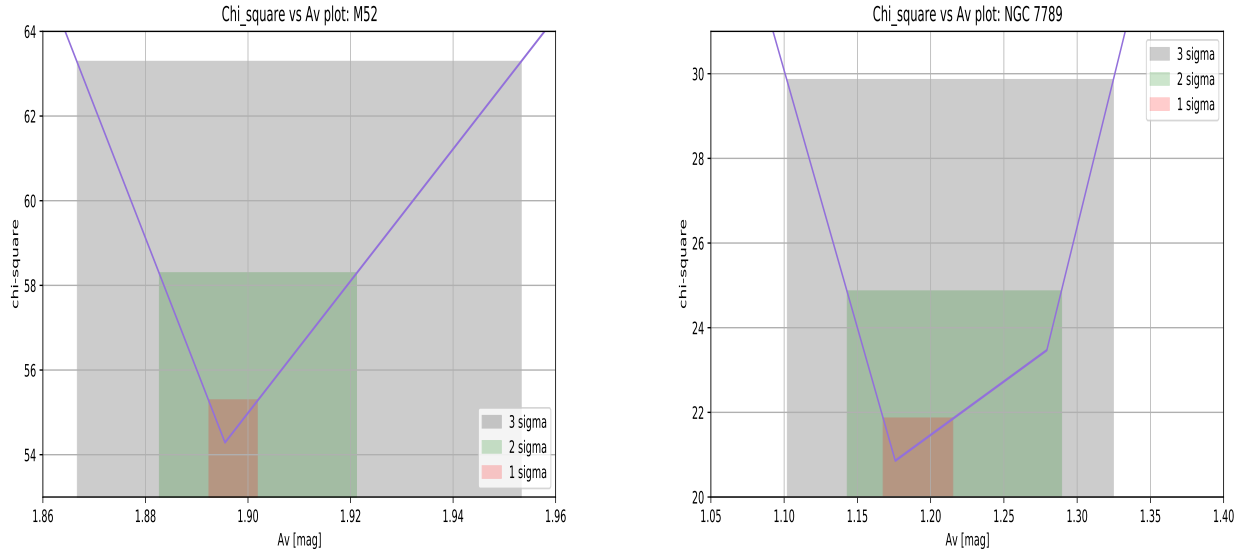


Figure 41: Zoom in version of chi-squared plot in Figure 40. A_v values error determination for M52 (left) and NGC7789 (right). Red region is the 1σ confidence interval, green region is the 2σ confidence interval and grey region is the 3σ confidence interval for the A_v values.

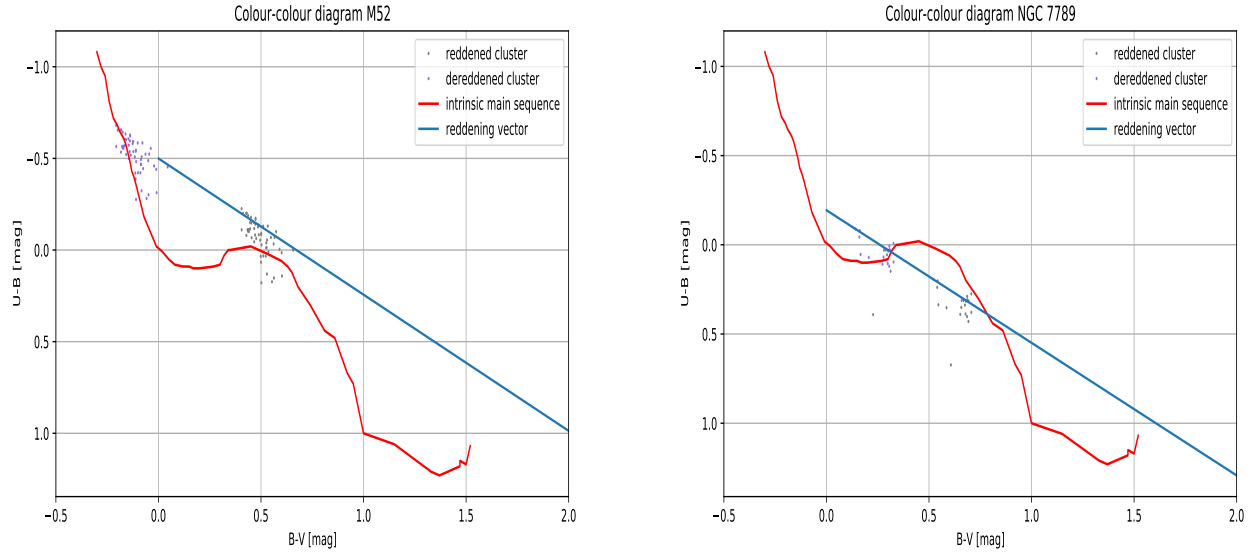


Figure 42: UBV diagram of M52 (left) and NGC7789 (right). Red line is the intrinsic main sequence taken from Fitzgerald et al^[70]. The blue line is the reddening vector that have a slope of 0.74324.

B.2 Distance determination plot for M52 and NGC7789

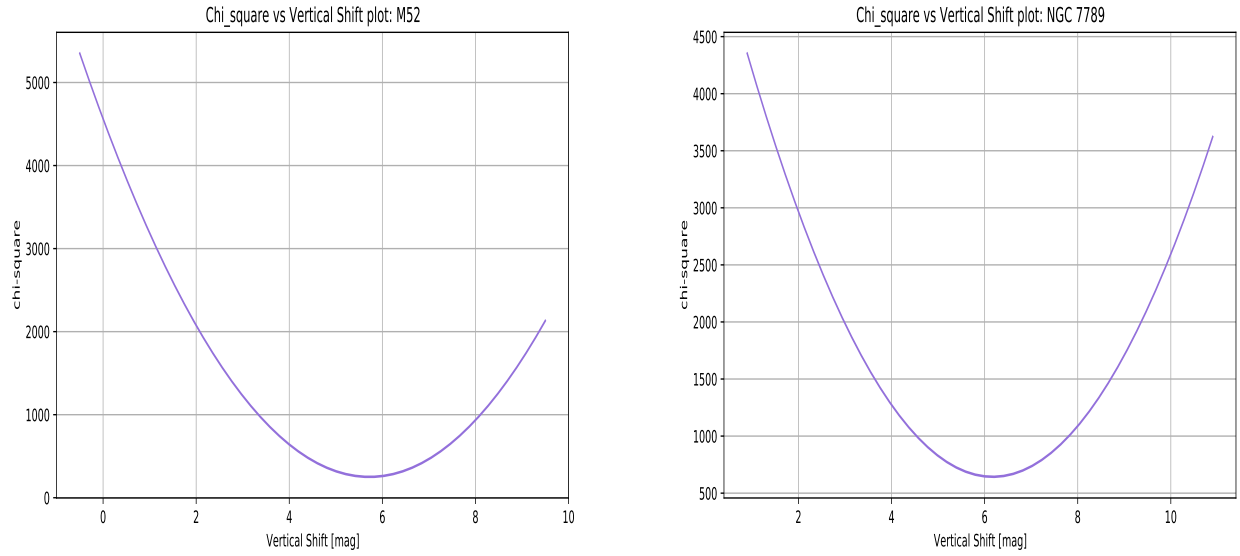


Figure 43: Chi-squared graph of M52 (left) and NGC7789 (right). The minimum chi-squared value shows the optimal vertical shift required for two main sequence in BV diagram to sit on top of each other.

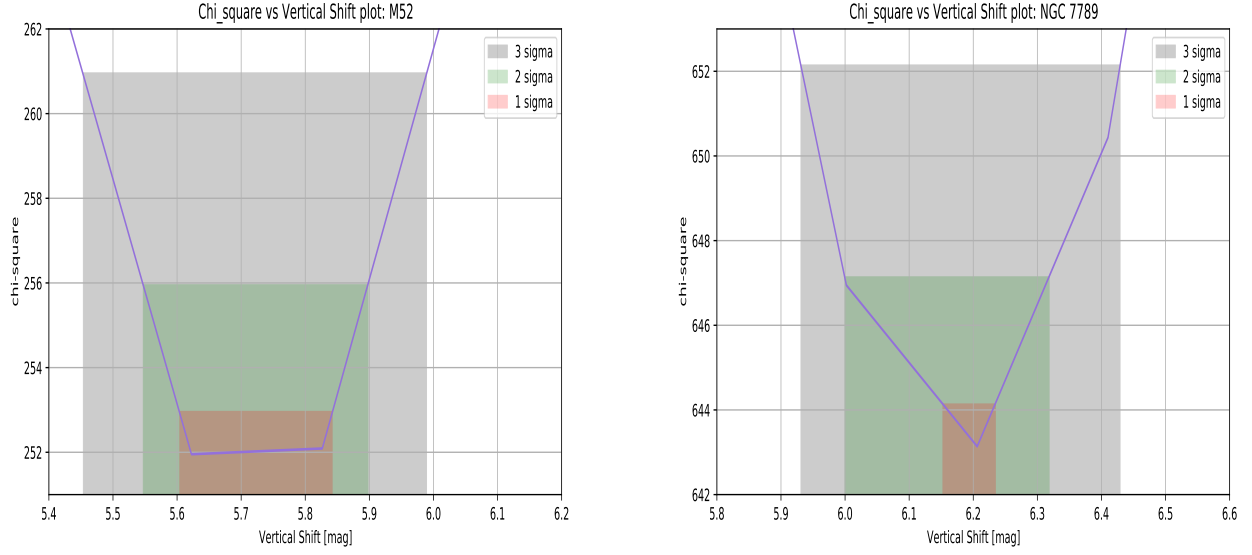


Figure 44: Zoom in version of chi-squared plot in Figure 43. Vertical shift error determination for M52 (left) and NGC7789 (right). Red region is the 1σ confidence interval, green region is the 2σ confidence interval and grey region is the 3σ confidence interval for the vertical shift values.

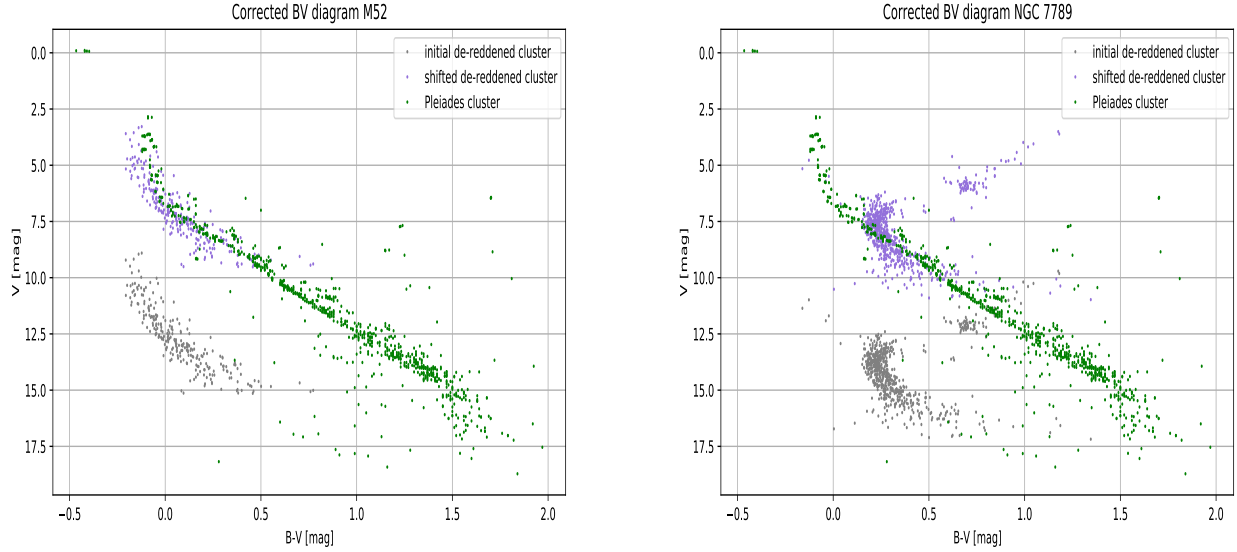


Figure 45: BV diagram for M52 (right) and NGC7789 (left). Green data points are the main sequence of Pleiades cluster (M45), the original dereddened cluster (grey) and the shifted dereddened cluster (purple). M45 cluster has a very low reddening with well-known distance from the GAIA parallax measurement to be 135.8 pc.

C Reddening and Distance: [FSR 2007] 0433 (Cluster near M52)

C.1 Reddening Plot

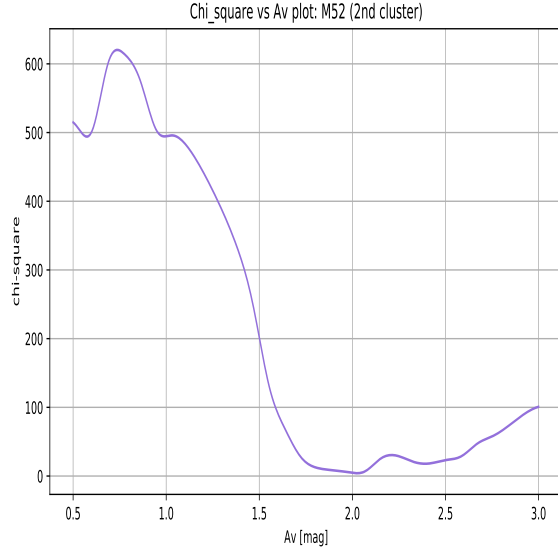


Figure 46: Chi-squared graph of the 2nd cluster of M52. The minimum chi-squared shows the optimal A_v value required to deredden our data.

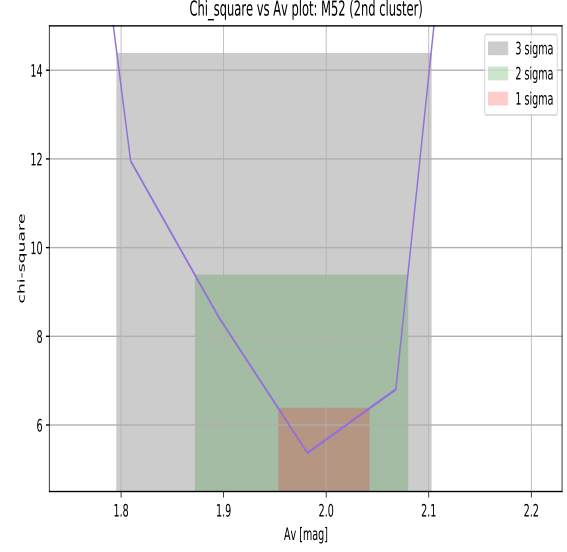


Figure 47: Zoom in version of chi-squared plot in Figure 46. A_v values error determination for 2nd cluster of M52. Red region is the 1σ confidence interval, green region is the 2σ confidence interval and grey region is the 3σ confidence interval for the A_v values.

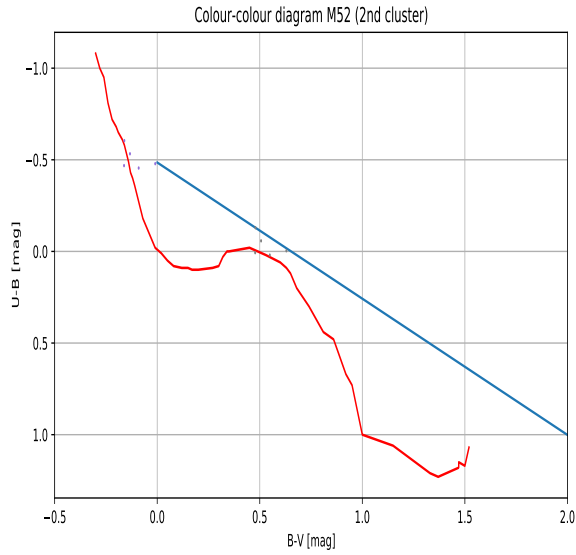


Figure 48: UB-V diagram of the 2nd cluster in M52. Red line is the intrinsic main sequence taken from Fitzgerald et al^[70]. The blue line is the reddening vector that have a slope of 0.74324. Grey points are the reddened data and purple points are the dereddened data.

C.2 Distance Plot

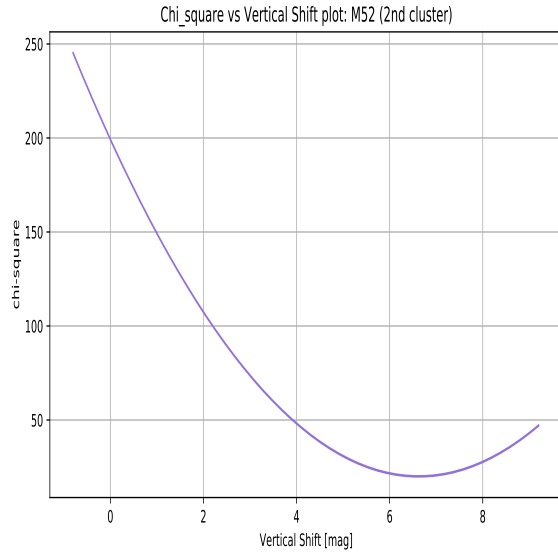


Figure 49: Chi-squared graph of 2nd cluster in M52. The minimum chi-squared value shows the optimal vertical shift required for two main sequence in BV diagram to sit on top of each other.

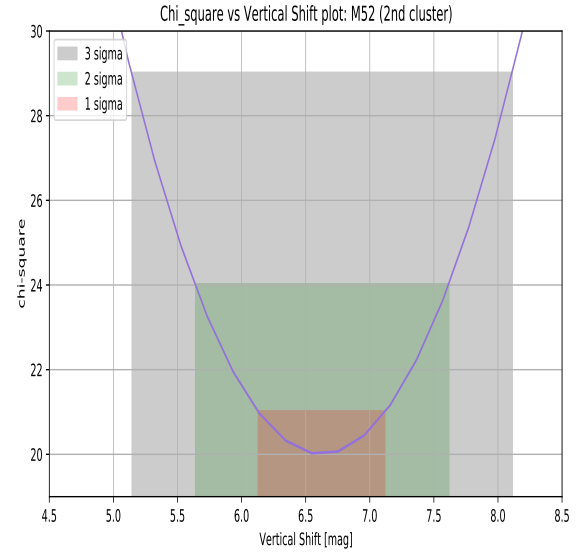


Figure 50: Zoom in version of chi-squared plot in Figure 49. Vertical shift error determination for 2nd cluster in M52. Red region is the 1σ confidence interval, green region is the 2σ confidence interval and grey region is the 3σ confidence interval for the vertical shift values.

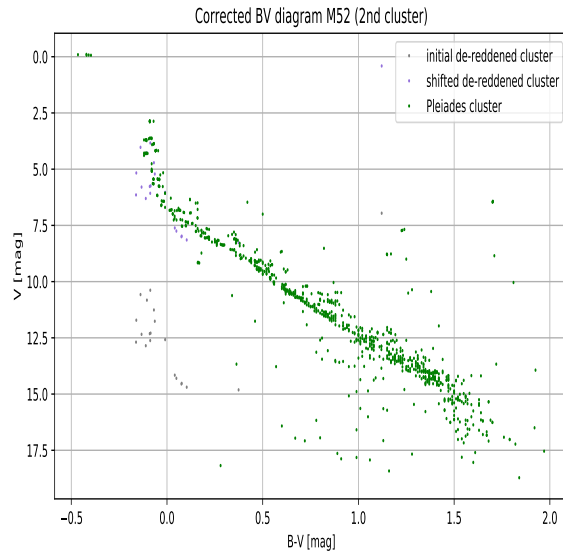


Figure 51: BV diagram for 2nd cluster in M52. Green data points are the main sequence of Pleiades cluster (M45), the original dereddened cluster (grey) and the shifted dereddened cluster (purple). M45 cluster has a very low reddening with well-known distance from the GAIA parallax measurement to be 135.8 pc.

D Error Propagation

D.1 Simple Aperture Photometry

Here we obtain ΔI_λ via error propagation of eq (3). For a region taken from the image array, we assume the error in N counts is given by \sqrt{N} .

B_λ is the background density. During simple aperture photometry with background estimation by an annulus mean this is given by

$$B_\lambda = \frac{I_{\lambda,an}}{A_{an}}$$

where $I_{\lambda,an}, A_{an}$ are the instrumental count and area of the annulus. We assume the area has no error and thus calculate

$$\Delta B_\lambda = \frac{\sqrt{I_{\lambda,an}}}{A_{an}}$$

Then propagating eq (3) we find

$$\begin{aligned} I_\lambda &= I_{\lambda,ap} - A_{ap} B_\lambda \\ \partial_{I_{\lambda,ap}} I_\lambda &= 1 \quad , \quad \partial_{B_\lambda} I_\lambda = -A_{ap} \\ \therefore \Delta I_\lambda &= \sqrt{(\Delta I_{\lambda,ap})^2 + (A_{ap} \Delta B_\lambda)^2} \end{aligned} \tag{31}$$

D.2 Optical Depth τ_λ

Here we obtain $\Delta \tau_\lambda$ via error propagation of Equation (6). We assume that $\Delta \theta = 0$. Let i, j be two observations at unique elevations.

$$\begin{aligned} \tau_{\lambda,(i,j)} &= \frac{\ln I_{\lambda,i} - \ln I_{\lambda,j}}{\sec \theta_j - \sec \theta_i} \\ |\partial_{I_{\lambda,i}}| &= \frac{1}{I_{\lambda,i}} \left| \frac{1}{\sec \theta_j - \sec \theta_i} \right| \\ \therefore \Delta \tau_\lambda &= \left| \frac{1}{\sec \theta_j - \sec \theta_i} \right| \sqrt{\left(\frac{\Delta I_{\lambda,i}}{I_{\lambda,i}} \right)^2 + \left(\frac{\Delta I_{\lambda,j}}{I_{\lambda,j}} \right)^2} \end{aligned} \tag{32}$$

D.3 $I_\lambda(0)$, the above-atmosphere flux

Here we obtain $\Delta I_\lambda(0)$ via error propagation of Equation (5). We assume that $\Delta \theta = 0$. θ is the zenith for the given measurement.

$$\begin{aligned}
I_\lambda(\theta) &= I_\lambda(0) \exp(-\tau_\lambda \sec \theta) \\
\therefore I_\lambda(0) &= I_\lambda(\theta) \exp(\tau_\lambda \sec \theta) \\
\partial_{I_\lambda} I_\lambda(0) &= \frac{I_\lambda(0)}{I_\lambda(\theta)} \quad , \quad \partial_{\tau_\lambda} I_\lambda(0) = I_\lambda(0) \sec \theta \\
\therefore \Delta I_\lambda(0) &= I_\lambda(0) \sqrt{\left(\frac{\Delta I_\lambda(\theta)}{I_\lambda(\theta)} \right)^2 + (\Delta \tau_\lambda \sec \theta)^2}
\end{aligned} \tag{33}$$

D.4 Error in m_λ

Here we propagate eq (??). We make use of the relation

$$\frac{\log_{10} a}{\log_{10} b} = \log_a b$$

and set $(a, b) = (e, F_\lambda)$ to find that

$$\begin{aligned}
\frac{\log_{10} F_\lambda}{\log_{10} e} &= \log_e F_\lambda \\
\therefore \log_{10} F_\lambda &= (\log_{10} e) \log_e F_\lambda
\end{aligned} \tag{34}$$

We propagate Equation (2) and make use of Equation (34) to deduce Δm_λ :

$$\begin{aligned}
m_\lambda &= -\frac{5}{2} \log_{10}(F_\lambda) + z_\lambda \\
\partial_{F_\lambda} m_\lambda &= -\frac{5}{2} (\log_{10} e) \frac{1}{F_\lambda} \quad , \quad \partial_{z_\lambda} m_\lambda = 1 \\
\therefore \Delta m_\lambda &= \sqrt{\left(\frac{5}{2} (\log_{10} e) \frac{\Delta F_\lambda}{F_\lambda} \right)^2 + (\Delta z_\lambda)^2}
\end{aligned} \tag{35}$$

D.5 Error in M_V

Here we propagate Equation (4). We tailor this specifically to our usage case, in which we assume that d is in parsecs (pc) and calculated using *GAIA DR2* parallax. Let ϕ be the parallax angle in arcseconds. $d, \Delta d$ are given by

$$d = \frac{1}{\phi} \tag{36}$$

$$\begin{aligned}
\partial_\phi d &= \frac{d}{\phi} \\
\therefore \Delta d &= d \left(\frac{\Delta \phi}{\phi} \right)
\end{aligned} \tag{37}$$

where Equation (36) is a common approximation for distance in Astronomy.^[37] We then propagate Equation (4) and once again make use of Equation (34):

$$M_\lambda = m_\lambda - 5 \log_{10} \left(\frac{d}{10 \text{ pc}} \right) \quad (38)$$

$$\begin{aligned} \partial_{m_\lambda} M_\lambda &= 1 \quad , \quad \partial_d M_\lambda = -5 (\log_{10} e) \frac{\frac{1}{10 \text{ pc}}}{\frac{d}{10 \text{ pc}}} = -5 (\log_{10} e) \frac{1}{d} \\ \therefore \Delta M_\lambda &= \sqrt{(\Delta m_\lambda)^2 + \left(5 (\log_{10} e) \frac{\Delta d}{d} \right)^2} \end{aligned} \quad (39)$$

D.6 Error in dereddened (B-V) & M_V

V-band absolute magnitudes and $B - V$ colours are dereddened as standard^[37] for the preliminary catalogue, with the dereddened M_V and colour given by

$$M_{V,DERED} = M_V - A_V \quad (40)$$

$$(B - V)_{DERED} = (B - V) - \frac{A_V}{R} \quad (41)$$

where A_V is our extinction coefficient and R is the ratio of total-to-selective extinction.^[11] We first propagate colour B-V to find

$$\Delta(B - V) = \sqrt{(\Delta m_V)^2 + (\Delta m_B)^2} \quad (42)$$

and subsequently propagate Equations (40) and (41) to find:

$$\Delta M_{V,DERED} = \sqrt{(\Delta M_V)^2 + (\Delta A_V)^2} \quad (43)$$

$$\Delta(B - V)_{DERED} = \sqrt{(\Delta(B - V))^2 + \left(\frac{\Delta A_V}{R} \right)^2} \quad (44)$$

E Final Deep Image Stacks



Figure 52: Deep images for M52. From left to right: U, B and V bands.



Figure 53: Deep images for NGC7789. From left to right: U, B and V bands.

F Images: source extraction for clusters

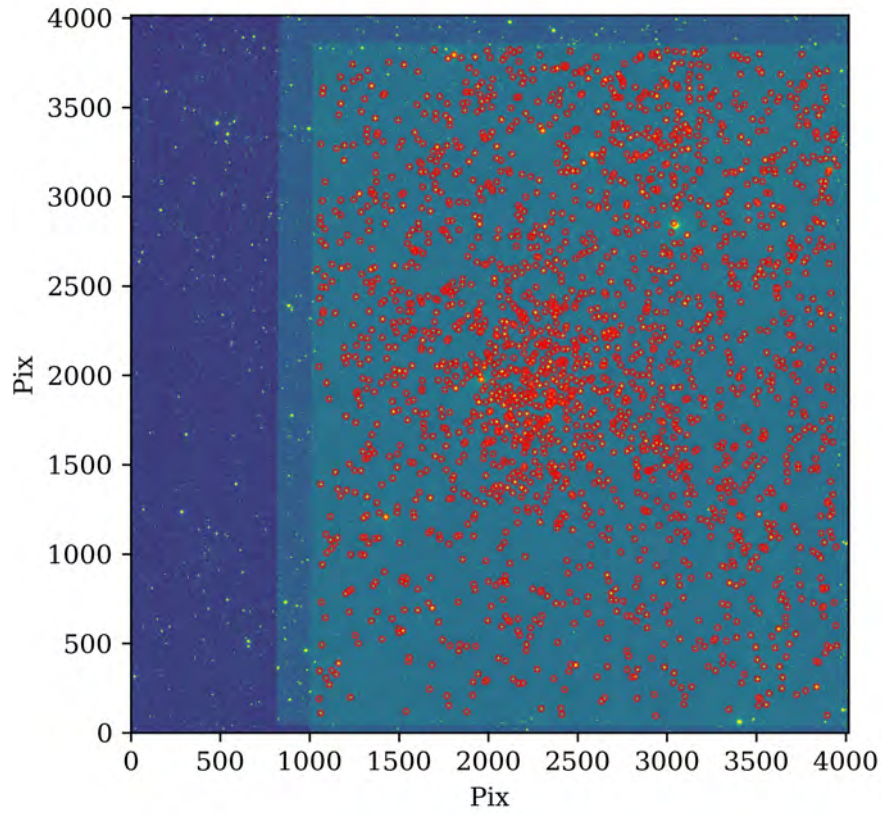


Figure 54: Deep image of M52 in the V-band, with source selection illustrated. The apertures here are the ones used in the photometry routine that used fixed apertures.

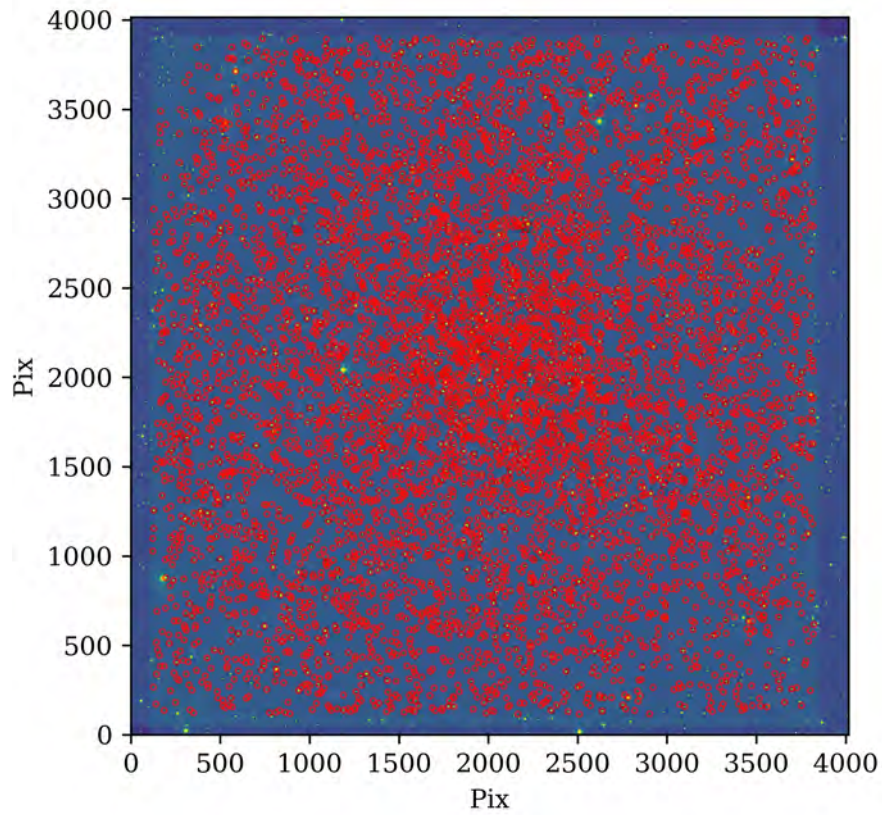


Figure 55: Deep image of NGC7789 in the V-band, with source selection illustrated. The apertures here are the ones used in the photometry routine that used fixed apertures.

G Preliminary CMD's for clusters

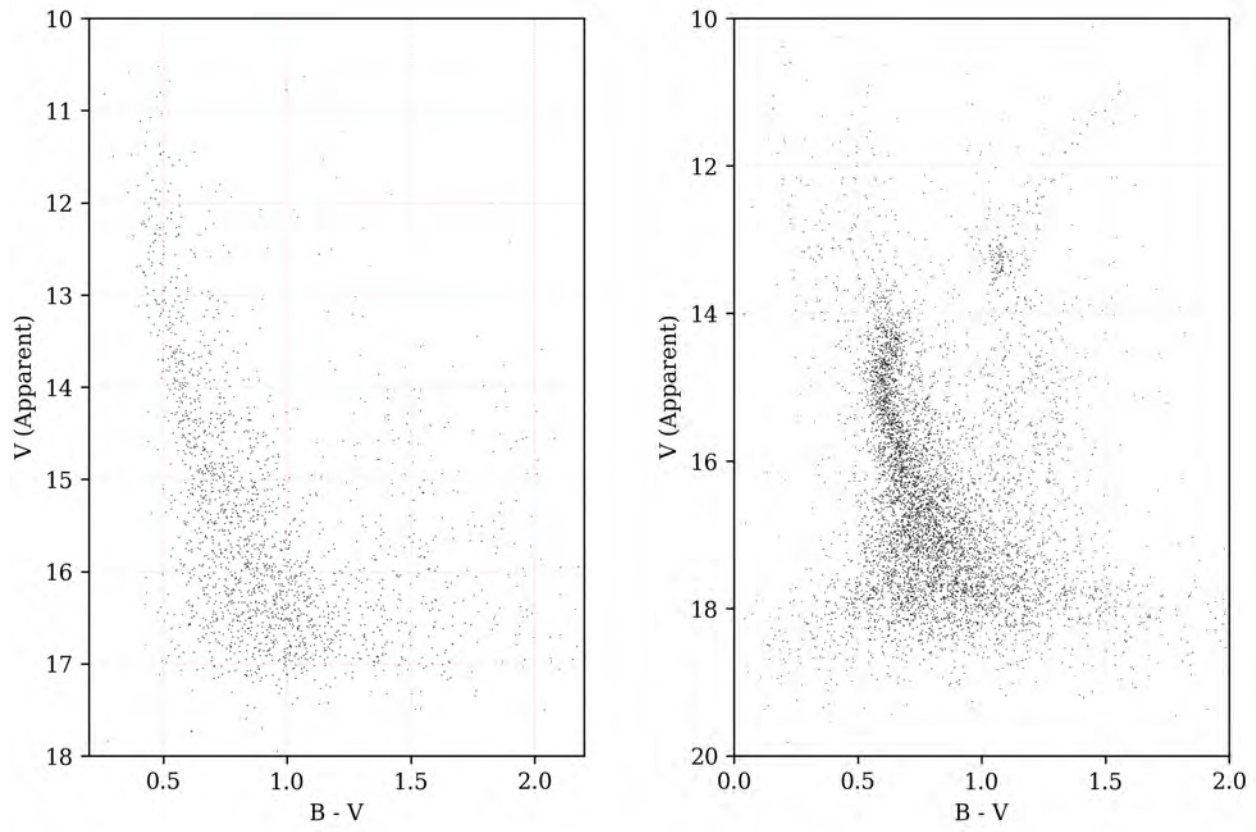


Figure 56: Preliminary CMD's for M52 (left) and NGC7789 (right). Pleiades main sequence provided for reference.

H Preliminary colour-colour diagrams for clusters

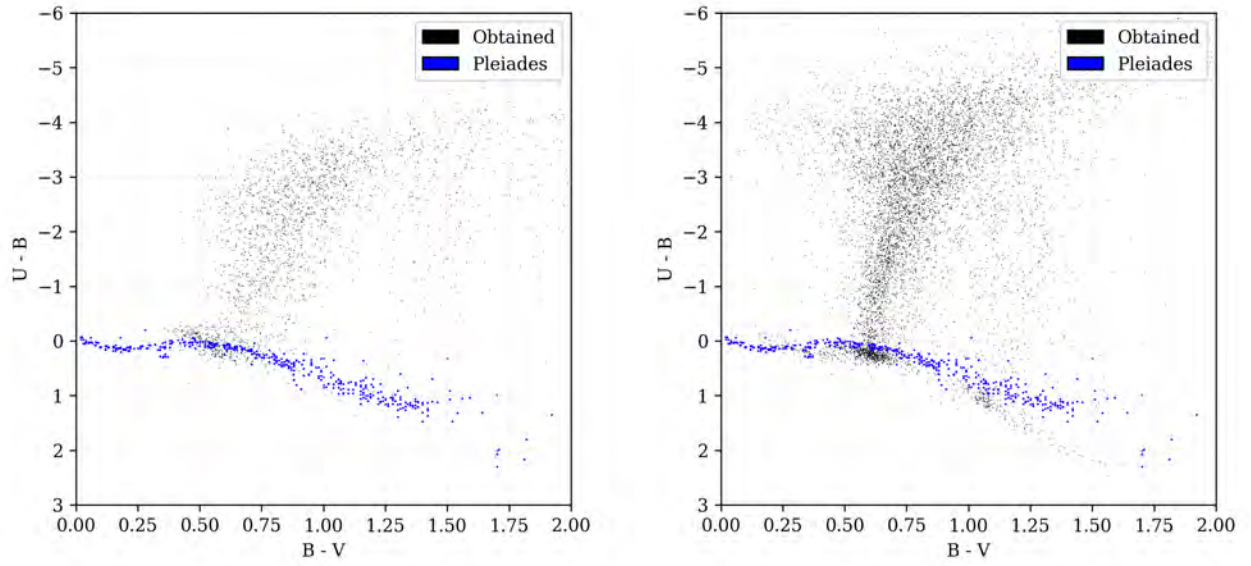


Figure 57: Preliminary colour-colour diagram for M52 (left) and NGC7789 (right). Pleiades main sequence provided for reference.

I GAIA CMD's in 20' vicinity of clusters

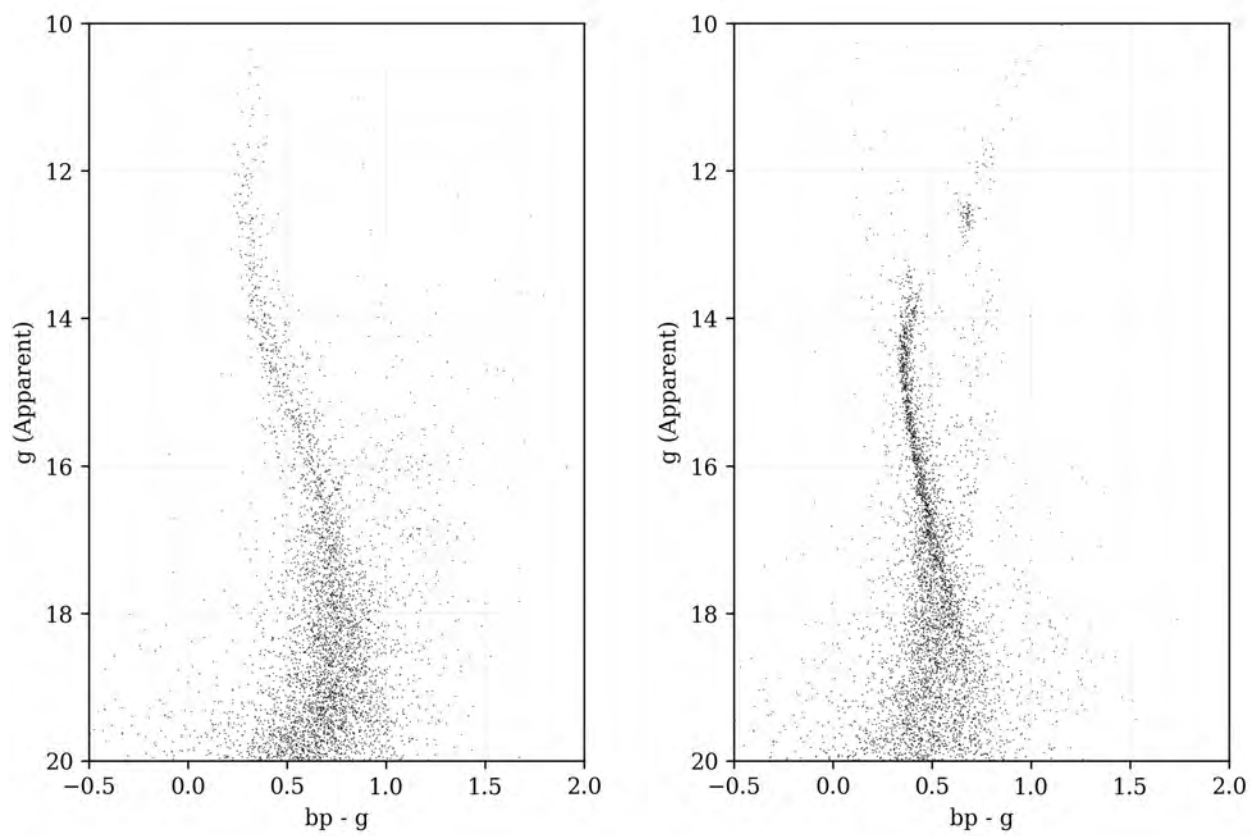


Figure 58: GAIA CMD for M52 (left) and NGC7789 (right), in GAIA DR2 passbands.

J Final CMD's for clusters

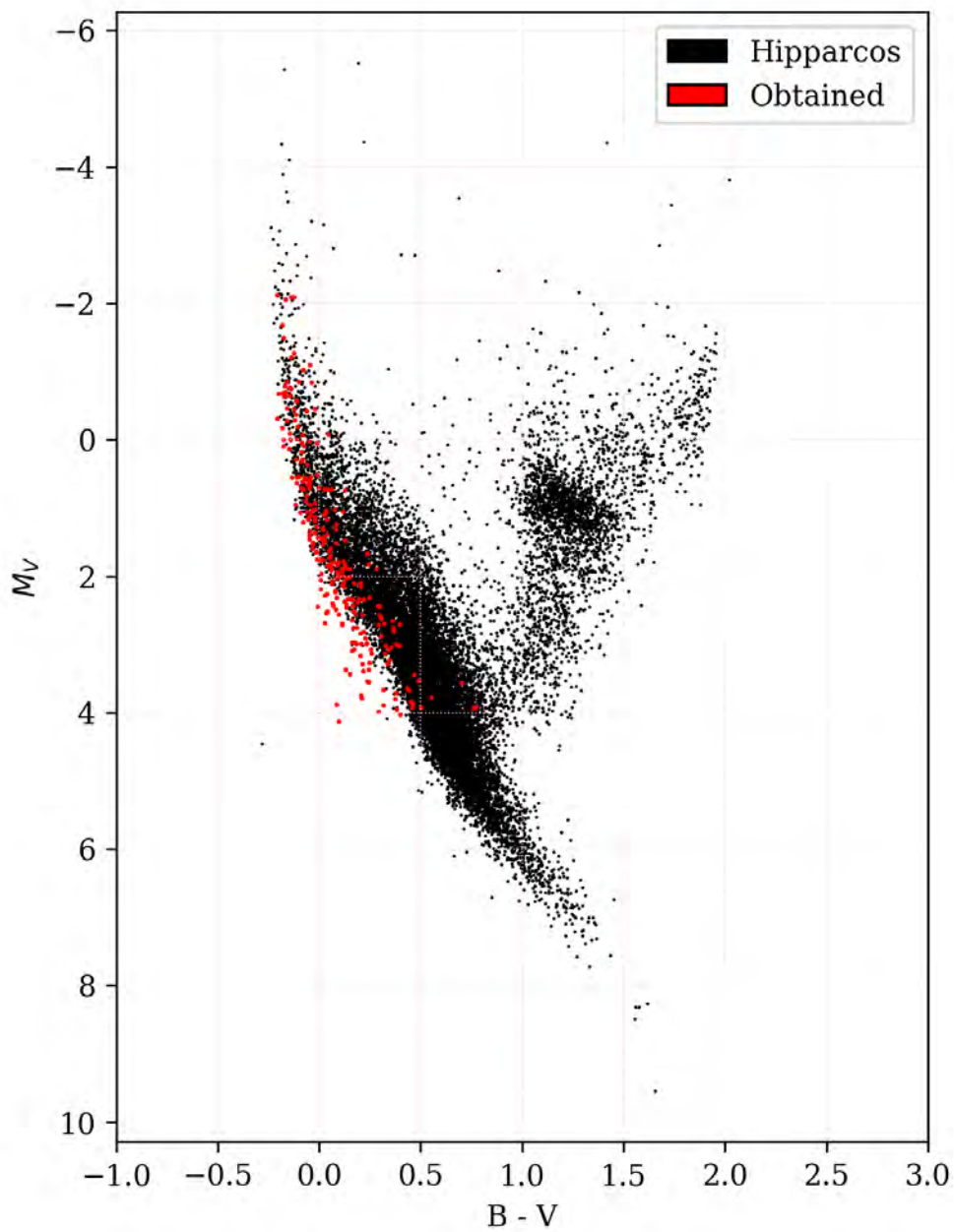


Figure 59: Derreddened CMD for M52 overplot with (uncorrected, error-limited as in original literature^[12]) Hipparcos CMD.

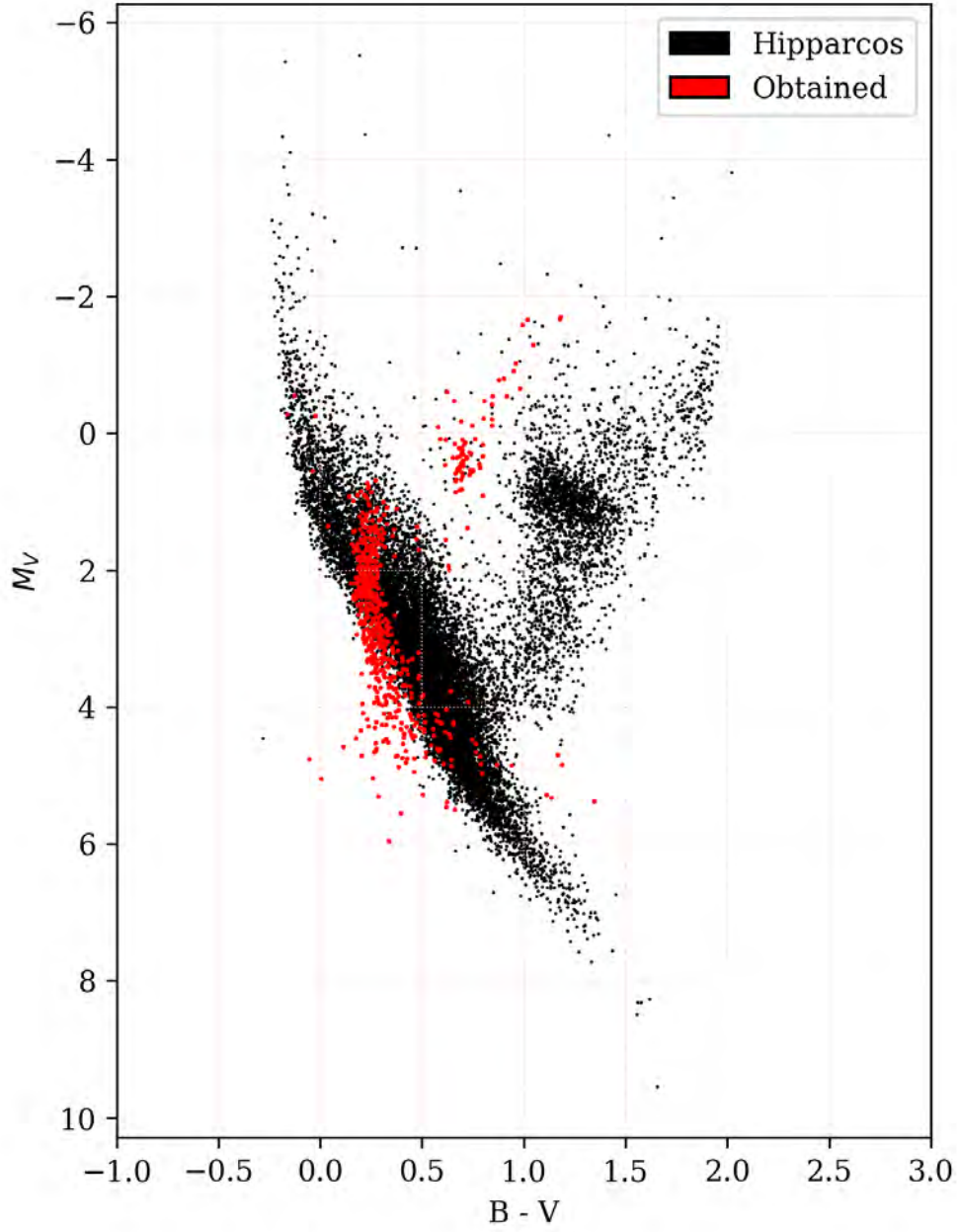


Figure 60: Derddenned CMD for NGC7789 overplot with (uncorrected, error-limited as in original literature^[12]) Hipparcos CMD.

K PARSEC/COLIBRI Isochrone fits for clusters

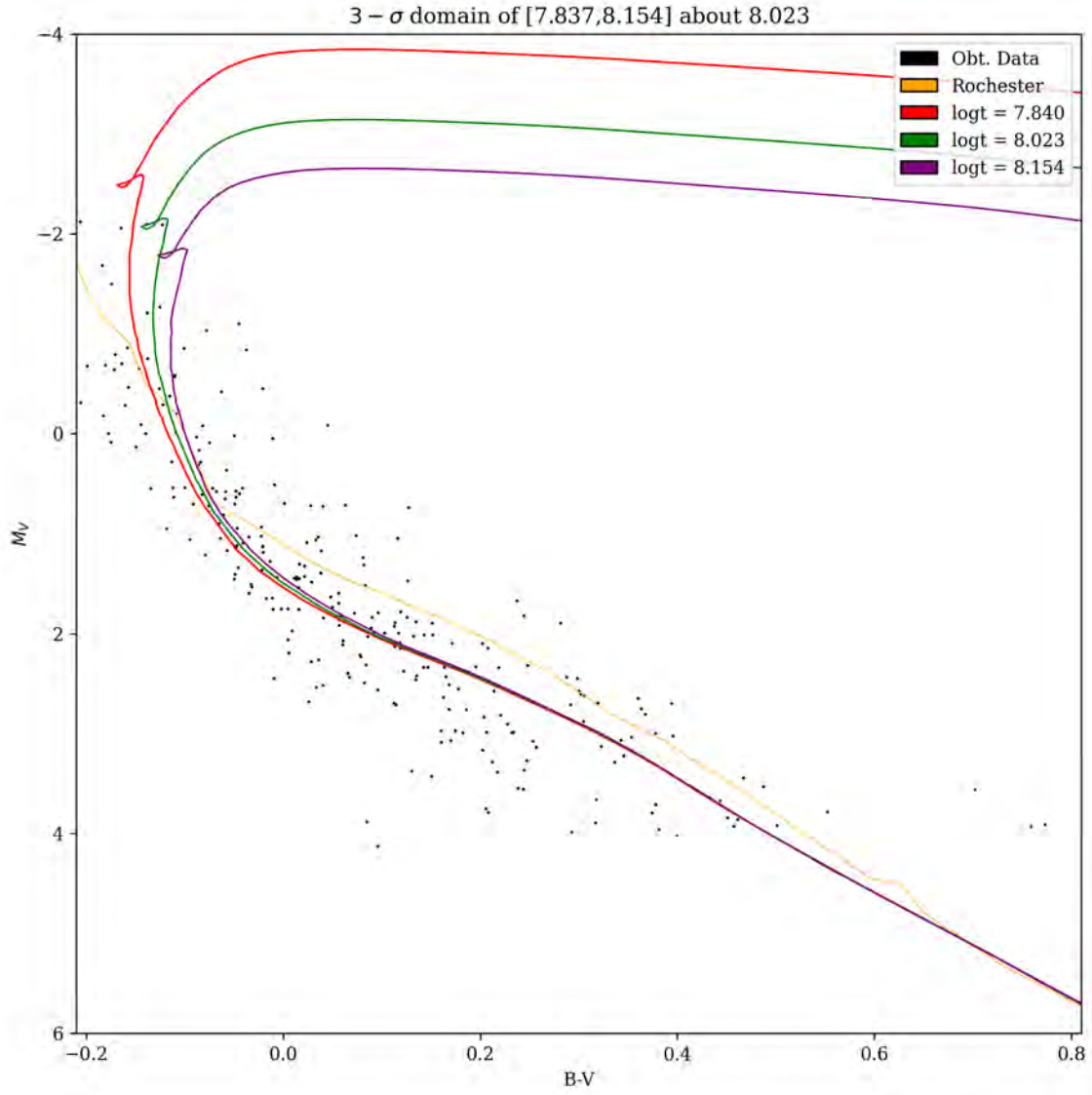


Figure 61: Fitted isochrones for M52. The Rochester MS locus is shown. Ages $\log t$ quoted in dex. $\chi^2(k=1)$ confidence intervals of 3, 2, 1 σ are shown.

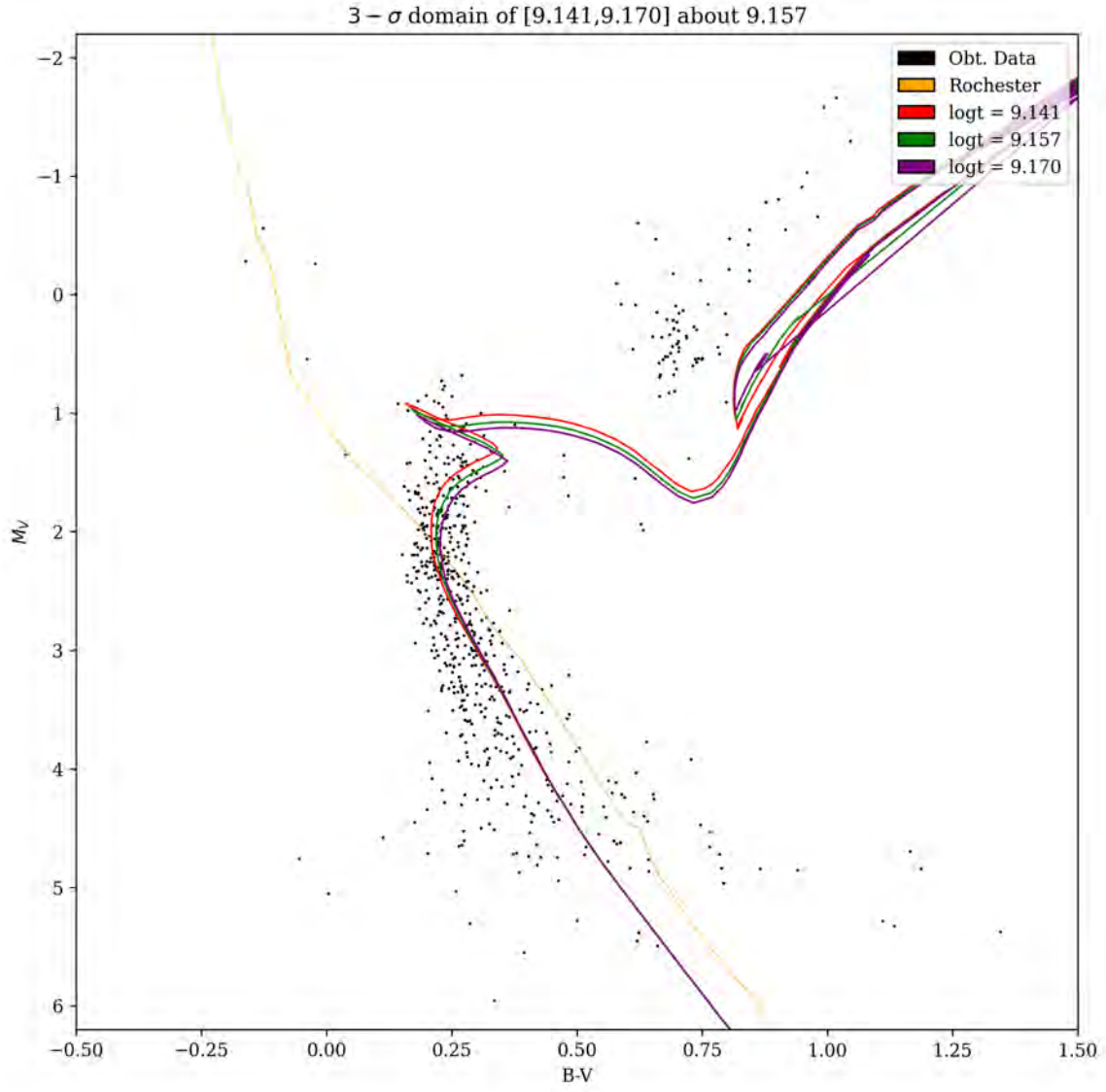


Figure 62: Fitted isochrones for NGC7789. The Rochester MS locus is shown. Ages $\log t$ quoted in dex. $\chi^2(k=1)$ confidence intervals of 3, 2, 1 σ are shown.

L Preliminary MIST isochrone fits

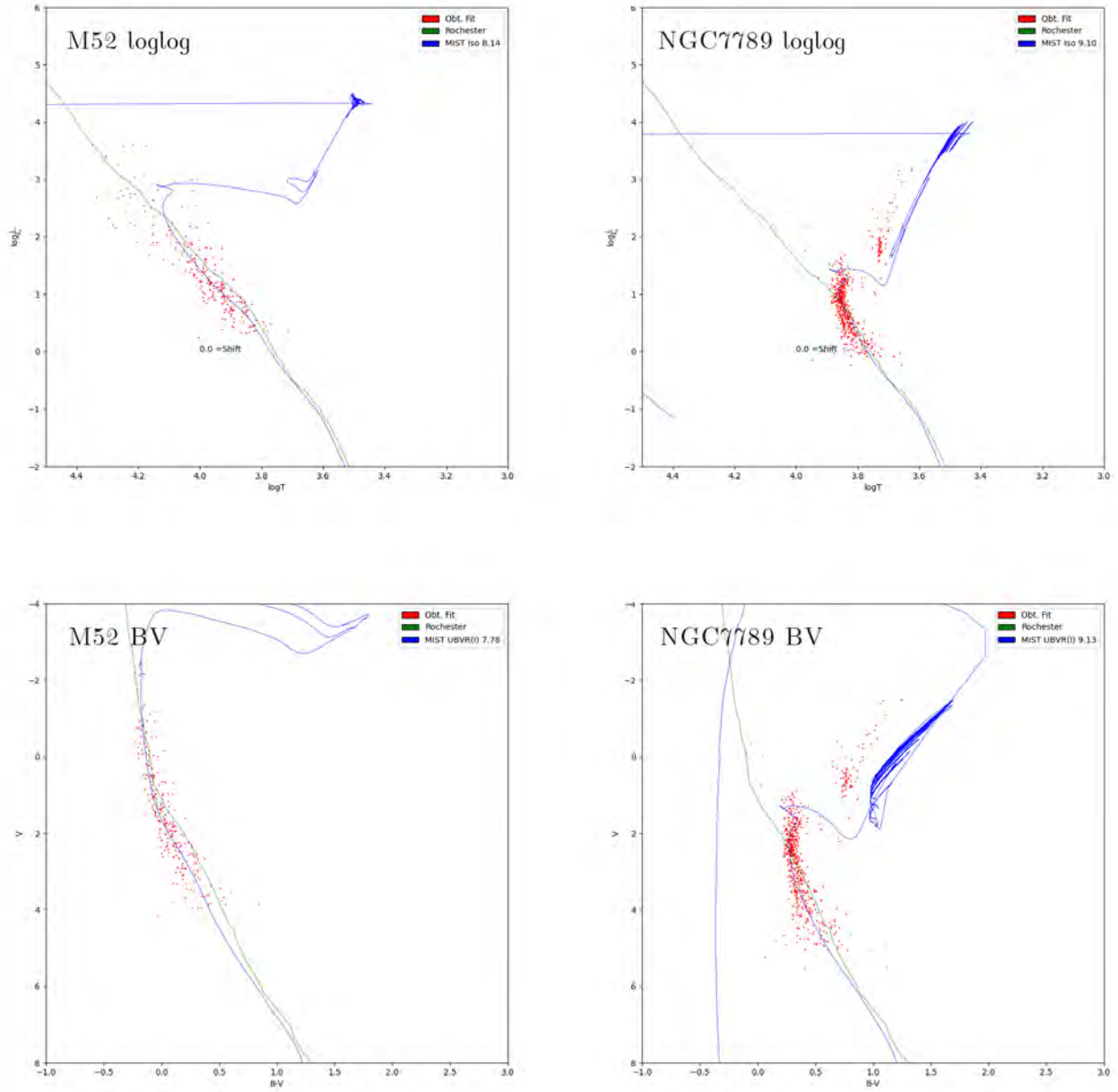


Figure 63: Fitted isochrones in $B - V, M_V$ & $\log T \log L$ parameter space, CMD & log-log space respectively, taken via weighted least-squares minimization. The Rochester MS locus is shown. Upper left: M52 in log-log space, Bottom left: M52 in CMD space, Upper right: NGC7789 in log-log space, Lower right: NGC7789 in CMD space.

M [FSR 2007] 0433: Objects

ID	α	δ	pm/ α /mas/yr	pm/ δ /mas/yr	d /pc	Δd /pc
1	351.429	61.360	−4.020	−2.220	2847	299
2	351.487	61.347	−4.090	−1.980	2781	362
3	351.366	61.350	−4.110	−2.100	2858	226
4	351.430	61.386	−4.000	−2.090	2775	149
5	351.456	61.346	−4.040	−2.130	2768	147
6	351.347	61.392	−4.150	−2.140	2889	150
7	351.551	61.345	−4.070	−2.080	2905	181
8	351.508	61.332	−3.930	−2.140	2867	215
9	351.387	61.310	−3.910	−2.010	2857	260
10	351.425	61.346	−4.090	−2.130	2855	271

Table 27: Obtained membership of [FSR 2007] 0433 with various observables taken from *GAIA DR2*. ID is arbitrary and assigned during reduction.

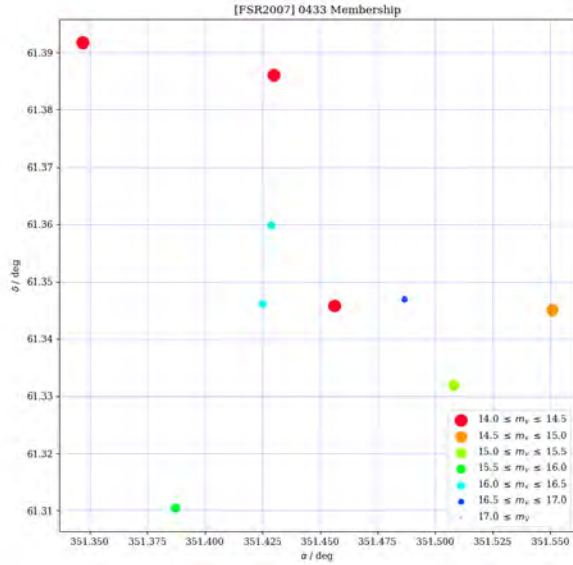


Figure 64: Determined cluster members in our field for [FSR 2007] 0433 clipped about the cluster centre, with atmospherically-corrected apparent magnitudes illustrated.